UNIVERSIDAD COMPLUTENSE DE MADRID

FACULTAD DE CIENCIAS FÍSICAS

Departamento de Astrofísica y Ciencias de la Atmósfera

TESIS DOCTORAL

High energy nonthermal emission from shocks produced in the interestellar medium

Emisión no térmica a altas energías procedente de choques producidos en el medio interestelar

MEMORIA PARA OPTAR AL GRADO DE DOCTOR

PRESENTADA POR

Víctor Pereira Blanco

Directores

Javier López Santiago
Elisa de Castro Rubio

Madrid, 2017

High-energy nonthermal emission from shocks produced in the interstellar medium

Emisión no térmica a altas energías procedente de choques producidos en el medio interestelar

Víctor Pereira Blanco

Departamento de Astrofísica y Ciencias de la Atmósfera

Facultad de Ciencias Físicas

Universidad Complutense de Madrid

A thesis submitted for the degree of
Doctor en Física
April, 25th 2017

Supervised by:
Javier López Santiago and **Elisa de Castro Rubio**

To all those I consider part of my life,
present or past.

Agradecimientos

Esta tesis no hubiera visto la luz sin la ayuda y consejo de mis directores, el Dr. Javier López Santiago y la Profesora Elisa de Castro Rubio. Gracias por haberme dado esta oportunidad y por haberme acompañado durante todo este tiempo. También quiero tener un agradecimiento especial para quienes me acogieron durante mi estancia en el Observatorio Astronómico de Palermo, el Dr. Marco Miceli, el Dr. Salvatore Orlando y la Dra. Rosaria Bonito. Gracias por vuestra ayuda y por la experiencia que me ayudasteis a vivir.

Gracias también a todos los profesores y compañeros del departamento, especialmente a los Doctores David Montes, Maria José Fernández y Manuel Cornide, y a los que fueron mis compañeros de despacho durante la mayor parte de mi tiempo como doctorando, Miguel Ángel, Javier, Miriam y Hugo. Quiero tener también un recuerdo especial para mis compañeros de Licenciatura y de Máster, con quienes poco a poco fui recorriendo el camino que me ha conducido hasta donde me encuentro ahora mismo.

También quiero agradecer a mi familia el apoyo durante todos estos años. Muchas veces ellos han estado más convencidos de mis posibilidades que yo mismo. Así que gracias. Y muy especialmente, me gustaría agradecer a Laura lo que soy y lo que he hecho. Mis decisiones y mis éxitos más importantes se han producido a su lado y por estar ella al mío.

Finalmente, me gustaría agradecer al Proyecto AYA2011-29754-C03-03 y al Ministerio de Economía y Competitividad los fondos aportados para la realización de este estudio.

Madrid, 25 de abril de 2017

Acknowledgements

This thesis would not have seen the light without the help and advice of my thesis directors, Dr. Javier López Santiago and Professor Elisa de Castro Rubio. Thank you for giving me this chance and for staying by my side during this time. I would also like to have a special mention for those who welcomed me during my stay at the Osservatorio Astronomico Di Palermo, Dr. Marco Miceli, Dr. Salvatore Orlando and Dr. Rosaria Bonito. Thank you for your help and for the experiences I lived during those months.

Thanks also to all the professors and colleagues of the department, especially to Profs. David Montes, Maria José Fernández and Manuel Cornide, and to those who were my officemates during most of my time as a PhD student, Miguel Ángel, Javier, Miriam and Hugo. I also want to have a special memory for my Physics' Degree and Master's Degree colleagues, along with whom I have walked the path that has led me to where I am now.

I also want to acknowledge the support of my family during all these years. Many times, they have been more convinced of my possibilities than I was. So thanks. A very special mention deserves Laura, for what I am and what I have done. My decisions and my most important successes have occurred at her side and because she is at my side.

Finally, I would like to thank Project AYA2011-29754-C03-03 and the Ministerio de Economía y Competitividad for the funds provided for the realization of this study.

April, 25th 2017

Contents

List of Figures

List of Tables

Resumen

Contexto

La emisión procedente de los choques producidos por la interacción del viento de estrellas masivas y de los remanentes de supernova con el medio interestelar, revela que en estos procesos se liberan grandes cantidades de energía. En estos choques se aceleran protones y electrones que posteriormente, al enfriarse, emiten fotones. Si, además, la aceleración de partculas es lo suficientemente eficiente, los fotones radiados pueden alcanzar energías muy altas, e incluso ser detectados en las bandas de los rayos-X y rayos-γ.

Objetivos y metodología

El objetivo de este trabajo es estudiar los procesos de emisión no térmica que tienen lugar en los choques formados por diferentes objetos estelares. Para ello, partiendo de modelos anteriores, hemos elaborado un modelo no térmico capaz de explicar y reproducir dicha emisión.

En primer lugar, se han estudiado las observaciones en rayos-X, infrarrojo y radio disponibles para diferentes choques producidos por la interacción del viento de estrellas masivas con el medio interestelar, y los datos se han comparado con los resultados de nuestras simulaciones, lo que ha permitido calcular el valor de los diferentes parámetros que intervienen en los choques.

El modelo presentado en este trabajo tiene un carácter genérico. Por ello, hemos podido extender su uso a choques producidos por otros objetos estelares, como es el caso de la transición de supergigante azul a supergigante roja en las últimas fases evolutivas de algunas estrellas, en las que el choque es formado por la interacción de los vientos estelares expulsados en las fases posteriores a la secuencia principal. Para ello, usamos como referencia la estrella Betelgeuse y las simulaciones hidrodinámicas que sobre ella se han desarrollado.

Posteriormente, extendimos el estudio de la emisión a los choques formados por las explosiones de supernova. Particularmente, aplicamos nuestro modelo al remanente de supernova SN 1006, y comprobamos que se ajustaba a las observaciones en altas energías (tanto rayos-X como rayos-γ) que se tienen de esa supernova. Típicamente, el estudio de la emisión no térmica se ha basado en modelos paramétricos simples. Sin embargo, nosotros acoplamos nuestro modelo a simulaciones MHD en 3D que describen la evolución de la supernova, para predecir la emisión no térmica y la compararla con los datos observacionales.

Resultados y Conclusiones

En esta tesis doctoral se ha podido confirmar, a partir del desarrollo de un modelo teórico, que la emisión en altas energías detectada en algunos choques formados por estrellas O y B moviéndose a alta velocidad mientras atraviesan un medio suficientemente denso, tiene un origen no térmico, principalmente debido a procesos sincrotrón y Compton inverso del campo de radiación producido por el polvo interestelar en la región calentada por el choque. La emisión térmica del polvo en la región del choque, por el contrario, es dominante en el infrarrojo, lo que concuerda con las observaciones de estos mismos choques por el telescopio espacial WISE. Sin embargo, debido a que la luminosidad del choque en altas energías es baja, sólo se ha podido detectar emisión no térmica en este tipo de choques en estrellas cercanas a la Tierra (distancias menores a 500 pc), como en el caso de AE Aurigae. Por otro lado, nuestro modelo también ha sido capaz de explicar la no detección de fotones muy energéticos en otras estrellas observadas en rayos-X (como en el caso de la conocida BD+43 3654).

Por otro lado, nuestro modelo predice que durante la transición de supergigante azul a roja, los choques formados por las estrellas evolucionadas pueden producir emisión no térmica. Sin embargo, esta emisión sería aún más débil que la emitida por los choques de las estrellas O y B, reduciendo aún más la distancia a la que podríamos encontrar choques detectables en altas energías en el caso de las estrellas evolucionadas.

Finalmente, nuestro modelo también predice que la emisión en rayos-γ procedente del limbo suroeste del remanente de supernova de SN 1006 es originada por el proceso Compton inverso de los fotones del fondo cósmico de microondas junto a la contribución hadrónica de dos poblaciones de protones originadas en el remanente y en su interacción con una nube densa. Además, nuestro modelo no preveía emisión en la banda de los GeV, algo que fue confirmado posteriormente con los datos de Fermi, que no detectaron emisión en esa banda, lo que reforzó el origen mixto (leptónico y hadrónico) de la emisión en rayos-X y rayos-γ, descartando el origen puramente hadrónico o leptónico. No obstante, nuestro modelo también predice que en el limbo suroeste del remanente de supernova SN 1006 los fotones susceptibles de ser difundidos por Compton inverso puede que no sean únicamente los fotones del fondo cósmico de microondas, sino que es posible que exista una contribución de fotones térmicos a muy baja temperatura, si bien no hay observaciones que puedan confirmar nuestra predicción.

Abstract

Context

The emission from shocks originated from the interaction of massive stars and supernova remnants with the interstellar medium shows that great amounts of energy are released in these processes and that a significant part of it is radiated as high-energy photons. In these shocks, protons and electrons are accelerated and emit photons when they cool down. If particle acceleration is efficient enough, the radiated photons can reach very high energies and be detected in X- and γ-rays.

Objectives and methodology

The main objective of this work is to study the nonthermal emission processes that take place in shocks formed by different stellar objects. To do so, we have started from previous models to elaborate a nonthermal theoretical model able to explain and predict such emission.

First, X-ray, infrared and radio observations have been studied for different shocks produced by the interaction of the stellar wind of massive stars with the interstellar medium, and the data have been compared to the results of our simulations, which permits to determine the physical parameters of the particles accelerated at the shock front.

The model presented in this Thesis has a general approach. Thus, we also extended its application to the shocks produced by other stellar objects, as is the case of supergiant stars during the transition from blue to red supergiant at the late stages of some evolved stars, during which the shock is formed by the interaction of the stellar winds ejected in the post main-sequence stages. We used hydrodynamic simulations of Betelgeuse as a reference for our study.

Later, we extended our study to the emission from shocks formed by supernova explosions. Particularly, we apply our model to the Supernova Remnant SN 1006 to fit the observational data at high energies (X-rays and γ-rays) available for the remnant. Typically, the study of the nonthermal emission is based on simple parametric one-zone models. On the contrary, we coupled our nonthermal emission model to a 3D MHD simulation, which carefully describes the evolution of the supernova remnant, to predict the emission and then compare the results with the observational data.

Results and conclusions

In this Ph.D Thesis we confirm that, from the development of a theoretical model, the high-energy emission detected in some shocks formed by O and B stars moving at high velocities when traveling through a dense interstellar medium, has a nonthermal origin, mainly produced by synchrotron emission and inverse Compton of the radiation field produced by the interstellar dust heated by the shock. The thermal emission of the dust in the shock region, on the contrary, is dominant in the infrared, which is in agreement with the observations of shocks by the spatial telescope WISE. However, the luminosity of the shocks at high energies is low, and hence the nonthermal emission from these shocks has only been detected in stars close to the Earth (at distances shorter than 500 pc), as is the case of AE Aurigae. Our model is also able to explain the non-detection of other stars observed with X-ray telescopes (as in the case of the well known BD+43 3654).

On the other hand, our model predicts that during the transition from blue to red supergiant the shocks formed by evolved stars can produce nonthermal emission. However, this emission would be weaker than the emission from the shock formed by O and B stars. This reduces the distance at which shocks produced by evolved stars could be detected at high energies.

Finally, our model predicts that the γ-ray emission coming from the Southwestern limb of the SN 1006 is originated by the inverse Compton of the Cosmic Microwave Background photons, together with the hadronic contribution of two populations of protons originated in the remnant and their interaction with a dense cloud. Furthermore, our model predicts no emission in the GeV band, which was confirmed by the *Fermi* data and reinforces the mixed leptonic and hadronic origin of the X-ray and γ-ray emission, rejecting the pure hadronic or leptonic origin. Nevertheless, our model also predicts that in the Southwestern limb of the supernova remnant SN 1006, the photons that can be scattered by inverse Compton processes could be others than the Cosmic Microwave Background photons, and it could exist a contribution of thermal photons at a very low temperature, but no observations confirm this prediction.

Chapter 1

Introduction

1.1 The spectrum of the objects

For hundreds of years, astronomers have observed the Universe trying to understand the motion of the stars and the planets and the origin of the different astronomical objects. However, during many centuries, most of the advances in the field of the astronomy were reduced to observational studies of the objects. In the last decades, with the advance of the Quantum Mechanics and the Electromagnetic Optics, astronomers have been able to extend the study of the objets to the information codified in the light they emit: the decomposition of the light is now related to the chemical composition of the objects and to the different processes that take place in the wide variety of objects of the Universe. Hence, the light emitted by planets, stars or galaxies is not only a mere proof of the existence of those objects, but an incredible source of information of their present, past and future.

The radiation received from the different objects in different wavelengths is now the most powerful instrument to study the different physical phenomena originated in Universe. The decomposition of the light produces a spectrum that typically is formed by a continuum with overlapped lines. The energy received from an object per cm^2, per second and at a given frequency, ν, is known as the specific flux, and is denoted by f_ν. Hence, the total flux received from the object per cm^2 and per second can be computed from the sum of the flux at different frequencies, i.e.,

$$f = \int_0^\infty f_\nu d\nu. \tag{1.1}$$

According to this definition, the continuum corresponds to a function $f_\nu(\nu)$, that shows no important discontinuities and is defined for all frequencies. Overlapped to this continuum there could exist spectral lines that enhanced the emission at a given frequency or darken it. The first case corresponds to an emission line and the later case to an absorption line. The type of line observed depends on the type of material and its temperature relative to another emission source: a emission line is originated when an atom, molecule or electron make a transition from a high energy state to a lower energy state. The photon energy of the emitted photon is equal to the energy difference between the two states, and the intensity of light,

over a narrow frequency range, is increased due to emission by the material. On the contrary, an absorption line is produced when photons from a hot, broad spectrum source pass through a cold material, and hence the intensity of light, over a narrow frequency range, is reduced due to absorption by the material. Hence, emission and absorption lines give information about the temperature and composition of the different objects of the Universe.

However, the continuum of the spectra of the objects is also important . Typical examples of continuous spectra are the bremsstrahlung and thermal radiation, but also the synchrotron and inverse Compton emissions. In this case, the continuous spectrum can reveal the processes that are taking part in the different astronomical objects, and hence can explain the production of some of the photons observed from those sources. The origin of these processes that produce continuum spectra can be thermal or nonthermal:

- Thermal radiation may take the form of either thermal bremsstrahlung from an optically thin gas or of a blackbody radiation from an optically thick object. In the thermodynamic equilibrium between the emitting material and its radiation, the thermal spectrum corresponds to a black body emission, in which case the spectrum is independent of the emitting mechanism. The spectrum of the emitted radiation follows the Planck's Law (see Sec. 2.17), and depends only on the temperature. On the other hand, if charged particles are thermalized, following a Maxwell-Boltzmann distribution, thermal bremsstrahlung emission can be produced when those particles experience transitions between unbound states in the field of the nucleus: the moving particle loses kinetic energy, which is radiated as a photon. The change of the energy state of the particles produces electromagnetic radiation, and the aggregate of the photons emitted produces the thermal continuum. Common examples in Astrophysics of thermal continuum spectra are the emission from the interstellar dust, the intergalactic X-ray spectrum from clusters of galaxies or the Cosmic Microwave Background (CMB).

- Nonthermal radiation is an electromagnetic emission originated from particles that do not have a thermal energy distribution (i.e. that do not follow a Maxwell-Boltzman distribution). This radiation is detected from many objects such as supernovae, pulsars, radiogalaxies, Gamma-Ray Bursts. Synchrotron, inverse Compton, relativistic bremsstrahlung (as leptonic processes) and π^0 decay (as hadronic process) are the main nonthermal processes [see e.g Aharonian, 2004; Kellermann & Verschuur, 1988]:

  a) Synchrotron: the trajectory of a charged particle under the influence of a magnetic field is helicoidal. Hence, the particle has an acceleration, and charged particles that are accelerated emit radiation. The set of photons emitted by accelerated charged particles is the Synchrotron continuum, which is typically observed in radio wavelengths. The energy of synchrotron photons are much less than the energy of parent electrons. In certain astrophysical environments, the synchrotron radiation is a major photon production process (see Sec. 2.2.1).

b) Inverse Compton (IC): photons can interact with other particles and these particles can transfer part of their energy to the photons, thus increasing their frequency. The interaction of relativistic electrons with radiation fields through IC scattering provides one of the principal γ-ray production processes in Astrophysics. It works from compact objects like pulsars and AGN to extended sources like supernova remnants. The presence of the CMB causes the IC to be very efficient in the intergalactic medium over the entire high-energy and very high-energy ranges. IC radiation is generated when relativistic electrons collide with low-energy photons. The electrons lose kinetic energy, which is transferred to the photons. More formally, IC scattering is the up-scattering of photons by electrons, in opposition to the well known Compton effect, which is the scattering of electrons by photons (see Sec. 2.2.2).

c) Nonthermal bremsstrahlung: is considered as radiation of decelerating electrons in the Coulomb field of an ion. The process is the same as the thermal bremsstrahlung, but electrons do not follow a Maxwell-Boltzmann distribution, but a nonthermal distribution of energies, e.g., a power law distribution of energies (see Sec. 2.3).

d) π^0 decay: proton-proton inelastic collisions can produce neutral and charged pions. Neutral pions can later decay producing two γ photons. Traditionally, this process has ben considered the most important γ-ray production mechanism.

Nonthermal emission processes have been reported to have a major role in the production of high-energy photons. In particular, Benaglia et al. [2010], del Valle & Romero [2012] and Terada et al. [2012], among others, concluded that synchrotron and IC processes could be responsible for the high-energy photons emitted from bow shocks formed by runaway stars; on the other hand, Berezhko et al. [2002], Acero et al. [2010] or Miceli et al. [2013] also pointed out that nonthermal processes may be the responsible for the high-energy photons detected from supernova remnants.

1.2 Nonthermal photon sources in this work

As explained above, bow shocks from runaway stars and supernova remnants are sites where nonthermal emission has been reported to take place. In this thesis we study the nonthermal emission from bow shocks formed by different runaway stars and from the supernova remnant of SN 1006.

- Bow shocks occur around many classes of astrophysical sources: pulsars, cataclysmic variables, colliding wind binaries, cometary H II regions, and even in groups and clusters of galaxies. Here we focus on stars with high peculiar velocities that may produce perturbations in the surrounding ambient medium. O and B stars have strong winds that can sweep relatively large amounts of gas and dust. When these stars move supersonically through the interstellar medium (ISM), the material is piled up forming bow shocks, arc-shaped

structures with bows pointing in the same direction as the stellar velocity [Benaglia et al., 2010]. Stellar winds are confined by the ram pressure of the ISM at distances from the star determined by momentum balance. The shocked material is heated by the stellar radiation field and the dust re-emits at infrared wavelengths. Many infrared bow shocks have been observed around runaway stars (stellar objects that were ejected from their place of origin by dynamical processes and travel through the ISM at high velocities, see Sec. 3.1). Examples are given in Peri et al. [2012].

The collision of the supersonic stellar wind with the ISM results is a system of two shocks: the forward and the reverse shocks. The forward shock propagates in the same direction of the star and at the same velocity. The stellar wind can be considered as a continuous power source, therefore both shocks reach a steady state. The reverse shock propagates in the opposite direction of the stellar motion at a velocity similar to the stellar wind and can accelerate particles up to relativistic energies by the Fermi mechanism (see Sec. 2.1), and then particles can cool by the nonthermal processes explained above, producing nonthermal radiation. This radiation may be detected in radio, X-ray and γ-ray energy bands.

- In the last years, significant efforts have been made to obtain direct observational evidence whether Galactic cosmic rays are generated in supernova remnants (SNRs). These remain the most likely sources of Galactic cosmic rays since particles can be accelerated up to very high energies at the SNR shock surface. The High-Energy Stereoscopic System (*H.E.S.S.*) is an array of Cherenkov telescopes which confirmed that many Galactic SNRs are associated with very high-energy sources [Fernandez et al., 2013]. TeV γ-ray emission has been detected from SNR sources, but the interpretation of the data is not unique: depending on the assumed values for the unknown physical parameters of SN 1006, the observed high-energy γ-ray emission can be predominantly either inverse Compton radiation due to electrons scattering CMB photons, or π^0 decay emission due to hadronic collisions [Berezhko et al., 2002].

The velocities of the stellar winds reach a few thousands of kilometers per second, which is comparable with the shock speed of young supernova remnants [Bamba et al., 2005]. The literature confirms that nonthermal processes take place in bow shocks from runaway stars and in SNRs [see, e.g., Acero et al., 2010; del Valle & Romero, 2012].

1.3 The influence of the magnetic field in the motion and acceleration of the charged particles.

Nonthermal emission is produced by particles that have a nonthermal distribution, i.e., do not follow a Maxwell-Boltzmann distribution. In particular, the dynamics of the charged particles that produce nonthermal emission is very influenced by the

magnetic field. Hence, the study of the nonthermal processes can not be understood without the presence of magnetic fields, whose study is a major requirement in many astrophysical events, and also plays an important role in the High-Energy Astrophysics. Specially, the magnetic fields play an important role in the acceleration of the charged particles that produce the synchrotron and the inverse Compton processes that generate part of the observable continuum from different astronomical objects.

The dynamics of the plasma in the stellar wind is dominated by the magnetic fields originated by the activity of the stars. At the same time, the motion of the plasma also influence the evolution of the magnetic field. The magnetic field is represented by the strength lines, also called magnetic field lines, which are tangent to the magnetic field, $\vec{B}$. Hence the magnetic field lines move as the field evolves.

The magnetic field affects the motion of charged particles as generates a force, called the Lorentz Force, given by

$$\vec{F} = q\Big(\frac{\vec{v}}{c} \times \vec{B}\Big) \tag{1.2}$$

where q is the charge of the particle, $\vec{v}$ is its velocity and c the light speed. The force is perpendicular to $\vec{v}$ and $\vec{B}$, but if the velocity is parallel to $\vec{B}$, then the particles move along the field lines.

According to the Maxwell equations, magnetic lines are born in the infinite, or die in the infinite, which can be expressed as $\nabla \cdot \vec{B} = 0$. On the other hand, the induction law of Faraday describes the temporal evolution of the magnetic field:

$$\frac{\partial \vec{B}}{\partial t} = -c\nabla \times E, \tag{1.3}$$

which implies that the rotation of the electric field lines defines the evolution of the magnetic field.

When densities are low, electrons can move easily, and if the ionization is high, as in the case of the stellar atmospheres, the conductivity is thus very high. When the density grows, as happens in regions where a shock compresses the plasma, the magnetic lines come together and hence the module of the magnetic field strength also increases, and so do the magnetic energy density. When gradients of magnetic energy density appears, there exists a pressure to reduce the gradient. Hence, the magnetic energy density also influence the movement of charged particles. Furthermore, the anisotropies of the magnetic field also influence the motion of the particles, scattering them.

1.4 Scope of this Thesis and Chapter description

In the last decades, the acceleration mechanism that has been considered in astrophysical studies is the diffusive shock acceleration, also known as the Fermi first-order mechanism (see Sec. 2.1). As particles pass through the shock in either direction, they are scattered due to magnetic inhomogeneities, gaining energy.

Bow shocks from runaway stars and supernova remnants are ideal sites for particle acceleration, and hence nonthermal emission processes can take place in those acceleration sites. Under this scenario, protons and electrons can cool trough different processes and the energy they lose can be emitted as photons. When charged particles have gained enough energy, the emitted photons can reach very high energies and hence be detected in the X-ray and γ-ray bands. Such detections would reveal the presence of efficient acceleration sites and also the existence of very energetic shock processes.

In this work we aim at developing a nonthermal model that can explain de observational data at high energies from different stellar objects with different physical parameters that intervene in the shock formation and in the particle acceleration process. The scenario is different for each object, and hence changes the treatment of the theoretical model we aim to develop, which justifies the divisions between chapters, namely:

- Chapter 2: Cooling processes.
- Chapter 3: Bow shocks from runaway stars.
- Chapter 4: Nonthermal emission from supernova remnants.
- Conclusions and future work.

1.4.1 Cooling processes.

In Chapter 2 we present the cooling rates of the different nonthermal processes considered. By cooling rates we refer to the time a particle of a given energy needs to cool completely by that process. The nonthermal processes considered are the synchrotron, the inverse Compton, the relativistic bremstrahlung, and the proton-proton inelastic collisions. The different values of the parameters that influence the shock formation will determine the cooling process that dominates over the other processes.

Once the expressions of the cooling time rates are presented, the particle energy distributions for protons and electrons can be computed, i.e., it can be derived the expression that specifies the number of electrons present in the shock per energy range, and that determines the particles that will produce nonthermal emission during the cooling phase. Also is discussed the derivation of the expression of the energy distributions in those cases where the cooling of particles is not efficient enough.

Finally, the expressions of the luminosities produced by the different nonthermal processes are derived, both leptonic and hadronic . These expressions produce the spectra we referred in Sec. 1.1. Also is considered the thermal emission to compare it with the nonthermal radiation in the different objects; in particular, the expressions for the thermal emission from a black body and the thermal bremstrahlung are studied.

1.4.2 Bow shocks from runaway stars.

We first apply the expressions derived in the previous chapter to the shocks formed by stars when interacting with the interstellar medium. In particular, the runaway stars, which are stars that move supersonically trough the surrounding medium and are able to produce a bow shock in the direction of their motion.

First, the different theoretical mechanisms that explain the ejection of runaway stars are presented, namely, the interaction with its binary exploiting into a supernova star or the dynamical interaction with other stars.

Second, the structure and the configuration of the shock parameters are shown. The shock parameters depend on the stellar wind parameters and on the interstellar medium density the stars are traveling through.

The model is then applied to particular cases. The first one is the shock formed by the star AE Aurigae, which is the first star in which X-ray nonthermal emission from a shock has been detected [López-Santiago et al., 2012]. Here we show that the inverse Compton of the infrared photon field present in the shock region is the responsible for the high-energy photons detected. Then, the model is applied to the case of BD+43 3654 to explain the absence of X-rays from it.

Later, we apply our model to an evolved star using the hydrodynamic simulations from Mackey et al. [2012], that studied the final phases of the evolution of the red giant star Betelgeuse. We show that during the transition phase from blue supergiant to red supergiant, nonthermal photons can be emitted.

Last, we consider the bow shocks formed by the runaway stars in the catalog from Peri et al. [2012]. X-ray counterparts have been searched with no results in most cases. Hence, we discuss different possibilities for each star starting off a grid of simulations for different values of the electron injection index, the terminal velocity, the mass loss rate and the velocity of the stars and the surrounding medium density.

These results were published in [López-Santiago et al., 2012] and [Pereira et al., 2016].

1.4.3 Nonthermal emission from supernova remnants.

In chapter 4 we try to explain the high-energy emission detected from the Southwestern limb of the supernova remnant of SN 1006. We study the structure of the limb and explore de conditions that can lead to a detectable nonthermal emission.

From the magnetohydrodynamic simulations from Orlando et al. [2012] we select the cutoff values of the proton energy distributions. In particular, we consider two proton populations, one corresponding to the remnant and one originated in the interaction of the remnant with a dense cloud. From the simulations we also select the total energy of each population, according to the interacting volumes. From this study we conclude that the γ-ray observations can not be explained by only considering hadronic processes.

We then also study the inverse Compton of the CMB photons. We show that this leptonic process is the dominant process, and that the total high-energy emission can be explain as a contribution of leptonic and hadronic processes. On the other

hand, if only CMB photons are considered, low magnetic field strengths are required to be present in the remnant acceleration region.

These results were published in [Miceli, M., Orlando, S., Pereira, V. et al., 2016].

Chapter 2

Cooling processes

2.1 Acceleration of high-energy particles

From the detection of cosmic rays in the atmosphere to the observation of synchrotron emission from thousands of astrophysical sources, particles can be accelerated by different physical processes through many different channels of interaction. The acceleration mechanisms may be classified as dynamic (lets say, for example, when particles are accelerated by collisions), hydrodynamic (such as the accelerations of whole layers of plasma), and electromagnetic [Longair, 2011]. For our work we consider only the Fermi acceleration mechanism, which belongs to the last type of the acceleration mechanisms listed. Here we consider the Fermi second-order mechanism (in the environment of moving magnetized gas clouds) and the Fermi first-order mechanism (in shocks), also known as diffusive shock acceleration:

- Fermi second-order mechanism:

  Qualitatively, this mechanism can be understood considering than in shock acceleration region magnetic inhomogeneities, called magnetic mirrors, are found. Charged particles are traveling through the shock wave from upstream to downstream (see Fig 2.1), and when they encounter these magnetic mirrors* they are reflected back through the shock at an increased velocity. To illustrate one of the most important consequences of this mechanism, which produces a power-law distribution of particle energies, lets assume that a charged particle moves at a velocity $v \approx c$ and that the magnetic mirrors or inhomogeneities move randomly at a velocity V. The average energy gain per collision (averaging over all pitch angles, which are the angles between the initial direction of the particle and the normal to the surface of the mirror) is [see Longair, 2011]

*The magnetic mirror is a moving magnetized cloud. In it, a specially shaped electromagnet creates a configuration of magnetic field lines which reflects charged particles from a high density magnetic field region to a low density magnetic field region. In a random motion environment, according to Fermi, the probability of a head-on collision is greater than a head-tail collision, so particles would, on average, be accelerated [Fermi, 1949].

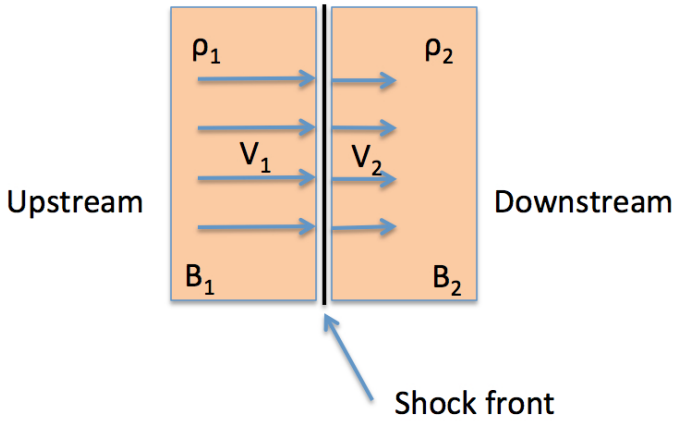

Figure 2.1: Shock front in the reference frame in which it is at rest.

$$\left\langle \frac{\Delta E}{E} \right\rangle = \frac{8}{3}\left(\frac{V}{c}\right)^2 \tag{2.1}$$

When particles remain within the acceleration region during some characteristic time τ_{esc} (up to the time they can scape from the acceleration region), they engage a chain of reflections, and in each collision they increase their energy the same fraction, which leads to an exponential increase in the energy of the particles.

Faster random velocities, V, are more efficient in accelerating particles. In the case of interstellar clouds in the Galaxy, $V/c \leq 10^{-4}$, and also the mean free path is of the order of 0.1 pc, resulting in a very slow gain of energy by particles. The term $(V/c)^2$ makes this process to be known as the Fermi second-order mechanism.

- Fermi first-order mechanism

  A different process that has leaded the astrophysical studies in the last decades is the diffusive shock acceleration. Shock waves typically have moving magnetic inhomogeneities both preceding and following them. To particles undergo Fermi first-order acceleration, the presence of strong shock waves and the velocity vector of high-energy particles is randomized on either side of the shock, are needed. The particles are assumed to be propagating at speeds close to c and so the velocity of the shock is very slow compared to those of the particles. As particles pass through the shock in either direction, they are scattered due to the magnetic inhomogeneities, and their velocity distribution becomes isotropic on either side of the shock. In this case, the average gain of energy uncrossing the shock and back again is

$$\left\langle \frac{\Delta E}{E} \right\rangle = \frac{4}{3}\frac{V}{c}, \tag{2.2}$$

a first order in V/c which is referred to as first-order Fermi acceleration mechanism.

In this work we study the nonthermal processes that take place in the collisionless shock waves of a supernova explosion or in the bow shocks formed by runaway stars (see Secs.3 and 4). These environments are ideal scenarios for Fermi first-order acceleration of charged particles [Bell, 1978]. The resulting energy spectrum of these particles undergoing the Fermi first-order mechanism is a power-law distribution of the form

$$Q(E) = Q_0 E^{-\alpha} \text{ cm}^{-3} \text{ erg}^{-1} \text{ s}^{-1}, \tag{2.3}$$

where Q_0 is a normalization constant and α is the particle injection index. . On the other hand, the time needed to accelerate a particle up to an energy E is given by [Drury, 1983]

$$t_{acc} = \frac{3}{V_1 - V_2}\left(\frac{D_1}{V_1} + \frac{D_2}{V_2}\right) \tag{2.4}$$

where $V_{1,2}$ and $D_{1,2}$ are the upstream/downstream velocities and the diffusion coefficients, respectively. If we consider the Bohm limit, i.e., the smallest diffusion coefficient allowed by the standard model of particle diffuse transport, then $D = Ec/3eB$, where B is the magnetic field of the acceleration region. On the other hand, the equation of continuity requires mass to be conserved through the shock, and so considering that the densities upstream and downstream the shock are ρ_1 and ρ_2 , then $\rho_1 V_1 = \rho_2 V_2$. In the case of strong shocks the relation between the densities at both sides of the shock is

$$\frac{\rho_2}{\rho_1} = \frac{\gamma + 1}{\gamma - 1} \tag{2.5}$$

where γ is the ratio of specific heat capacities of the gas. For a monatomic or fully ionized gas, $\gamma = 5/3$, which leads to $V_1 = 4V_2$ (Fig 2.1). [Miceli et al., 2013] showed that in the southwestern limb of the supernova remnant SN 1006 the compression ratio is higher than 4 and the relation between the upstream and the downstream magnetic fields is $B_2 = \sqrt{11}B_1$ due to the compression enhances the magnetic field in the downstream region. Hence, under these assumptions, the acceleration time rate can be expressed as function of the upstream parameters as

$$t_{acc} = \frac{3Ec}{V_1^2 eB_1}. \tag{2.6}$$

Hereafter V_1 and B_1 will be V and B, the shock velocity and the magnetic field in the acceleration region, respectively.

Nevertheless, we have to note that the Bohm limit is a theoretical minimum that not necessarily has to be fulfilled, and hence a proportional factor could be included, which would increase the time needed to accelerate a particle up to an energy E.

We can derive another approximation of the same order of magnitude considering the Hillas criterion [Hillas, 1984], which postulates that to accelerate particles to

high energies the acceleration region must be at least twice the Larmor* radius. Then, the time a particle has to survive in the acceleration region to be accelerated up to an energy E is $t_{acc} \sim r_L/c$, where r_L is the Larmor radius defined by $r_L = E/eB$. From Drury [1983], the acceleration efficiency is $\eta \sim r_L c(V/c)^2/3D$. Thus, the acceleration time can be defined as

$$t_{acc} = \frac{3E}{\eta eBc}, \tag{2.7}$$

which, in fact, is the same as Eq. 2.6.

However, now that we have explained an effective mechanism to accelerate particles, a new question arises: up to what energy can particles be accelerated to? According to the Hillas criterion, the size of the acceleration region, L, must be at least twice the Larmor radius, so then $L > 2r_L = 2E/eB$, and hence

$$E < 150BL \text{ eV}, \tag{2.8}$$

where B is expressed in Gauss and L in cm.

The Hillas criterion sets the maximum energy of the charged particles. However, we will see that the maximum energy will be given by the point where the acceleration time rate and the time rate of the most efficient cooling process equalize (see section 2.2.5), with also has to fulfill the Hillas criterion. On the other hand, the minimum particle energy that we consider is twice the rest mass energy of the particle, $2mc^2$. For electrons, this energy is 10^6 eV, and for protons is 5×10^9 eV.

2.2 Nonthermal cooling losses

Protons and electrons in the acceleration region are accelerated by the Fermi first order mechanism described in the previous section. However, these particles undergo different cooling processes which lead to nonthermal emission. Electrons can cool mainly by synchrotron radiation, inverse Compton scattering (IC) and relativistic Bremstralung, while the most relevant proton cooling process for our purposes is the proton-proton inelastic collisions. By nonthermal emission we refer to the continuum radiation of a distribution of particles with a non-Maxwellian energy spectrum, or, more generally, when the spectrum cannot be accounted for by the spectrum of thermal bremstrahlung or black-body radiation.

Each of the processes mentioned produce an energy loss per second represented by dE/dt, and so charged particles with energy E cool down in a time $t_{cool} = E/|dE/dt|$. This time rate t_{cool} can be understood as the time a particle needs to lose all its energy by an specific cooling process. However, in shorter time scales particles can lose a fraction of their energy and hence emit nonthermal radiation as well. In this section we aim to present the expressions of the cooling time rates for different nonthermal processes.

*The radius of the circular motion of a charged particle in the presence of a uniform magnetic field.

2.2.1 Synchrotron cooling rate

When electron move perpendicular to a magnetic field with a velocity $\vec{v}$, the Lorentz force (eq. 1.2) appears and is perpendicular to the magnetic field and the velocity of the particle. This force is compensated by the centrifugal force in the reference frame of the electron, and hence results that

$$\frac{evB}{c} = m_e \frac{v^2}{r}. \tag{2.9}$$

However, if the velocity is parallel to $\vec{B}$, the Lorentz force does not appear and hence the particle continues with a uniform movement. Nevertheless, a real particle is more likely to have a composition ob both types of movement, and will follow an uniform movement and a turn around $\vec{B}$, ant the composition of movements is known as a helical trajectory. Charged particles describe a helical movement along the magnetic field lines. In this movement, as the electrons do not follow a rectilinear trajectory, an acceleration appears, and accelerated electrons emit electromagnetic radiation [see e.g. Ginzburg & Syrovatskii, 1965, 1969], losing part of their energy along their line of motion (see Fig. 2.2). The emission is isotropic in the reference system of the electron but for an observer moving with a non-relativistic velocity, the emission is produce in a narrow solid angle proportional to γ^{-1} (where γ is the Lorentz factor), as cone shape. From Earth, only the radiation produce in the direction perpendicular to the magnetic field can be observed.

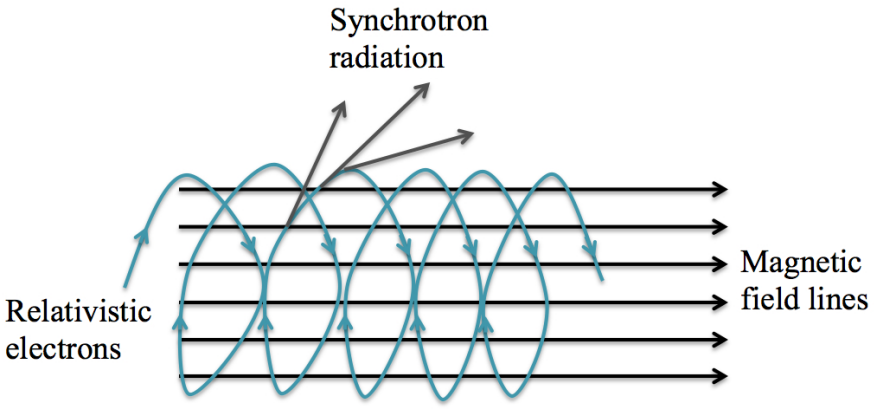

Figure 2.2: Mechanism of synchrotron radiation.

Synchrotron emission is gyromagnetic emission from highly relativistic electrons. This radiation of ultra-relativistic electrons dominates much of high-energy astrophysics. Is the process responsible for the background radio emission of our Galaxy, of supernova remnants and extragalactic radio sources. But it can be also responsible for the continuum optical emission of the Crab Nebula and also of the X-ray emission from other objects, as in the the supernova remnant SN 1006.

The synchrotron losses carry away small amounts of the electron energy. Assuming an isotropic distribution of pitch angles for a population of high-energy

electrons, the electron energy losses per second are thus given by [e.g., Rybicki & Lightman, 1979]

$$\frac{\mathrm{d}E}{\mathrm{d}t} = -\frac{4}{3}\sigma_T c u_B \gamma^2 \left(\frac{v}{c}\right)^2, \tag{2.10}$$

where $u_B = B^2/8\pi$ is the magnetic energy density given before, σ_T the Thomson cross section and $\gamma = E/m_e c^2$. Therefore, the synchrotron cooling time rate, i.e., the time an electron of energy E needs to cool completely by synchrotron losses, is

$$t_{sync}(E) = \frac{6\pi m_e^2 c^3}{\sigma_T B^2 E}. \tag{2.11}$$

Is easy to show that the more intense is the magnetic field, the more intense in the energy emitted, as well as the less massive are the particles. Furthermore, the radiation emitted by electrons is about 2000 times greater than the emission from protons of the same energy, and hence we referring to synchrotron emission, usually only electrons are considered. On the other hand, from the last equation is also clear that electrons with very high energy E spend their energy is timescale much shorter than electron with lower energies, because their lifetime is very short, and hence most of the radiation is dominated by low-energy electrons, that emit in the radio wavelengths.

2.2.2 Inverse Compton

Inverse Compton (IC) radiation is generated when ultrarelativistic electrons collide with low-energy photons. The electrons loss kinetic energy, which is transferred to the photons. More formally, IC scattering is the scattering of photons by electrons, on opposition to the well known Compton effect, which is the scattering of electrons by photons. The scattering of photons by non-relativistic electrons is called Thomson scattering.

Adams [1980] demonstrated that the relation between the energy of a photon before being scattered (ε) and the energy of the scattered photon (ε_1), considering collisions at different angles, is $\varepsilon_1 \backsimeq \gamma^2 \varepsilon$. Some typical photon fields to be scattered by electrons that are usually considered are the cosmic microwave background (CMB) and the starlight photons. CMB photons peak at 160.2 GHz ($\varepsilon = 10^{-4}$ eV), and hence would have to interact with 3.2 GeV electrons ($\gamma = 6300$) to produce, for example, 4 keV X-rays. However, starlight photons with $\nu = 6 \times 10^{14}$ Hz ($\varepsilon = 0.4$ eV) would just need to collide with electrons of 51 eV ($\gamma = 100$) to produce the same X-ray photons as before.

In Fig. 2.3 is represented the energy of the IC scattered photon (ε_1) as a function of the field photon (ε) and the electron energy (E). Electrons over 50 GeV are able to scatter even low-energy photons up to gamma-ray energies. We expect strong shocks to be able to accelerate electrons over a few GeV, and hence produce gamma emission by IC scattering. On the other hand, it is clear that the IC is revealed as an effective mechanism to produce X-rays photons, since even electrons with energies a few times the electron rest energy can scatter the milimetric and submilimetric photons up to X-ray energies.

The theoretical treatment of the IC requires more considerations than the synchrotron process. If the photon energy before being scattered is much less than the electron rest energy, the Thomson scattering cross-section, which is independent of the energy of the incoming photons, can be used to describe the probability of scattering. In this case the electron loses a small fraction of its energy in each interaction. The opposite case, where the energy of the photon is much bigger than the electron energy rest, corresponds to the Klein-Nishina limit, and the photon carries away a large fraction of the electron energy. The electron rest energy is 0.5 MeV, and photons with the same energy are gamma photons, which are not the field photons. Consequently, the IC scattering may be treated as Thomson scattering, and its loss rate can be expressed by

$$\frac{\mathrm{d}E}{\mathrm{d}t} = -\frac{4}{3}\sigma_T c u_{rad} \gamma^2 \left(\frac{v}{c}\right)^2, \tag{2.12}$$

and hence the cooling time rate can be calculated as $t_{IC} = E/|dE/dt|$, i.e.,

$$t_{IC}(E) = \frac{3m_e^2 c^3}{4\sigma_T u_{rad} E}. \tag{2.13}$$

However, although we only consider low-energy photon fields, there is another case were the quantum relativistic cross-section has to be used: when the electron moves ultra-relativistically with $\gamma \gg 1$. In this case, the inverse Compton losses are generally determined following the derivations of Blumenthal & Gould [1970], who

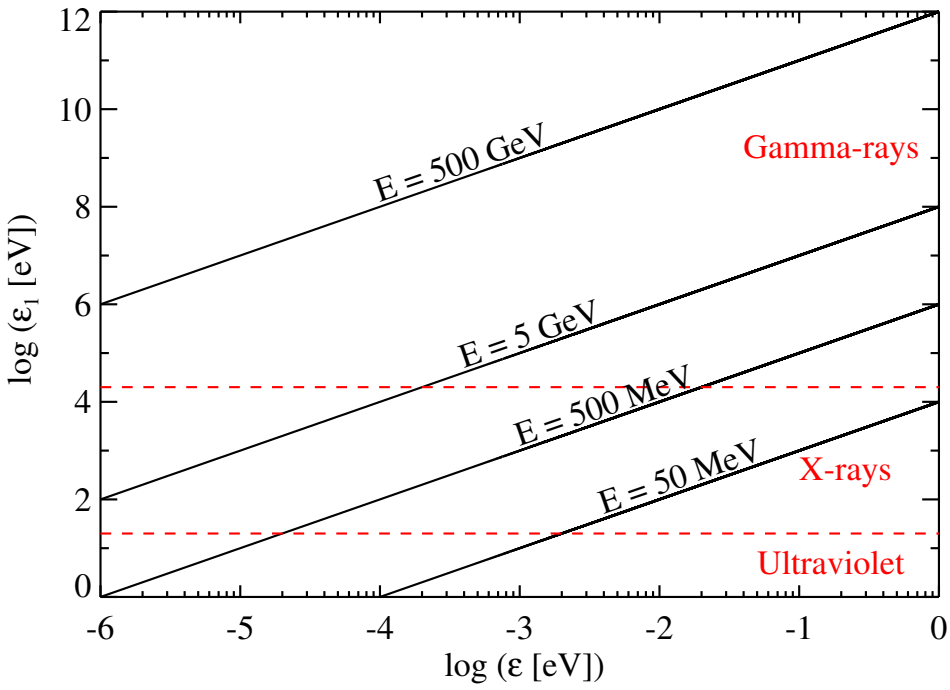

Figure 2.3: Energy of the scattered photons (ε_1) as a function of the photon field energy (ε) and the incident electron energy (E).

take into account the Klein-Nishina cross-section. Here we consider that electrons can be accelerated up to energies of 10^{12} - 10^{13} eV in strong shocks, and hence the ultra-relativistic condition is fully accomplished (for lower energy electrons, Thomson treatment is enough). Thus, Eq. 2.12 must be corrected.

Bosch-Ramon & Khangulyan [2009] and Peri [2010] proposed a good approximation (with a difference of less than a 3% of the Bloumentan & Gould expressions) which is still valid in both regimes (Thomson and Klein-Nishina), given by

$$t_{IC}(E) = 6.1 \text{ x } 10^{12} \frac{\varepsilon}{u_{rad}} \frac{(1+8.3y)}{\ln(1+0.2y)} \frac{(1+1.3y^2)}{(1+0.5y+1.3y^2)}, \tag{2.14}$$

where $y = \varepsilon E/(m_e c^2)^2$ and ε is the energy of the target photons at a temperature T, i.e., $\varepsilon = kT$. The term u_{rad} is the energy density of radiation of the photon field. For the case of runaway bowshocks, we consider the starlight photons at a distance R_0 from the star, the infrared radiation from the heated shocked dust and the CMB photons.

The infrared photons are considered to follow a black body law at a temperature T, which was calculated by Draine & Lee [1984] considering that dust grains are heated by the starlight and cool by radiating in the infrared:

$$T_{\rm IR} = 27 \; a_{\mu m}^{-1/6} L_{\star 38}^{1/6} R_{0pc}^{-1/3} \text{ K}, \tag{2.15}$$

where $L_{\star 38}$ is the luminosity expressed in units of 10^{38} erg s^{-1}. We can adopt a dust grain radius of $a_{\mu m} \sim 0.2$ μm. For the starlight photon field the temperature is given by the stellar temperature, $T_\star$.

Further expressions are needed to find the number of photons at energy ε emitted by a black body at temperature T, per unit of energy and volume. A black body is a system of photons in thermodynamic equilibrium, and is characterized by two properties: the firs is the isotropy, which means that any photon can move in any direction with the same probability. The second property is that the photon density follows a the expression

$$n_{ph}(\varepsilon) = \frac{4\pi}{c} I_{\rm BB}(\varepsilon) \text{ erg}^{-1}\text{cm}^{-3}, \tag{2.16}$$

where $I_{\rm BB}$ is the intensity given by the Planck's function,

$$I_{\rm BB} = \frac{2\varepsilon^2}{h^3 c^2} \frac{1}{\exp(\varepsilon/kT) - 1} \text{ erg}^{-1}\text{s}^{-1}\text{cm}^{-2}. \tag{2.17}$$

The intensity is the same in all directions but depends on the frequency These expressions are valid for the infrared photons because the emission is produced in the shock and for the CMB photons ($T = 2.725$ K), but for the starlight photons a correction must be done since the emission is produced by a spherical layer and the density of photons decreases with distance:

$$n_{ph\star} = n_{ph} \frac{R_\star^2}{R_0^2} \text{ erg}^{-1}\text{cm}^{-3}, \tag{2.18}$$

where $R_\star$ is the stellar radius.

To compute the energy density, i.e., the total energy per unit of volume, we propose to integrate $n_{ph}(\varepsilon)$ (or $n_{ph\star}(\varepsilon)$) over the energy range of the field photons:

$$u_{rad} = \int_0^\infty n_{ph}(\varepsilon)\varepsilon d\varepsilon \text{ erg cm}^{-3}. \tag{2.19}$$

In Fig 2.4 we compare the differences between both regimes. The IC cooling time rate for low-energy electrons is well describe by both the Thompson and the Klein-Nishina regimes. Dust and CMB photons have very low energies, and hence the differences between the both regimes are only evident at very high electron energies, at about 1TeV. However, starlight photons are much more energetic, and hence the Klein-Nishina correction acts at lower energies, at about 10 GeV.

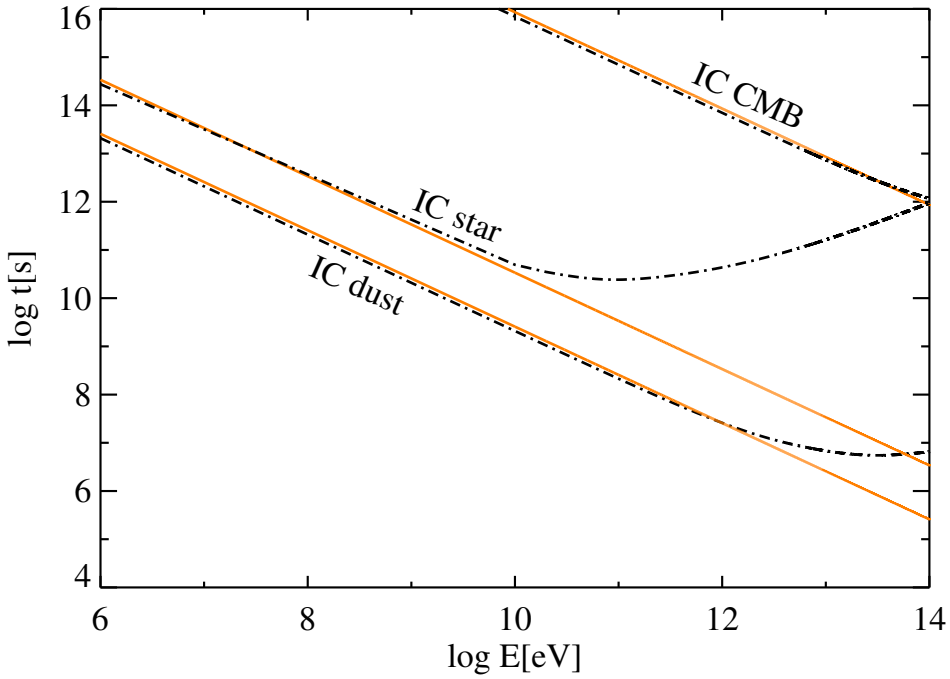

Figure 2.4: Thomson and Klein-Nishina regimes comparison for an arbitrary set of parameters. Straight orange lines represent the IC cooling rates considering the Thomson treatment; the dashed-dotted black line represents the IC in the Klein-Nishina regime. The Klein-Nishina treatment is also valid for the low-energy electrons, achieving a good level of accuracy. For high-energy electrons, only the Klein-Nishina formulation must be considered.

2.2.3 Relativistic Bremstrahlung

The energy loss rate for relativistic electrons around atomic nucleus are underestimated if only the ionization losses are considered. Relativistic bremsstrahlung is called to be of importance in astrophysics. The process is referred to electromagnetic radiation produced by the deceleration of a charged particle when deflected

by another charged particle: in the cases we consider, an atomic nucleus. The moving particle loses kinetic energy, which is radiated as a photon. The spectrum of these radiation is continuous spectrum whose peak intensity shifts toward higher frequencies as the change of the energy of the decelerated particles increases. The emission corresponds to transitions between unbound states of the electron in the field of the nucleus, a process known as free-free emission. Electrons of energy E can interact with atoms and molecules to generate photons with average energies of $1/3E$ [Longair, 2011]. However, among the processes considered here, relativistic Bremsstrahlung losses are the less important leptonic losses, although for completeness we consider its presence in our computations.

The bremstrahlung cooling time rate for a complete ionized plasma, given by Berezinskii et al. [1990], is

$$t_{Br}^{-1} = 4nZ^2 r_e^2 \alpha c \Big[\ln \frac{2E_e}{m_e c^2} - \frac{1}{3} \Big], \tag{2.20}$$

where n represents the density of the target ions of the shocked stellar wind, which is four times the wind density for a strong shock approximation [Landau & Lifshitz, 1959]; it can be obtained from $n_{\rm ISM} v_\star^2 \sim n_w v_w^2$ since the standoff radius is formed where the ram pressure of both the ISM and the wind reach the equilibrium. Considering a medium mainly composed by H I, $Z = 1$; r_e is the classical electron radius and α is the fine structure constant.

2.2.4 Proton-Proton inelastic collisions

The three previous cooling losses considered correspond to leptonic losses, but the proton-proton (p-p) production of gamma rays through inelastic collisions is a process that traditionally has been though as one of the major causes of the high-energy emission in the galaxy [see e.g., Kelner et al., 2006]. These collisions can produce neutral and charge pions, which can decay in the following products:

$$\pi^0 \rightarrow \gamma\gamma$$

$$\pi \rightarrow \mu\nu_\mu$$

and later, muons can decay producing secondary electrons,

$$\mu \rightarrow e\nu_e\nu_\mu.$$

These secondary electrons can undergo the same processes as the primary electrons.

Neutral pions decay in two gamma photons, and hence p-p collisions is revealed as one of the most important γ-ray production mechanism.

Protons lose all their energy by p-p collisions in time scales of [del Valle & Romero, 2012]

$$t_{pp}^{-1} = nc\sigma_{inel} K_{pp}, \tag{2.21}$$

where n is the density of the target protons ($n \sim 4n_w$), K_{pp} is the inelasticity (~ 0.5) and σ_{pp} the cross section of the inelastic p-p collision given by Kelner et al. [2006],

$$\sigma_{inel} = 10^{-27}(34.3 + 1.88L + 0.25L^2)\ \mathrm{cm}^2, \tag{2.22}$$

where $L = \ln(E_p \times 10^{-12})$. This expression is valid for proton energies > 0.1 TeV. For lower energies a correction factor $[1 - (E_{th}/E_p)^4]^2$ is needed, where $E_{th} = 1.22$ GeV is the threshold energy of π^0-mesons production.

2.2.5 Energy limits

Electrons and protons are accelerated in the shock region. In the previous section we studied the cooling processes these charged particles can lose energy by. It is important to note that they can neither lose more energy than that they reach during the acceleration process, nor lose energy below their rest mass energy. We consider the minimum energy to be twice the rest mass energy of the particle, i.e. $2mc^2 = 10^6$ eV for electrons and 5 x 10^9 eV for protons. The maximum energy of the charged particles can be obtained from equalling the dominant cooling rate to the acceleration rate. For an arbitrary set of values, Fig 2.5 shows the

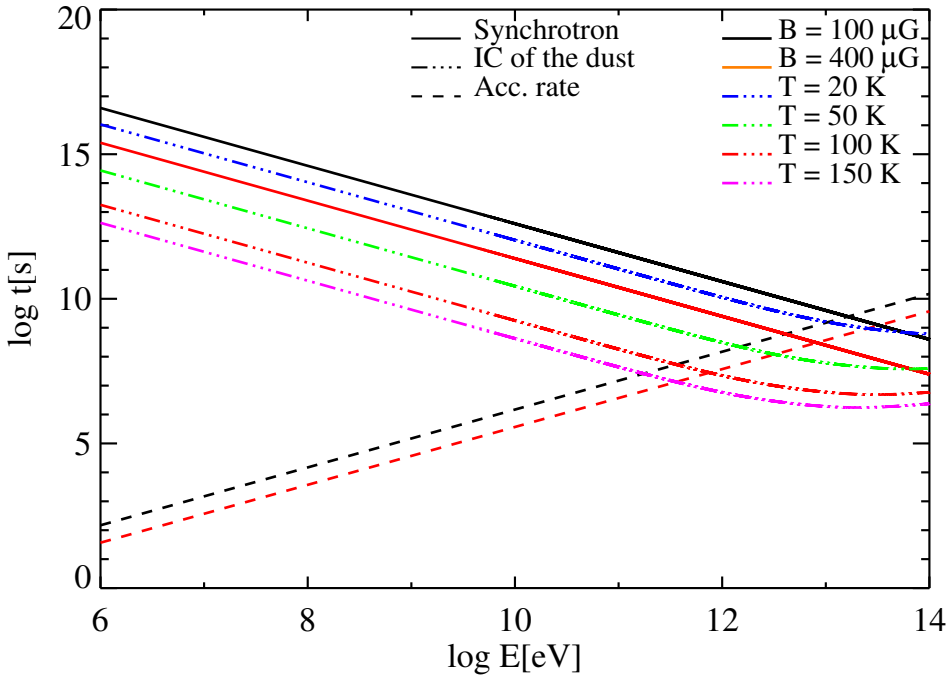

Figure 2.5: Variation of the maximum energy for different values of the magnetic field and the dust temperature.

dependency of the maximum energy reached by electrons on the dominant cooling process in the presence of a magnetic field and when scatter a photon field at given temperature. Straight lines represent the synchrotron cooling time rates, the dotted-dashed lines the IC of the dust photons and the dashed lines the acceleration rates. The synchrotron cooling rate decreases when the magnetic field increases; the same happens with the acceleration rates. On the other hand, the IC cooling time

losses are shorter for higher dust temperatures. Warmer dust temperatures favor the dominance of the IC losses of the dust photons, whilst high magnetic fields favor the synchrotron losses to be the most effective cooling process. Hence, the maximum energy can vary two orders of magnitude, depending on the dominant losses.

However, we see that both the IC and the synchrotron cooling rates can be very similar or have similar values at a wide range of energies. In a more general case, we may obtain the equivalent cooling time rate as

$$\frac{1}{t_{loss}} = \sum \frac{1}{t_i}, \tag{2.23}$$

where t_i are the cooling time rates of each of the nonthermal processes considered.

Finally, the probability of the charged particles to be convected away from the acceleration region by the stellar wind must be also be taken into account. The convection timescale is given by $t_{esc} \sim 4\Delta/V_w$ [Bell, 1978]. If the convection time is shorter than the cooling time rate of the most efficient nonthermal process, charged particles may not have time to cool completely. On the other hand, the diffusion* time rate is also very important and can be estimated as $t_{diff} = \Delta^2/2D_B$ [del Valle & Romero, 2012], where D_B is the diffusion coefficient in the Bohm limit. We verify that it is always much larger than the other time scales (than the convection time at all energies), and therefore we will neglect the diffusion term (see Sec. 2.3, Eq. 2.24)

Fig. 2.6 shows the leptonic cooling time rates for the bow shock formed by the star AE Aurigae (see Sec. 3.3.1). The maximum energy reached by the electrons is $\sim 3 \times 10^{11}$ eV, and the most effective cooling process is the IC of the dust photons. Notice that the escape time is shorter than the cooling time rate of the lowest energy electrons, and hence they are expected to scape from the acceleration region before they have time to cool completely. The synchrotron losses, the relativistic Bremstrahlung and the IC of the cosmic Microwave Background (CMB) are the less efficient cooling processes in this bow shock, compared to the IC of the dust and the starlight photons. On the other hand, in Fig. 2.7 we show the hadronic time rate for the same star. The proton-proton inelastic collisions time rate is much greater for all energies than the time needed for the particles to escape from the acceleration region. Hence, protons are more likely to escape before losing a significant fraction of its energy. This does not mean that protons will not produce any emission, but that the proton energy distribution will be given by the injection function (Eq. 2.3), as we will see in the next section.

2.3 Particle energy distribution

To compute the emission produced by the cooling processes mentioned above, the particle distribution of electrons $N(E)$ (and protons) is needed. The Fermi first

*Movement of the particles from a region of high concentration to a region of low concentration. In this case, electrons can scape from the acceleration region, where the electron concentration is high, to regions outside the shock where the electron density is smaller.

order mechanism responsible of the charge particle acceleration also produces a random scattering of the particles due to the magnetic inhomogeneities in the acceleration region, and hence these particles can diffuse from their sources trough the interstellar medium. The spectrum of the particles can be study from the diffusion-loss equation for high-energy particles, which describes the energy spectrum in the presence of energy losses and with a continuous supply of new charged particles (those accelerated by the Fermi first order mechanism) and their diffusion from their sources [Ginzburg & Syrovatskii, 1964]:

$$\frac{\mathrm{d}N(E)}{\mathrm{d}t} = D\nabla^2 N(E) + \frac{\partial}{\partial E}\Big[-\frac{\mathrm{d}E}{\mathrm{d}t}N(E)\Big] - \frac{N(E)}{t_{esc}} + Q(E). \tag{2.24}$$

In Sec. 2.1 we explained that $Q(E) = Q_0 E^{-\alpha}$ is a power-law distribution of the injected particles in the acceleration region given by the Fermi first order mechanism. For our purposes we consider that the energy distribution reaches a steady state, $\mathrm{d}N(E)/\mathrm{d}t = 0$, and neglecting diffusion the spatial dependency also disappears ($D\nabla^2 N(E) = 0$) and simplifies the problem to

$$\frac{\partial}{\partial E}\Big[\frac{\mathrm{d}E}{\mathrm{d}t}\Big|_{loss} N(E)\Big] + \frac{N(E)}{t_{\mathrm{esc}}} = Q(E). \tag{2.25}$$

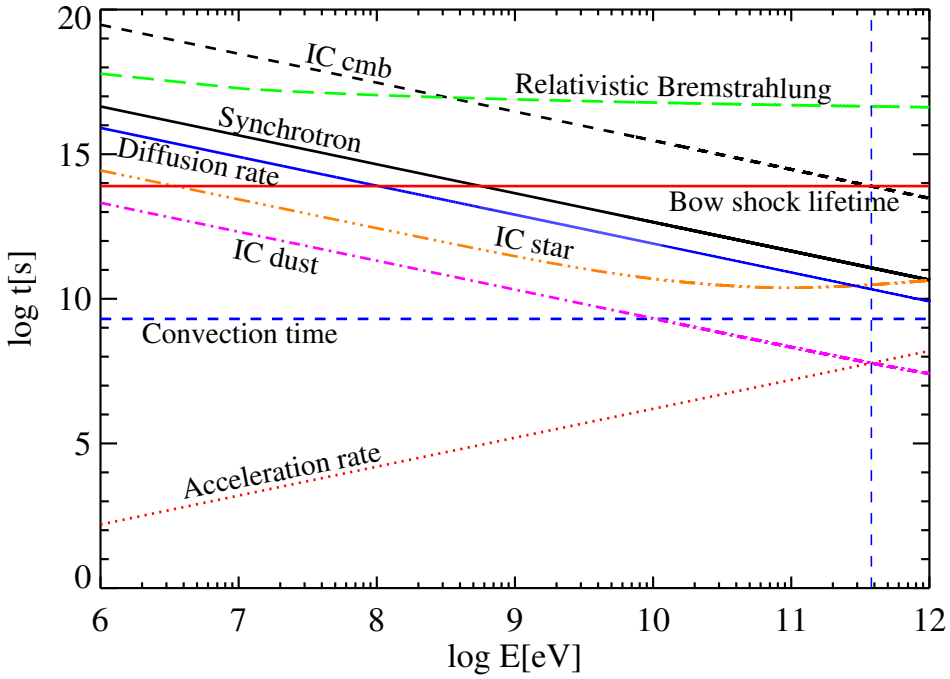

Figure 2.6: Leptonic cooling time rates, acceleration rate, escape time, acceleration rate and bow shock lifetime for the parameters of the bow shock formed by AE Aurigae (see Sec. 3.3.1). The IC of the dust photons is the most effective cooling process, followed by the IC of the starlight photons and then by the synchrotron cooling time rate. The maximum energy is represented by the vertical dashed line.

The normalization constant Q_0 can be obtained from the energy available in the acceleration region that goes into electrons energy, L_e, by

$$L_e = V \int_{E_{\rm min}}^{E_{\rm max}} Q(E) E {\rm d}E = V Q_0 \int_{E_{\rm min}}^{E_{\rm max}} E^{1-\alpha} {\rm d}E. \tag{2.26}$$

The electron injection index, α, defines the solution of the previous equations:

$$L_e = V Q_0 \frac{1}{2-\alpha} \Big(E_{\rm max}^{2-\alpha} - E_{\rm min}^{2-\alpha} \Big), \text{ if } \alpha \neq 2 \tag{2.27}$$

$$L_e = V Q_0 ln \Big(\frac{E_{\rm max}}{E_{\rm min}} \Big), \text{ if } \alpha = 2 \tag{2.28}$$

In accordance with the assumed energy dependencies for primary electrons [e.g. Lin et al., 2010; Protheroe & Stanev, 1999; Rieger et al., 2007], the values of α we use in our simulations are ≥ 2. Finally, the exact solution of Eq. 2.25 is also a power-law of the form:

$$N(E) = \frac{t_{\rm loss}}{E} \int_{E}^{E_{\rm max}} {\rm d}E' Q(E') \exp\Big(- \frac{t_{\rm loss}}{t_{\rm esc}} \Big). \tag{2.29}$$

This last expression has been derived considering electrons of any energy have time to cool completely before they are convected away. Nevertheless, bow shocks

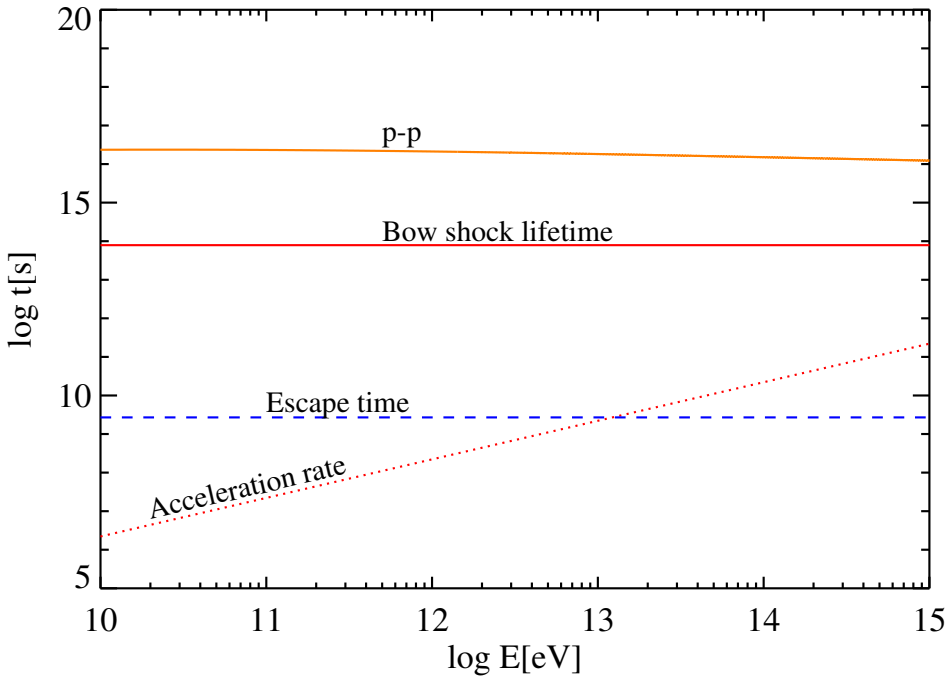

Figure 2.7: Proton-proton inelastic collision time rate, escape time and bow shock lifetime for the parameters of the bow shock formed by AE Aurigae (see Sec. 3.3.1). Protons are more likely to escape from the acceleration region rather than cool by p-p inelastic collisions. Also, the bow shock lifetime is shorter than the time needed by the protons to cool completely by this process.

formed by runaway stars also have lifetimes that can be shorter than the time electrons of different energies need to cool completely by the cooling processes described in the previous section. In Fig. 2.6 the IC is shown as the dominant cooling process. However only electrons with energies over 10 GeV are able to cool completely. In this case, the electron energy distribution of the highest energy electrons will follow equation 2.29, whilst the electron energy distribution of those electrons with energies under 10 GeV will be represented by the injection function. Hence, there is a change in the slope in the electron energy distribution, which is one power of E flatter in the range of those electrons whose cooling time rate is greater than the bow shock life time, with a smooth transition between the two regimes given by Longair [2011]:

$$N'(E) = N(E)(1 - (1 - t_{\rm life}/t_{\rm loss})^{\alpha-1}). \tag{2.30}$$

The consideration of the convection time also produces a change in the slope by a power of E when the time needed by the electrons to cool completely is greater than the convection time, but its effect in considered by the exponential term $\exp(-t_{\rm loss}/t_{\rm esc})$. In Fig 2.8 is represented the electron energy distribution for the bow shock formed by AE Aurigae. In this case, the change in the slope is produced by the convection and not by the bow shock lifetime (see Fig 2.6). For $\alpha = 2$, the electron distribution can be parametrized by two exponential functions, $N(E) \propto E^{-2}$ (corresponding to the range of electrons that did not cool completely because the convection time is shorter than the IC cooling time rate) and $N(E) \propto E^{-3}$ (for those electrons that have time to cool completely, see Eq. 2.29) plus a cutoff at those energies close to the maximum energy.

The proton energy distribution can not be obtained from Eq. 2.29 since in Fig. 2.7 is clear that the time needed for the protons to cool completely through proton-proton inelastic collisions is much larger than the convection time and the bow shock lifetime. In this case the energy distribution is simply the injection function with an exponential cutoff. The cutoff energy, $E_{0,p}$ would correspond to the energy where the acceleration rate and the escape time or the age of the source are equal. A general expression of the distribution would be [Kelner et al., 2006],

$$N(E)_p = Q(E)_p = Q_{0,p}E_p^{-\alpha}\exp{-(E_p/E_{0,p})^{\beta}}, \tag{2.31}$$

where β is typically 1 or 2 [e.g., Miceli et al., 2013].

2.4 Spectral synthesis

2.4.1 Synchrotron emission

Following the derivations by Rybicki & Lightman [1979], the total emitted power per unit of energy is

$$P(\varepsilon_1) = \frac{\sqrt{3}e^3 B sin\alpha}{hmc^2} F(x), \tag{2.32}$$

where ε_1 is the energy of the emitted photons and

$$F(x) = x \int_x^{\infty} K_{5/3}(\xi) d\xi. \tag{2.33}$$

$K_{5/3}$ is the modified Bessel function of order 5/3. The expression $F(x)$ can be approximated by $F(x) \sim 1.85x^{1/3}\exp(-x)$, where now x is $x = \varepsilon_1/E_c$ and E_c is the characteristic energy given by

$$E_c = \frac{3}{4\pi} \frac{ehB}{mc} \Big(\frac{E}{mc^2}\Big)^2. \tag{2.34}$$

Assuming an isotropic distribution of pitch angles, $B\,\sin\alpha$ can be written as $B\sqrt{2/3}$ [Peri , 2010]. Finally, the total luminosity at an energy ε_1 produced by an electron distribution $N(E)$ is

$$L(\varepsilon_1) = 1.85 A \varepsilon_1 V \frac{\sqrt{2}\, e^3 B}{hmc^2} \int_{E_{\min}}^{E_{\max}} N(E) \Big(\frac{\varepsilon_1}{E_c}\Big)^{1/3} \exp\Big(-\frac{\varepsilon_1}{E_c}\Big) \mathrm{d}E. \tag{2.35}$$

Here A is the absorption coefficient. The specific intensity of radiation from a source in thermodynamic equilibrium cannot exceed a limit set by the temperature of the source, so at this point emission and absorption are balanced along the line

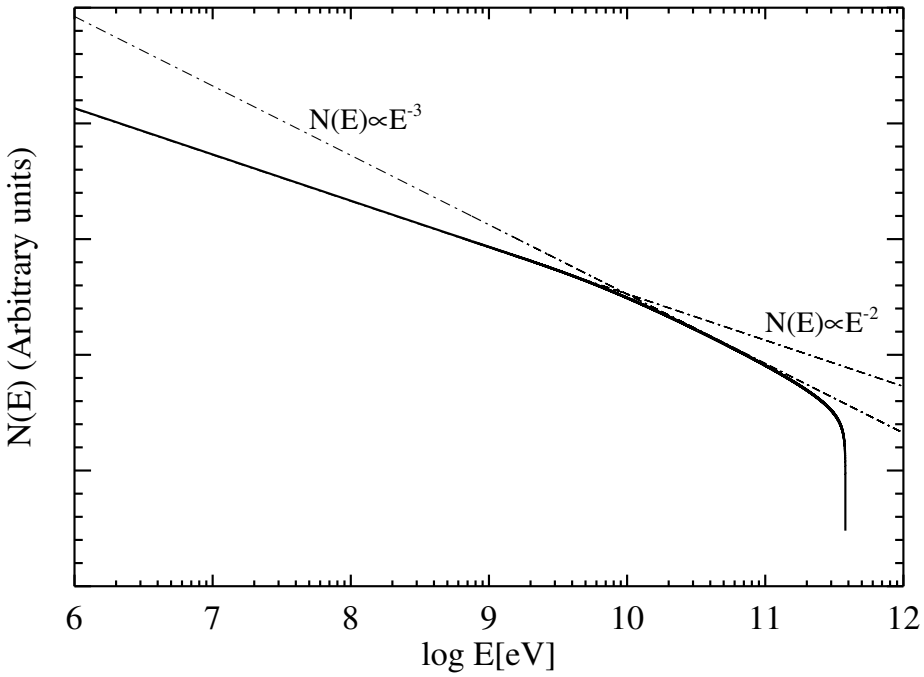

Figure 2.8: Electron energy distribution in the acceleration region of the bow shock formed by the runaway star AE Aurigae. The solid line represents the electron distribution computed by using Eq. 2.29 and 2.30. Dashed lines represent the paremeterization of the solid curve.

of sight. This must apply to synchrotron radiation, although in this case the source temperature must be related to the kinetic energy of the radiating electrons, which are not necessarily in thermal equilibrium with their surrondings. The emission must then be balanced by an inverse process of absorption, which is known as synchrotron self-absorption [e.g., Burke & Graham-Smith, 2014]. The absorption coefficient A is then represented by [del Valle & Romero, 2012]

$$A = \frac{1 - exp(-\chi_{\varepsilon_1} l)}{\chi_{\varepsilon_1} l}, \tag{2.36}$$

where l is the thickness of the region (Δ in Fig. 3.1). The distribution obtained from Eq 2.29. can be substituted by a power-law energy distribution of the form $N(E) = \kappa E^{-p}$ (notice the difference between the injected electron index, α, and the new electron distribution index, p), as seen in Fig. 2.8. The synchrotron self-absorption coefficient, χ_{ε_1}, for each frequency of the emitted photons [Rybicki & Lightman, 1979] is,

$$\chi_{\varepsilon_1} = \frac{\sqrt{3} e^3}{8\pi m_e} \kappa B^{(p+2)/2} \left(\frac{3e}{2\pi m_e^3 c^5} \right)^{p/2} b(p) (h/\varepsilon_1)^{(p+4)/2}, \tag{2.37}$$

where

$$b(p) = \frac{\sqrt{\pi}}{8} \frac{\Gamma(\frac{3p+22}{12}) \Gamma(\frac{3p+2}{12}) \Gamma(\frac{p+6}{4})}{\Gamma(\frac{p+8}{4})}. \tag{2.38}$$

To test the influence of the synchrotron self-absorption, we compute its effect for two arbitrary values of the magnetic field. In figure 2.8 we see that the electron distribution can be represented by two indexes, $p = 2$ and $p = 3$. These values of p lead to $\chi_E = 8.15 \times 10^{-63} \kappa B^2 / E^3$ cm^{-1} and $\chi_E = 2.15 \times 10^{-66} \kappa B^{2.5} / E^{3.5}$ cm^{-1}, respectively. The synchrotron self-absorption only affects the lowest energy emitted photons, as shown in Fig. 2.9. It is clear than even for high magnetic fields, only the lowest energy emitted synchrotron photons are affected by the synchrotron self-absorption. Hence, we have test that the its effect can be neglected in our study.

Let us assume that the synchrotron cooling is the most effective cooling process in a given source and that the source lifetime and size (and so the convection time) are larger than the synchrotron cooling time, and hence particles can cool completely. In this situation, the magnetic field affects both the synchrotron cooling rate and the acceleration rate, and since the maximum energy will be given by the point where both rate are equal, a change in the magnetic field changes the maximum energy achieve by the electrons, which is in fact the integration limit in Eqs. 2.29 and 2.35). In Fig. 2.10 is represented how the magnetic field and the injection index affect the shape of the synchrotron spectrum. As the magnetic field changes, the synchrotron cutoff also changes; the electron injection index also changes the synchrotron shape: higher indexes produce a flattening before the cutoff region. This is, furthermore, of the utmost importance when the cutoff region corresponds with the X-ray band, because small variations in the parameters can produce great variations in the shape.

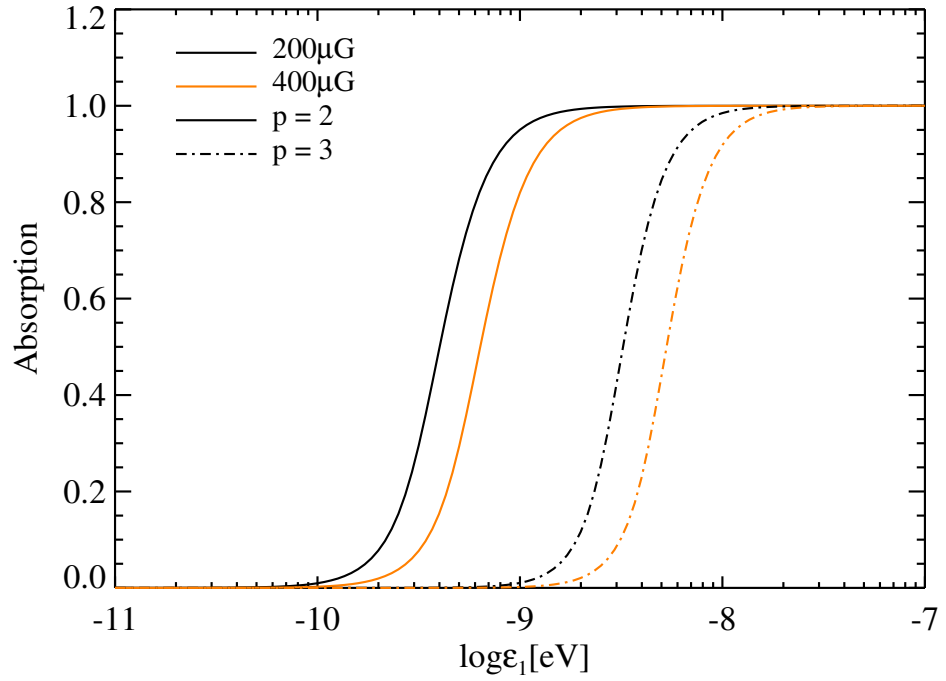

Figure 2.9: Synchrotron self-absorption as a function of the magnetic field and the electron energy distribution power-law index.

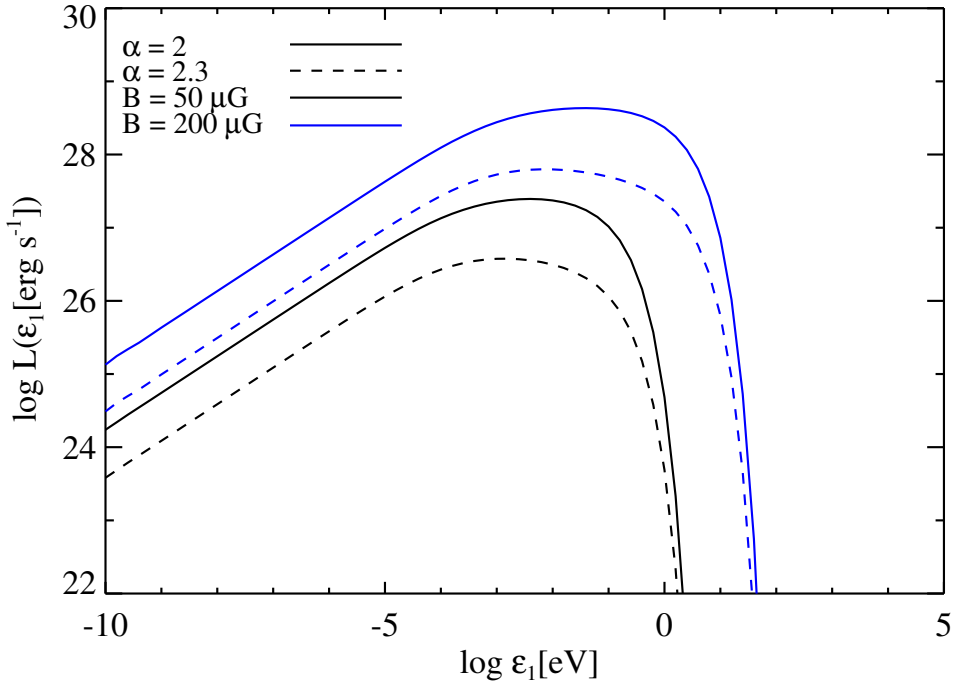

Figure 2.10: Synchrotron shape and cutoff variations as a function of the electron injection index and the magnetic field. The simulations were done for an arbitrary set of parameters of a bow shock formed by a runaway star. In this case, the synchrotron emission is responsible of the soft X-rays emission.

2.4.2 IC emission

IC emission is call to be a relevant process to explain the origin of the most energetic photons generated in strong shocks, as we will see along this thesis. The IC luminosity can be computed by

$$L(\varepsilon_1) = \varepsilon_1^2 V \int_{E_{\min}}^{E_{\max}} N(E) \int_{\varepsilon_{\min}}^{\varepsilon_{\max}} P_{IC}(E, \varepsilon_1, \varepsilon) \mathrm{d}\varepsilon \mathrm{d}E, \tag{2.39}$$

where the spectrum of scattered photons, $P_{IC}(E, \varepsilon_1, \varepsilon)$, is

$$P_{IC}(E, \varepsilon_1, \varepsilon) = \frac{3\sigma_T c (mc^2)^2}{4E^2} \frac{n_{ph}(\varepsilon)}{\varepsilon} f(q), \tag{2.40}$$

with $f(q)$ given by

$$f(q) = 2q\ln q + 1 + q - 2q^2 + \frac{1}{2}\frac{(bq)^2}{a + bq}(1 - q), \tag{2.41}$$

and $b = 4\varepsilon\gamma/mc^2$, $q = \varepsilon/[b(E - \varepsilon_1)]$. Assuming that the fraction of energy turned into relativistic particles (see Sec. 3.2) is the same for electrons and protons, then $a = 1$.

IC can be responsible of the X-ray emission, as is the case of the bow shocks formed by runaway stars or of the gamma emission in the GeV and TeV band, for example, in the supernova remnants. In most cases, the IC of the stellar photons is negligible. In Fig. 2.11 we plot the variation of the IC luminosity with the magnetic field and the injection index.

2.4.3 Relativistic Bremstrahlung emission

For the relativistic Bremsstrahlung, the luminosity can be calculated as

$$L(\varepsilon_1) = \varepsilon_1 V n \frac{c}{4\pi} \int_{E_{\min}}^{E_{\max}} \sigma_B(E, \varepsilon_1) N(E) \mathrm{d}E, \tag{2.42}$$

where

$$\sigma_B(E, \varepsilon_1) = 4\alpha r_e^2 \phi(E, \varepsilon_1), \tag{2.43}$$

and

$$\phi(E, \varepsilon_1) = \left\{1 + \left(1 - \frac{\varepsilon_1}{E}\right)^2\right\}\left\{\ln\frac{2E(E - \varepsilon_1)}{mc^2\varepsilon_1} - \frac{1}{2}\right\} - \frac{2}{3}\left(1 - \frac{\varepsilon_1}{E}\right). \tag{2.44}$$

This emission is associated to the acceleration of electrons in the electrostatic field of the nucleus, and corresponds to transitions between unbound states of the electron. However, compared the IC emission, the emission produced by this process is much lower, although it also can reach the GeV band.

2.4.4 π^0 decay emission

The time scale of the protons to cool completely is much larger that the convection time from the acceleration region (see Fig 2.7), and hence the proton energy distribution is the injection function of protons. However, as explained in Sec. 2.3, in this case we have to add an exponential cutoff with $\beta = 2$ in Eq. 2.31. Again, the normalization constant Q_{0p} can be obtained from

$$L_p = V \int_{E_{pmin}}^{E_{pmax}} Q(E_p) E_p \mathrm{d}E. \tag{2.45}$$

To derive the emission from the π^0 decay we follow Kelner et al. [2006] derivations. For $E_p > 0.1$ TeV, the luminosity is given by

$$L(\varepsilon_1) = \varepsilon_1^2 c n_H V \int_0^1 \sigma_{inel}(E_p) Q(E_p) F(x, E_p) \frac{dx}{x}, \tag{2.46}$$

where n_H is the shocked medium density, $x = \varepsilon_1/E_p$, $L = ln(E_p/1TeV)$, σ_{inel} was given in Sec. 2.2.4 and $F(x, E_p)$ is

$$F(x, E_p) = C \frac{\ln(x)}{x} \left(\frac{1 - x^\beta}{1 + k x^\beta (1 - x^\beta)} \right) \left[\frac{1}{\ln(x)} - \frac{4\beta x^\beta}{1 - x^\beta} - \frac{4k\beta x^\beta (1 - 2x^\beta)}{1 + k x^\beta (1 - x^\beta)} \right]. \tag{2.47}$$

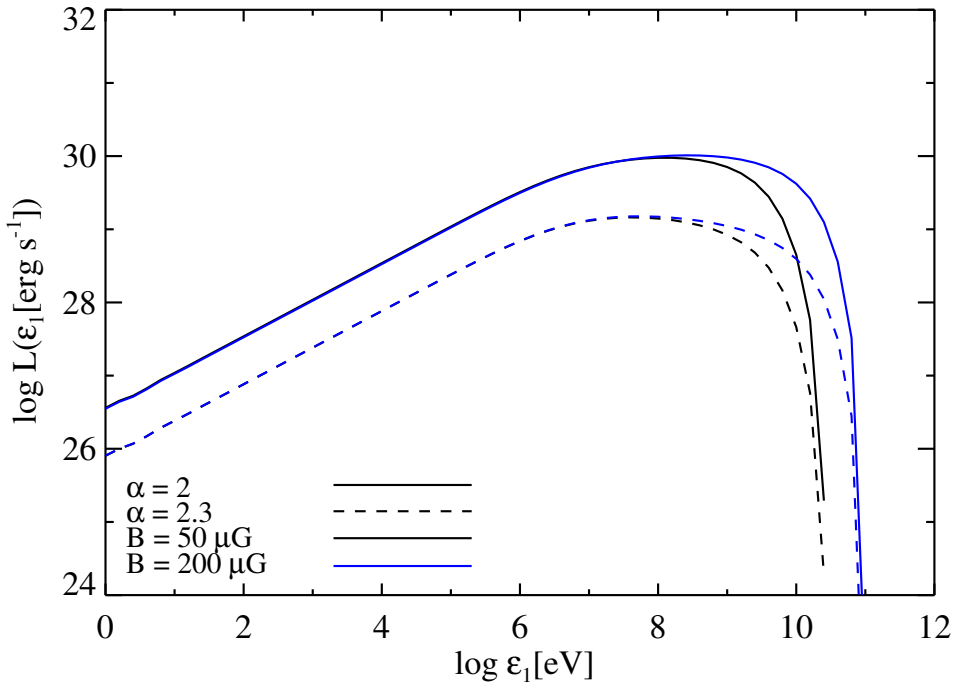

Figure 2.11: An example of the IC shape and cutoff variations as a function of the electron injection index and the magnetic field. Greater values of α flatten the peak of the IC spectrum, while the magnetic file values mostly affect the cutoff energies, given the influence of the acceleration energy on the maximum energy, and the magnetic field on it.

$F(x, E_p)$ is the number of photons in the interval $(x, x + dx)$ per collision, and the terms C, β and k are

$$C = 1.30 + 0.14L + 0.011L^2, \tag{2.48}$$

$$\beta = \frac{1}{1.79 + 0.11L + 0.008L^2}, \tag{2.49}$$

$$k = \frac{1}{0.801 + 0.049L + 0.014L^2}. \tag{2.50}$$

For $E_p < 0.1$ TeV the emitted spectrum is

$$L(\varepsilon_1) = 12.9\varepsilon_1^2 c n_H V \int_{E_{min}}^{\infty} \frac{\sigma_{inel}(E_p)Q(E_p)}{\sqrt{E_\pi^2 - m_\pi^2}}. \tag{2.51}$$

Here, $E_{\rm min} = \varepsilon_1 + m_\pi^2/4\varepsilon_1$ (m_π =135 MeV/c^2) and $E_\pi = 0.17(E_p - m_p)$ (m_p = 938 MeV/c^2).

2.5 Thermal radiation

The emission produced by some objects (and in particular those that we aim to study in the following chapters) could have the contribution of both nonthermal and thermal components. The latter component may take the form of either thermal bremsstrahlung from an optically thin gas or of a blackbody radiation from an optically thick object. The major emitting processes from a hot gas are the thermal Bremsstrahlung, bound-bound emission and free-bound emission. The last two processes involve the presence of atoms with at least some of their electrons remaining in bound orbits around the nucleus. Gaseous plasmas with a normal astrophysical abundance of elements (mostly hydrogen and helium) are almost completely ionized at high temperatures [$\sim 10^7$ K; e.g. Kippenhahn & Weigert, 1990]. Therefore, the major emission process considered here is thermal Bremsstrahlung of the plasma.

The spectral emissivity of the gas is [Adams, 1980; Longair, 2011]

$$\kappa_\nu = \frac{1}{3\sqrt{6}\pi^{3/2}} \frac{Z^2 e^6}{\varepsilon_0^3 c^3 m_e^2} n_e n_i \exp\Big(-\frac{h\nu}{kT}\Big) g(\nu, T) \Big(\frac{m_e}{kT}\Big)^{1/2}, \tag{2.52}$$

where Z=1, n_e is the electron density in units of cm^{-3}, n_i the nuclei density, T is the shocked plasma temperature and $g(\nu, T)$ the Gaunt factor, a slowly varying function of ν for which detailed calculations show that its frequency averaged value, $\bar{g}$, ranges from 1.1 to 1.5 along the whole spectrum, and thus, $\bar{g} = 1.2$ is a good approximation for our purposes. Considering a plasma mostly formed by hydrogen, the electron density and the ion density are the same, $n_e = n_i$, and so the density of cold electrons is similar to the medium density. However, not all those cold electrons are heated by the shock. In particular, for the case of bow shocks formed by runaway stars, assuming that all the shock region can emit thermal X-rays, only

about the $\sim$ 3% of the cold electrons are heated, [Terada et al., 2012], and thus $n_{th} = 0.03 n_H$. Then, $n_e n_i$ in Eq. 2.53 must be replaced by n_{th}^2.

On the other hand, the plasma temperature, T, can be obtained from

$$kT = \frac{\mu m_H}{3} v_w^2 = 3.4 \times 10^{-9} v_w^2 \text{ K}, \tag{2.53}$$

where μ is the mean ratio of number of electrons and nucleons ($\mu = 0.615$), $m_H = 2.3 \times 10^{-24}$ g and v_w is the wind velocity. Taking into account that $\nu = \varepsilon_1/h$, the emissivity is simplified to

$$\kappa_{\varepsilon_1} = 8.16 \times 10^{-38} T^{-1/2} n_{th}^2 \exp\Big(- \frac{\varepsilon_1}{kT} \Big).$$

Finally, the luminosity of the thermal Bremstrahlung is given by

$$L = \varepsilon_1 \kappa_{\varepsilon_1} V/h. \tag{2.54}$$

Whilst the relativistic Bremstrahlung is expected to play an important role in the X-ray band, the thermal emission of the heated dust is, on the contrary, expected to produce the observed IR emission detected around many bow shocks [Peri et al., 2012]. If we consider the heated dust as a black body at a temperature T_B, the luminosity will be given by

$$L(\varepsilon_1) = \frac{2\varepsilon_1^4}{c^2 h^3} \frac{1}{\exp(\varepsilon_1/kT_B) - 1}, \tag{2.55}$$

where now T_B is given by Eq. 2.15.

Chapter 3

Bow shocks from runaway stars

3.1 The origin of the runaway stars

O and B type stars, with masses over $10 M_{\odot}$ and temperatures between 15.000K and 50.000K, are the most massive and luminous stars. In their short life ($\leq$20 Myr) these stars lose mass at a rate of $\dot{M} \approx 10^{-7} - 10^{-5} M_{\odot}$ yr^{-1}, and their stellar winds, with velocities of the order of $v_{\infty} \approx 1.000 - 3.000$ km s^{-1}, transfer great amounts of mechanical energy to the circumstellar medium.

Runaway stars are stellar objects that were expelled from their place of origin by dynamical processes. They show high spatial velocities (corrected from solar movement and the differential rotation of the galaxy) that exceed the typical velocity of these objects on the galaxy and that can reach 200 km s^{-1}. Taking as a definition a velocity over 40 km s^{-1}, Blaauw [1961] discovered the first 19 runaways stars. Currently, a runaway star is that with a velocity over 30 km s^{-1}, to differentiate it from those O and B stars with typical velocities and dispersions of about 10 km s^{-1}. Later, Gies & Bolton [1986] and Gies [1987] expanded the catalog of runaway stars; Moffat et al. [1998, 1999], trough a study based on proper motions measured by *Hipparcos*, also contributed to the classification of more O and B stars as runaway stars. Currently, the most recent catalogs of O and B runaway stars are those of Maíz-Apellániz et al. [2004] and Tetzlaff et al. [2010].

Present theories about the formation of massive stars highlight the importance of dense clusters in which the majority of these stars, if not all, are formed. The dynamical interaction in the center of the star forming regions can lead to the formation of binary systems, to ejections, mass segregations and mergers of stars. As a consequence of these interactions, a high rate of runaway stars has been detected in dense clusters. Hoogerwerf et al. [2000] estimated that around $10\% - 30\%$ of the O stars and the $5\% - 10\%$ of the B stars are of this type. Furthermore, as these objects are relatively young, they have only travelled a few or a few hundred of parsecs, and hence it is possible to identify the parental cloud or the stellar group the stars come from.

Two mechanisms are proposed to explain the production of runaway stars: the *binary-supernova scenario* [Blaauw, 1961; Zwicky, 1957] and the *dynamical ejection scenario* [Gies & Bolton, 1986; Poveda et al., 1967]. In the former one, a supernova

explosion impels to its massive and close binary companion. After the explosion, the binary star is dissociated and the secondary star starts to move throughout the space at a velocity comparable to the orbital velocity previous to the explosion, of the order of $30 - 50$ km s^{-1}. This scenario is favored by the high rate of binaries among the massive systems. A possible example of this case would be ζ Oph: after studying its motion, Hoogerwerf et al. [2000] discovered that its trajectory intersected that of the close pulsar PSR J1932+1059 one Myr ago, in the stellar group of Upper Scorpius; the neutron star would be the remnant of a supernova that took place in the binary system to which ζ Oph also belonged, in such a way that when the supernova exploded, both objects were expelled.

In the second scenario, the runaway star reaches its high velocity after dynamical interactions with other or others stars. The most efficient encounter is that produced between two binary and massive systems that, in many cases, results in the ejection of two runaway stars at velocities over 200 km s^{-1} and one eccentric binary. In this scenario the most common result is the exchange between the most massive binary components, that formed a new eccentric binary or merged, and the ejection of the low mass companions. The ejection velocity of the later components can be as high as the escape velocity of the surface of the most massive star, about 1.000 km s^{-1}. On the other hand, the backward velocity of the new binary formed by the two massive stars can exceed the escape velocity of the potential well of the parental cloud and so also becomes in a runaway object. The high stellar density in the parental cloud favors the interactions and the ejections and hence the reproduction of the *dynamical ejection scenario*. An example would be the system formed by AE Aur, μ Col and the eccentric binary ι Ori [Gualandris et al., 2004; Hoogerwerf et al., 2000]: their trajectories would have crossed ~ 2.5 Myr ago in the Trapezium cluster, confirming that their present velocities are the result of a binary-binary encounter.

Which of the two mechanisms or scenarios dominates in the creation of runaway stars has been widely debated in the past. The modest precision and the lack of data did not always allow to precisely distinguish between the two mechanisms, and sometimes both scenarios are consistent with the statistical properties of the set of runaway stars. Nowadays, the availability of *Hipparcos* data and its good precision for close stars, as well as the pulsar astrometry of the VLBI, permit tracing trace the past trajectories of runaway stars to study their ejection mechanism. Those studies dedicated to ζ Oph and the stars AE Aur, μ Col and ι Ori have succeed in explaining the origin of other 18 runaway stars and two pulsars. Out of them, one third would have acquisted their velocity after dynamical interactions and the other two thirds after supernova outbreaks in binary systems. In general, a past encounter of the proper motions between an individual star and a pulsar would confirm the *binary-supernova scenario*, whilst a trajectory encounter between two or more runaway stars would certificate their origin from a *dynamical ejection scenario*.

3.2 Bow shock formation and main parameters

When a runaway star moves through a dense region of the interstellar medium, for example, through a molecular cloud, the pressure balance between the stellar wind and the interstellar medium results in an axisymmetric bow shock in the direction of the movements of the star. In particular, the strong winds of the O, B and Wolf-Rayet stars are able to form thin and dense layers ahead of the stars and in the same direction of the proper motion when the star interacts with the circumstellar medium and moves supersonically through it.

When the supersonic stellar wind of a runaway star interacts with its surroundings, a resulting system of two shocks can be formed: a bow shock, which is the heading front shock propagating in the same direction as the stellar wind at a velocity similar to the stellar speed, and the reverse shock, moving opposite to the stellar wind and at its same velocity. Since the stellar wind can be considered a continuous power source, both shocks reach a steady state where the reverse shock is fast an adiabatic and the forward shock is radiative and slower [see van Buren, 1993]. The density of the ISM around the shock, ρ_{ISM}, is assumed to be constant, while the density of the stellar wind, ρ_w, decreases with growing distance from the star. The interaction of both media results in a bow shock where $\rho_{ISM}V_\star^2 \sim \rho_w V_w^2$, at a distance from the central star defined by the so called standoff radius, R_0, expressed by [Wilkin, 1996]:

$$R_0 = \sqrt{\frac{\dot{M}V_w}{4\pi\rho_{ISM}V_\star^2}}. \tag{3.1}$$

Here, $\dot{M}$ is the mass-loss rate, which represents the mass a star losses per unit of time, $\dot{M}= dM/dt$, and although represent the losses, is used as a positive value, expressed in solar masses per year ; V_w the wind terminal velocity, which is the velocity of the steer wind at high distances from the star (ranges from about 10 km/s in supergiant cool stars up to 3000 km/s in very hot and luminous stars); ρ_{ISM} ($\rho_a = n_H\mu$, where n_H is the ambient column density in cm^{-3} and $\mu = 2.3 \times 10^{-24}$ g the mass per H atom) is the ambient density and $V_\star$ is the stellar velocity.

Electrons and protons are efficiently accelerated in the fast adiabatic shock through diffusive shock acceleration (the Fermi first order mechanism, see Sec. 2.1): the magnetic field forces the charge particles to move continuously upstream-downstream the shock wave [Drury, 1983], and the shock wave typically have some magnetic inhomogeneities, so when particles encounter those inhomogeneities they can be reflected back through the shock at an increased velocity. The chain of reflections is what accelerates the particles up to very high energies [e.g. Bell, 1978; Longair, 2011]. The forward shock is also able to accelerate particles, but it is slower than the reverse shock and suffers from radiative losses, what makes it less efficient in accelerating electrons than the reverse shock.

The overall number of accelerated particles depends on the size of the acceleration region, which has not been studied in much detail in the literature, though it is a major parameter of the shock. The thermal IR shock is much larger than the acceleration region, which is assumed to be a surface near the bow shock apex of

width Δ, where the shock is nearly flat (see Fig. 3.1). Hence, if we express Δ in terms of the standoff radius, $\Delta = \delta R_0$, the larger is R_0, the smaller is δ. The total volume of this region can be obtained geometrically as

$$V = \frac{\pi \Delta^2}{3}(3R_0 - \Delta). \tag{3.2}$$

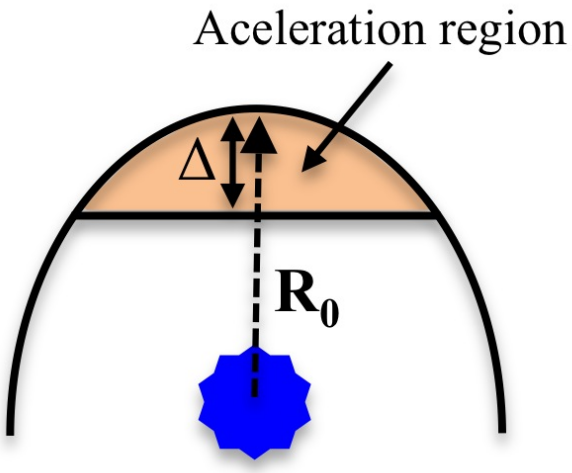

Figure 3.1: Shock front in the reference frame in which it is at rest. R_0 is the standoff radius and Δ is the width of the bow shock.

To estimate the value of the magnetic field that forces the charged particles to travel along the shock wave, we assume that the magnetic energy density is in subequipartition with respect to the kinetic energy by a factor χ, i.e., $u_B = \chi u_E$, where u_B is the magnetic energy density, $u_B = B^2/8\pi$, and B is the magnetic field. The kinetic energy is the energy released by the stellar wind per second, $L_T \sim \frac{1}{2}\dot{M}V_w^2$ (L_T is given in units of erg/s, i.e, in power units). The time a thin layer of plasma powered by the stellar wind needs to reach the bow shock region, at a distance R_0, is R_0/V_w and hence the total kinetic energy in a sphere of radius R_0 is $L_T R_0/V_w$. Thus, the energy density is

$$u_E = \frac{3L_T}{4\pi V_w R_0^2}. \tag{3.3}$$

Finally the magnetic field is given by:

$$B = \frac{1}{R_0}\sqrt{\frac{6\chi L_T}{V_w}}. \tag{3.4}$$

The power available in the acceleration region is given by the volume ratio, i.e, $L = VL_T/V_{R_0}$, where V_{R_0} is the volume of a sphere of radius R_0 and V is the volume of the acceleration region defined by Eq. 3.2. A small fraction of the

kinetic energy available in the acceleration region, L, goes into relativistic particles [see del Valle & Romero, 2012, and references therein]; this fraction is denoted by q_{rel} (a free parameter of our model), and thus the total energy of the accelerated charged particles is $L_{rel} = q_{rel}L$. These relativistic particles can be either electrons or protons, so L_{rel} has both a leptonic and a hadronic components, $L_{rel} = L_p + L_e = L_p + aL_p$ where a is the ratio of relativistic protons to electrons. Here we always consider $a = 1$, and hence $L_e = 0.5q_{rel}L$, same energy for protons and electrons.

We must highlight that not all the runaway stars effectively form a bow shock. During a study of HII regions in the galaxy with 60 μm IRAS data, Van Buren & McCray [1988] found that 15 runaway stars could have formed a bow shock when traveling through the interstellar medium. Bow shocks formed by runaway stars produce thermal emission when the stellar radiation field heats the swept dust and hence the heated dust emits infrared radiation. Those IRAS images revealed bow shock shape structures, possibly consistent with shocks. Another 20 bow shocks were classified as so by van Buren et al. [1995] and Noriega-Crespo et al. [1997]. The axial symmetry of these structures and their alignment along the direction of the movement of the central star induced them to think that they could only be shocks. Later, Povich et al. [2008] published the discovery of another 6 bow shocks in the star forming regions M 17 and RCW 49 from the study of *Spitzer* GLIMPSE images. Also combining data from 2MASS, Spitzer, MASX and IRAS they obtained the spectral distribution of those bow shocks and their associated stars. Ten more candidates were found by Kobulnicky et al. [2010] by using mid infrared images from the *Spitzer Space Telescope Cygnus X Legacy Survey*. Also Gvaramadze et al. [2011] discovered 7 bow shocks associated to stars that are escaping from the young stellar cluster NGC 6357. More recently, Peri et al. [2012] proposed a list of new 28 bow shock candidates from the first released WISE data. They concluded that bow shocks are detected in the infrared around the 10% of the O and B runaway stars and that the bow shock formation frequency would not be particularly favored by the stellar mass or the age, although a deeper study is necessary.

The study in radio wavelengths can also help to understand the physical processes that produce the high-energy emission from the runaway stars. Electrons than previously have been accelerated can then cool by synchrotron processes and produce radio nonthermal emission. Benaglia et al. [2010] published the first possible detection of a radio bow shock from the source BD+43 3654. This source was first studied in IRAS/60 μm by Van Buren & McCray [1988], with a low spatial resolution. Higher resolution images images were obtained with *MSX*, in which the shock structure appeared well defined, showing a bow shock shape. NRAO-VLA images in the 1.42 and 4.86 GHz band showed a comma-shape structure consistent with the *MSX* result, what would correspond to the first nonthermal radio emission detected from a bow shock formed by a runaway star. More recently, López-Santiago et al. [2012] reported the first X-ray detection of a bow shock in X-rays, from the bow shock formed by the runaway star AE Aur (HIP 24575).

3.3 A nonthermal study of the bow shocks

In the previous chapter we developed the theoretical model that permits to synthesize the theoretical spectrum of a bow shock. However, several parameters of the star are needed and it is necessary to follow the steps listed below (see also Fig. 3.2, where is shown an IDL pseudocode):

- The terminal velocity of the wind and the mass loss rate are needed to compute the kinetic energy $L_T = \frac{1}{2}\dot{M}V_w^2$.
- The standoff radius is usually derived from the IR images [Peri et al., 2012] and hence it is no necessary to use Eq. 3.1. With the bow shock width and the standoff radius it is possible to calculate the volume of the acceleration region with Eq. 3.2. However, the width of the bow shock region is left as a free parameter since is not a measurable value. The only condition is that is much smaller than the infrared bow shock.
- With the two parameters determined previously, the standoff radius and the fraction of energy turned into relativistic particles, q_{rel}, it is possible to derive the total energy available in the acceleration region for protons and electrons. A standard fraction of $q_{rel} = 10\%$ is generally used [del Valle & Romero, 2012], though it can be left free in the range 5% to 20%.
- From Eq. 3.4 we now can compute the value of the magnetic field. However, as the magnetic energy is in subequipartition with respect to the kinetic energy density by a factor χ, this factor is also a free parameter with a maximum value of 1.
- The next step is to compute all the cooling time rates, the acceleration rate and the convection time:
  - From Eq. 2.7, the acceleration rate.
  - The escape time can be computed by $t_{esc} \sim 4\Delta/V_w$.
  - From 2.11 the synchrotron cooling rate.
  - For the IC of the dust photons cooling rate the temperature of the heated dust is also needed. From Eq. 2.15 this temperature can be computed from the luminosity of the star. Then, the cooling time rate can be computed by using Eqs. 2.14 to 2.19.
  - In the case of the IC of the starlight photons, the stellar radius and temperature are also needed, and finally the same equations as for the IC of the dust can be used.
  - The IC of the CMB can be computed as the IC of the dust photons but considering a temperature of 2.725 K, as the CMB emission can be assumed as a black body at that temperature.

  - To compute the Bremstrahlung cooling time rate the medium density and the velocity of the star are also parameters needed, and its values can be obtained from 2.20.

- Once the cooling time rates are calculated, its easy to compute the maximum energy (see Sec. 2.2.5) a parameter of the utmost importance since defines the integration limits of the electron energy distribution.

- From Eq. 2.27 or Eq. 2.28 the normalization constant can be calculated, but its value depends on the electron injection index, which is left as a free parameter in the simulations.

- There is one dominant cooling process, but all the cooling processes can cool electrons as well, and hence all the processes must be taken into account by computing the effective cooling time rate as explained in 2.23.

- Now the maximum energy of the electrons can be obtained, and hence the electron energy distribution can be computed from Eq. 2.29. Notice that we also have to include the flattening in the distribution slope for the low-energy electrons by using 2.30. This transition can be produced both by the convection time or by the lifetime of the shock, in particular, the shorter of them.

- The final step is to synthesize the luminosity spectrum.

  - Eq. 2.35 defines the synchrotron luminosity distribution.
  - For the IC of the dust, the starlight and the CMB photons, the luminosity distribution is given by Eq. 2.39.
  - The Bremsstrahlung luminosity can be obtained from 2.42.
  - As the proton-proton inelastic collisions cooling time rate is always greater than the escape time, the electron energy distribution is simply the injection function (Eq. 2.3), the luminosity can be computed from 2.46:
  - The thermal contribution of the dust is given by 2.55 and the thermal Bremstrahlung by 2.54.

The results presented in this Chapter were published in Pereira et al. [2016].

Free parameters of the model:

Shock width: δ
Fraction of the total energy turned into relativistic particles: q_{rel}.
Magnetic subequipartition factor: χ.
Electron (protons) injection index: α (α_p).

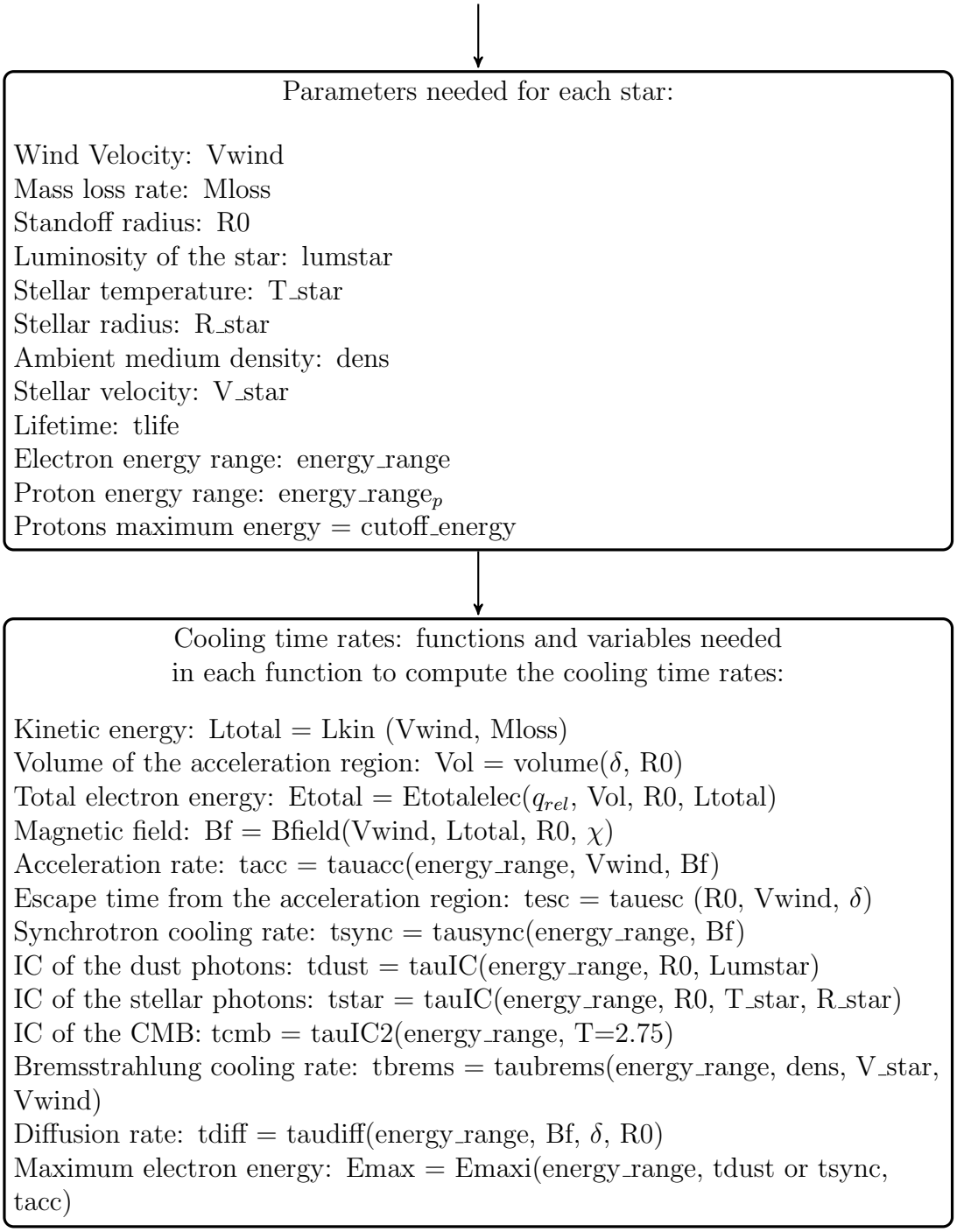
Parameters needed for each star:
Wind Velocity: Vwind
Mass loss rate: Mloss
Standoff radius: R0
Luminosity of the star: lumstar
Stellar temperature: T_star
Stellar radius: R_star
Ambient medium density: dens
Stellar velocity: V_star
Lifetime: tlife
Electron energy range: energy_range
Proton energy range: energy_range$_p$
Protons maximum energy = cutoff_energy
Cooling time rates: functions and variables needed
in each function to compute the cooling time rates:
Kinetic energy: Ltotal = Lkin (Vwind, Mloss)
Volume of the acceleration region: Vol = volume(δ, R0)
Total electron energy: Etotal = Etotalelec(q_{rel}, Vol, R0, Ltotal)
Magnetic field: Bf = Bfield(Vwind, Ltotal, R0, χ)
Acceleration rate: tacc = tauacc(energy_range, Vwind, Bf)
Escape time from the acceleration region: tesc = tauesc (R0, Vwind, δ)
Synchrotron cooling rate: tsync = tausync(energy_range, Bf)
IC of the dust photons: tdust = tauIC(energy_range, R0, Lumstar)
IC of the stellar photons: tstar = tauIC(energy_range, R0, T_star, R_star)
IC of the CMB: tcmb = tauIC2(energy_range, T=2.75)
Bremsstrahlung cooling rate: tbrems = taubrems(energy_range, dens, V_star, Vwind)
Diffusion rate: tdiff = taudiff(energy_range, Bf, δ, R0)
Maximum electron energy: Emax = Emaxi(energy_range, tdust or tsync, tacc)

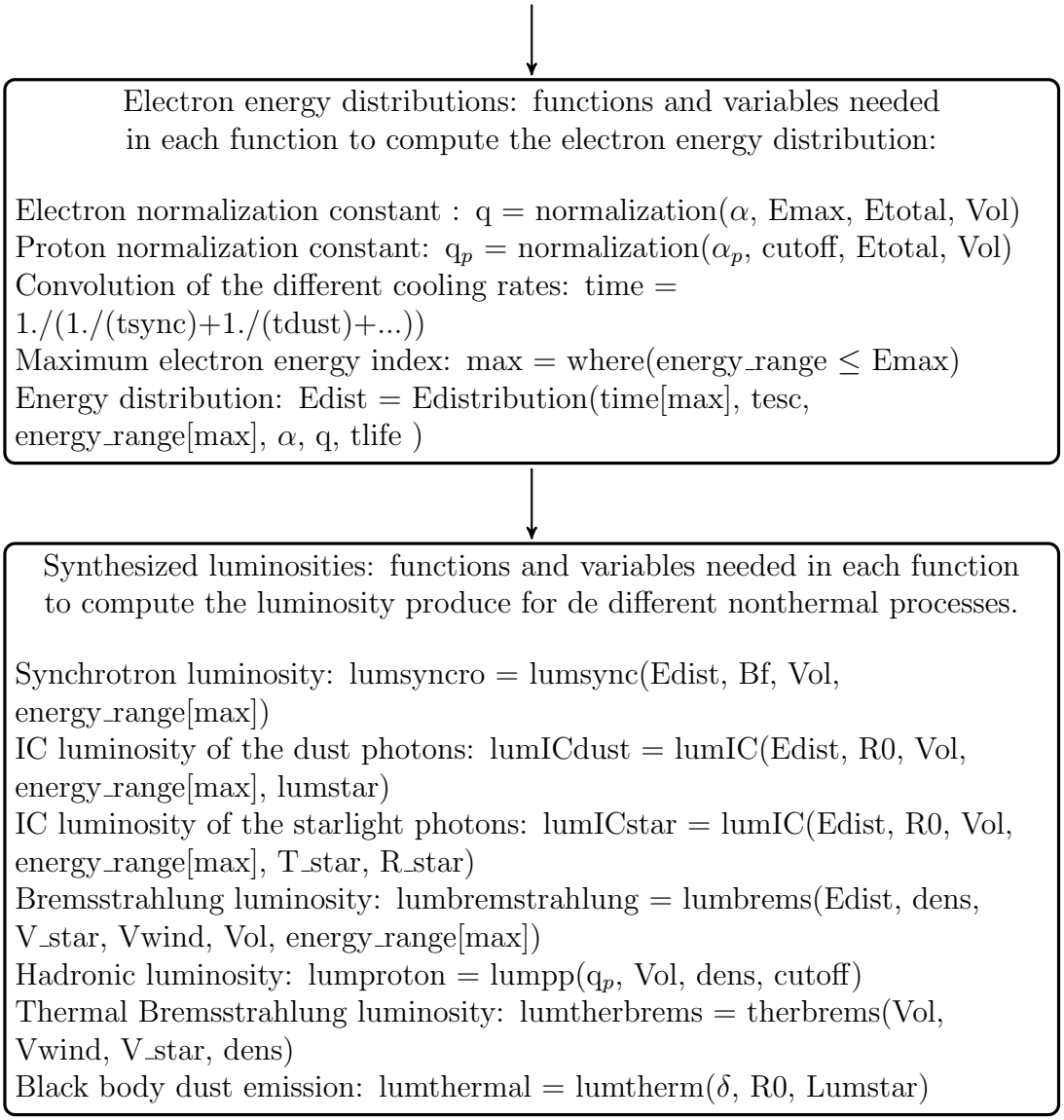

Figure 3.2: Step by step IDL pseudocode: procedure to obtain the different parameters needed to compute the synthesize spectrum. For each function are indicated the different variables required.

3.3.1 AE Aur

In Sec. 3.1 we explained that the star AE Aur was ejected from the Orion nebula cluster after an encounter of two massive binary systems, about 3 Myr ago. As a result of that interaction, the stars AE Aur and μ Col (both of spectral type O9.5V) were ejected at very high velocities, while ι Ori remained forming a very eccentric binary system with the two most massive stars (see Fig. 3.3). AE Aur is considered a runaway star for its high velocity ($v_* \approx 130$ km s^{-1}; Peri et al. [2012]). In its

path, this star found the dense molecular cloud IC 405 ($N_H \sim 3$ cm^{-3}, see Fig. 3.4). As a result of the interaction between the intense stellar wind ($v_\infty \approx 1500$ km s^{-1}; Hubrig et al. [2011]; $\dot{M} \sim 10^{-7}$ M$_\odot$ yr^{-1}) and the dust a bow shock was formed. This shock was first detected in the mid-infrared by Van Buren & McCray [1988] with *IRAS* data.

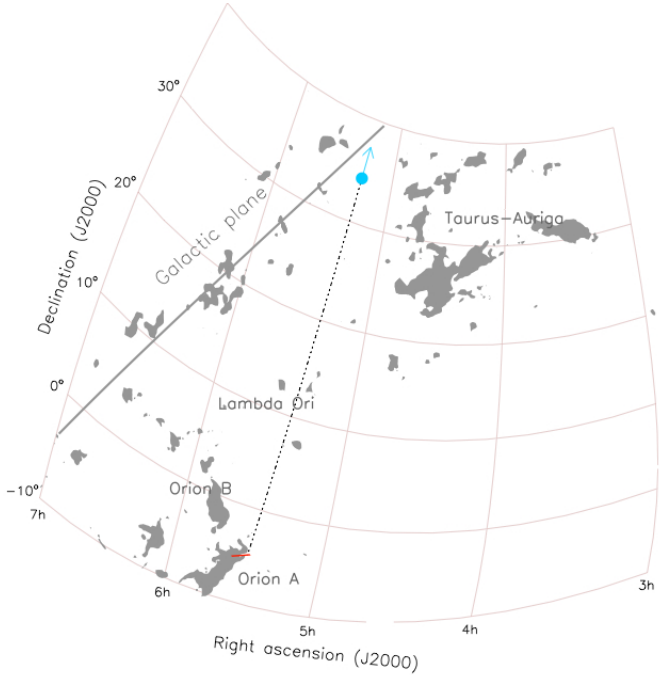

Figure 3.3: Trajectory follow by AE Aur from its ejection. The blue point represents the current position of AE Aur and the dotted line its trajectory; the red line represents the trajectory of ι Ori.

[López-Santiago et al., 2012] investigated the possibility of X-ray emission from the shock formed by the star AE Aur. Fig. 3.5 shows the WISE 12.1 μm image (in red) of the bow shock of AE Aur together with the corresponding EPIC pn count image in the 1-8 keV band (left panel, in green) and the pn median photon energy map, i.e., an image where each pixel holds the median energy of the detected pn photons in the 0.3-8 keV band (right panel in green), following the procedure adopted by Miceli et al. [2008]. A bright X-ray source, ~ 30" northwest of the star is visible in the left panel and appears embedded in the infrared bow-shock. The median photon energy map clearly shows that the X-ray emission from the bow shock source is significantly harder than that of the star. Namely, the average value of median photon energy is ~ 850 eV in the bow shock region and ~ 750 eV in the star region. Hence, the bow shock region emission is harder than the stellar region. They also try to fit the spectra to a power-law and to a very hot thermal component and concluded that the temperature needed to fit the spectra is very high, not corresponding to the temperature of the plasma at the distance where the star bow shock is formed.

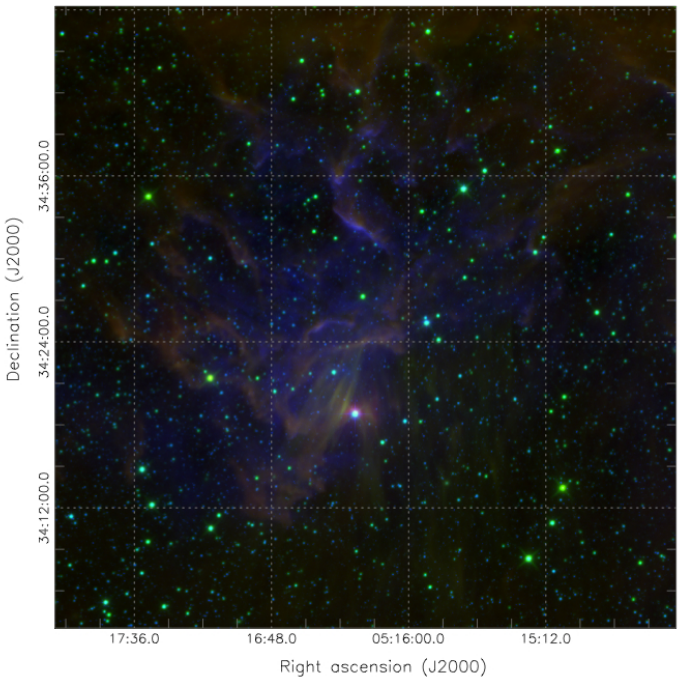

Figure 3.4: Colour composite image of IC 405. The bright white star slightly to the south from the image centre is AE Aur. Green: *Spitzer*/IRAC, band 1 (3.5 μm). Red: *Spitzer*/IRAC, band 4 (8 μm). Blue: DSS/PosII, red band.

The lack of infrared and optical counterparts and the extremely high temperature derived from the thermal model make the association of the bow shock with a foreground or background stellar object less likely. Furthermore, the spatial correlation between the bow shock and the infrared bow shock and the bow shape morphology of the hard X-ray emission around AE Aur, suggest that the bow shock is indeed the result of nonthermal emission originated by the runaway star.

3.3.2 Spectral synthesis

Our aim in this section is to synthesize the luminosity spectrum to test if that emission from the bow shock region is consistent with our nonthermal model. The stellar parameters of AE Aur used in the simulations are listed in Table 3.1.

The cooling time rates obtained for these parameters were represented in Fig. 2.6. The IC of the dust photons is the most effective cooling process, followed by the IC of the starlight photons. However, electrons with energies $E < 10$ GeV can not cool completely before they are convected away from the acceleration region. The maximum energy for the electrons to be accelerated, given by the point where the IC of the dust and the acceleration rate cross, is $E_{max} \sim 0.4$ TeV.

On the other hand, the electron energy distribution is the one used as an example in Sec. 2.3 (see Fig. 2.8). That is the distributions of electrons that is going to produce the nonthermal emission through the different cooling processes considered,

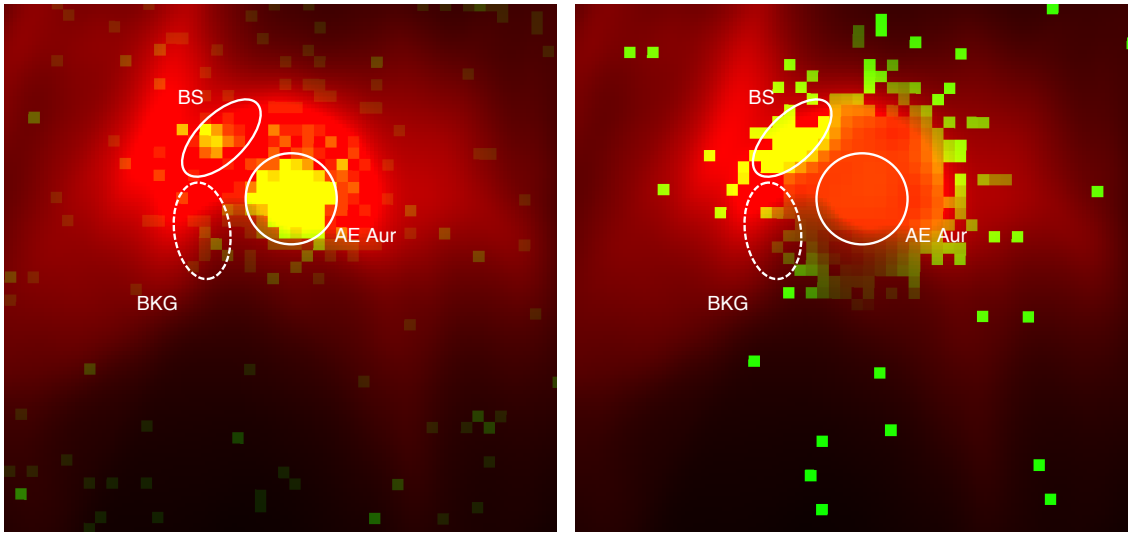

Figure 3.5: *Left panel*: WISE image (red) in the 12.1 μm and EPIC pn image in the 1-8 keV band (green). The pixel size is 4". The bow shock (BS) and background (BKG) regions are also indicated. North is up and East is left. *Right panel*: same as left but with the median energy map in the 0.3-8 keV range in green. Each pixel contains the value of the median energy of the pn photons detected in that band.

	Parameters	Values
$\dot{M}$	Wind mass-loss rate	$10^{-7} M_\odot$ yr^{-1}
V_w	Wind velocity	1500 km s^{-1}
R_0	Standoff radius	0.082 pc
$L_\star$	Luminosity of the star	0.7×10^5 $L_\odot$
$T_\star$	Stellar temperature	32 kK
$R_\star$	Stellar radius	8.9 $R_\odot$
n_H	Ambient medium density	2.3 cm^{-3}
$V_\star$	Stellar velocity	150 km s^{-1}
d	Distance	550 pc
Age	Bow shock lifetime	2.5 Myear
Δ	Shock width	0.3 R_0
α	Electron injection index	2
χ	Magnetic subequipartition fraction	0.2
q_{rel}	Content of relativistic particles	15%

Table 3.1: AE Aur parameters.

per unit of volume and per unit of energy. A wide range of electrons (from 1 MeV to 10 GeV) are more likely to escape from the acceleration region before they have time to lose all their energy, for this reason in the electron energy distribution there is a change in the slope for the same range of electrons.

We name L'_e the electron energy that is going to produce the nonthermal emission. As the electron energy distribution reaches a steady state (see Sec. 2.3) we can compute the total electron energy in the acceleration region that produce nonthermal emission from the electron energy distribution as

$$L'_e = V \int_{E_{\rm min}}^{E_{\rm max}} N(E') E' dE'. \tag{3.5}$$

We numerically obtained N(E), and hence can also integrate numerically (an analytical solution can also be obtained since the distribution can be parametrized by two power-laws). For this case we obtain that the total electron energy of those electrons that produce the nonthermal emission is 4.7×10^{41} erg.

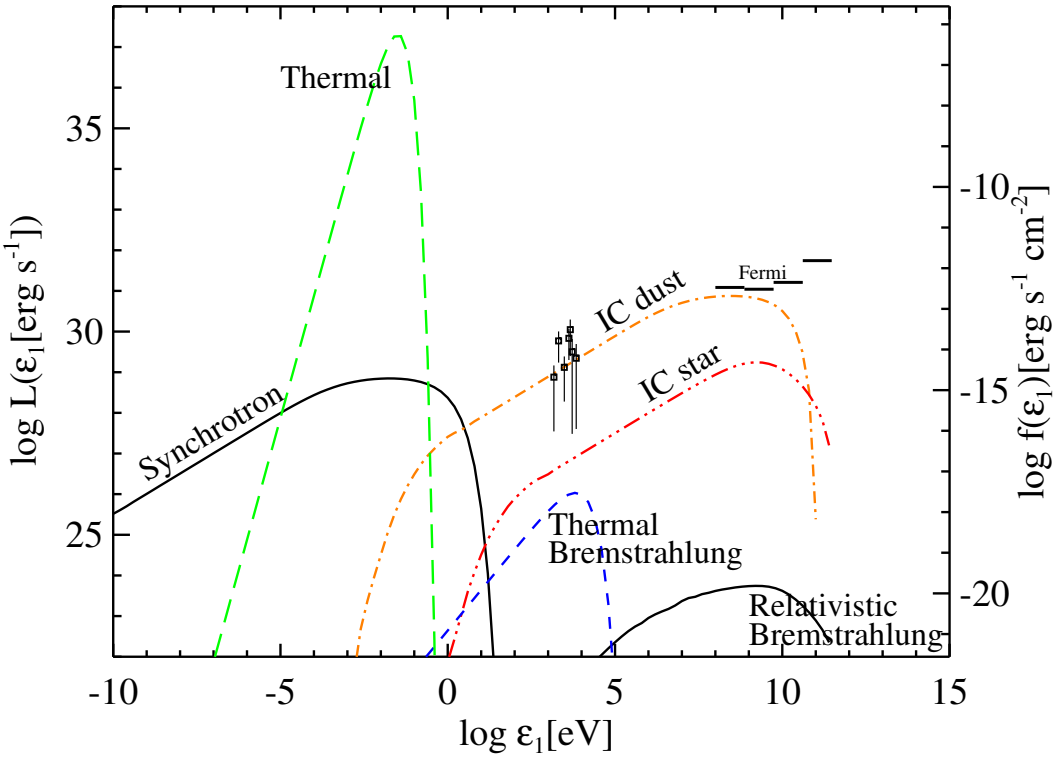

Figure 3.6: Synthesized luminosity spectrum for the bow shock formed by the star AE Au. The *Fermi* upper limit from Schulz et al. [2014] for this star is also included.

In Fig. 3.7 we plot the synthesized luminosity spectrum of the bow shock formed by the star AE Aur. From the emission reported by López-Santiago et al. [2012], given the low count rate of the source, statistical fluctuations are large and hence deeper exposures are necessary to obtain a proper study of the light curve. However, we aim at reproducing a spectrum than can fit the current X-ray data. For this matter, we obtain the following values for the free parameters of our model: the width of the shock results $\Delta = 0.3 R_0$, consistent with the X-ray bow shock region considered by López-Santiago et al. [2012]; $q_{rel} = 0.15$ (in agreements with del Valle & Romero [2012]); the magnetic energy is in subequipartition with respect to the

kinetic energy by a factor $\chi = 0.2$; and finally the electron injection index is $\alpha = 2$. Under this hypothesis, the X-ray emission from the bow shock formed by the star AE Aur can be explained by inverse Compton (IC) emission of the heated dust, with a very small contribution of the IC of the starlight photons. The synchrotron emission is important at radio frequencies, and the IR is dominated by the thermal emission. The thermal and the relativistic Bremsstrahlung are negligible compared to the IC of the dust and the starlight photons, and also the IC of the CMB photons, which is very faint and do not appear in the figure. The p-p contribution does not appear since the cooling time of the protons is much longer than the cooling time rate of the electrons, and hence they are removed from the radiation zone without having time to make a significant contribution to the spectral energy distribution.

The *Fermi* upper limits from Schulz et al. [2014] are also included, showing that no emission is expected in the GeV band. However, according to our simulations, the measures obtained by Schulz et al. [2014] from 57 months of *Fermi*-LAT data, show that GeV emission from AE Aurigae should be detected with only a few more months of observation.

3.3.3 BD+43 3654

BD+34 3654 has been reported to have formed a bow shock detected in the IR [Comerón & Pasquali, 2007] and in radio [Benaglia et al., 2010], and both observations are coincident and extensive. BD+34 3654 was observed with *XMM* during 47 ks and with *Suzaku*, but no X-ray emission has been detected from the bow shock. We also apply our model to study the possibility of nonthermal emission from the bow shock formed by this star.

The velocity of the BD+43 3654 is 67 km s^{-1} [Kobulnicky et al., 2010]. Comerón & Pasquali [2007] concluded that the origin of the high velocity of BD+34 3654 was the dynamical interaction between two massive binaries. On the contrary, Gvaramadze & Bomans [2008] determined that this star is a merged star formed via a close encounter between two tight massive binaries in the core of the association Cygnus OB2. The high linear momentum of the star indicates that the encounter was very energetic, and the most massive object is now seen as an O4If star. The star has now a massive (70 $M_{\odot}$) blue supergiant runaway star at 1.45 kpc

Other parameters of the star are a mass-loss rate 10^{-5} $M_{\odot}$ yr^{-1} [Markova et al., 2004; Repolust et al., 2004], a stellar wind velocity of 2300 km s^{-1} [Howarth et al., 1997], and the standoff radius is $R_0 = 1.5$ pc [Peri et al., 2012]; from Eq. 3.1 we derive a medium density of 5 cm^{-3} (see parameters listed in Table 3.2). The extensive emission in the radio and IR wavelengths are found at a distance consistent with R_0.

BD+43 3654 has one of the highest mass-loss rates among the O and B type stars [see Vink et al., 2001], as well as for the stellar wind [see Howarth et al., 1997]. This large amount of released energy and moderate space motion cause the bow shock to be formed far from the star. The high density in the interstellar region favors the formation of the shock. Taking these results into account, the values in the nominator of Eq. 3.1 are the highest for all the known stars, although the

value of the velocity of this star is moderated. Under these circumstances, a higher velocity would lead to a closer shock, whereas lower velocities would make BD+43 3654 not to be a runaway star. With such parameters, the bow shock formed by this star possibly represents an upper limit for the standoff radius of a bow shock formed by a runaway star. In Fig. 3.8 are represented the cooling time rates of the bow shock formed by BD+43 3654, the acceleration rate, the convection time and the bow shock lifetime.

Benaglia et al. [2010] suggest the detection of VLA radio emission is associated to the cooling of electrons by synchrotron emission. However, from our computations the radio points can be explained by the sum of the nonthermal synchrotron emission and the thermal emission of the shocked dust, also consistent with the MSX data at 0.1 eV (see Fig. 3.9). On the other hand, Fig. 3.8 shows that only electrons with energies ranging from 50 GeV to the maximum energy (2.2 TeV) have time to cool completely, producing a flattening before the cutoff region of the nonthermal processes. Here the IC of the dust photons, plus the thermal Bremtrahlung, hardly reach the XMM-*Newton* detection limit proposed by Hasinger et al. [2001] for 100

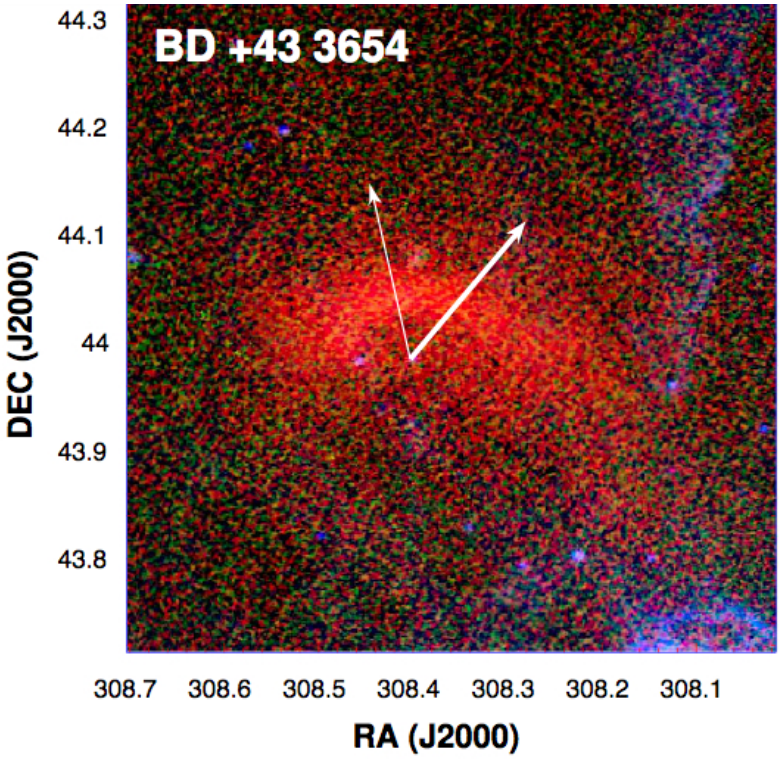

Figure 3.7: MSX images for BD+43 3654. Color mapping for MSX: blue, 8.3 microns; green, 12.1 microns; red, 21.3 microns. The vectors indicate the star proper motion: the thicker one represents the one derived from Hipparcos data; the thinner one is the same but corrected for the ISM motion caused by Galactic rotation. The vectors length are not scaled with the original values. Image obtained from Peri et al. [2012]

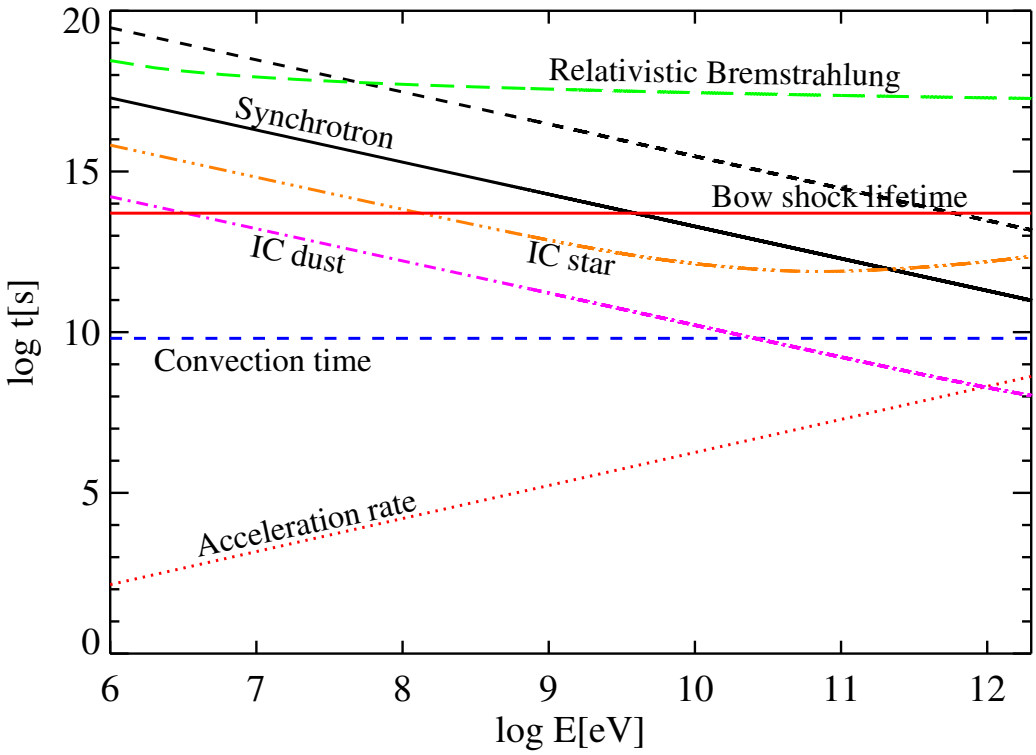

Figure 3.8: Cooling time rates for the electrons in the acceleration region of the bow shock formed by BD+43°3654. Again, the IC of the dust photons is the most efficient cooling process. The maximum energy of the accelerated electrons is 1.3 TeV

	Parameters	Values
$\dot{M}$	Wind mass-loss rate	$10^{-5} M_\odot$ yr^{-1}
V_w	Wind velocity	2300 km s^{-1}
R_0	Standoff radius	1.5 pc
$L_\star$	Luminosity of the star	8×10^5 $L_\odot$
$T_\star$	Stellar temperature	39 kK
$R_\star$	Stellar radius	19.4 $R_\odot$
n_H	Ambient medium density	5 cm^{-3}
$V_\star$	Stellar velocity	66 km s^{-1}
d	Distance	1450 pc
Age	Bow shock lifetime	1.6 Myear
Δ	Shock width	0.05 R_0
α	Electron injection index	2.1
χ	Magnetic subequipartition fraction	1
q_{rel}	Content of relativistic particles	10%

Table 3.2: BD+43 3654 parameters

ks. The values of the free parameters that fit the data are $\alpha = 2.1$, $\chi = 1$, $q_{rel} = 0.1$ and $\delta = 0.08$.

Despite the large number of free parameters used in our model and that only a few data points are available, our model predicts that the bow shock of this star could be observed with observations longer than 100 ks with XMM-Newton. BD+34 3654 was observed with XMM during 47 ks, which is not enough to detect the bow shock X-ray emission, according to our simulations. Terada et al. [2012] failed in detecting this bow shock with *Suzaku*. From their observations, they obtained an X-ray luminosity upper limit at 1.1×10^{32} erg s^{-1}, well over our predictions ($\sim 10^{30}$ erg s^{-1}). More recently, Toalá et al. [2016] were not also able to detect X-ray emission from the bow shock produce by this star, obtaining an integrated luminosity limit in the 0.4-4 keV band of 7.4×10^{32} erg s^{-1}.

3.3.4 Betelgeuse

Mackey et al. [2012] developed stellar evolution models and incorporated the evolving stellar wind into hydrodynamic simulations to simulate the transition of Betelgeuse from the blue supergiant (BSG) phase to the red supergiant (RSG) phase at the late stages of its life. At these phases, massive stars may undergo rapid

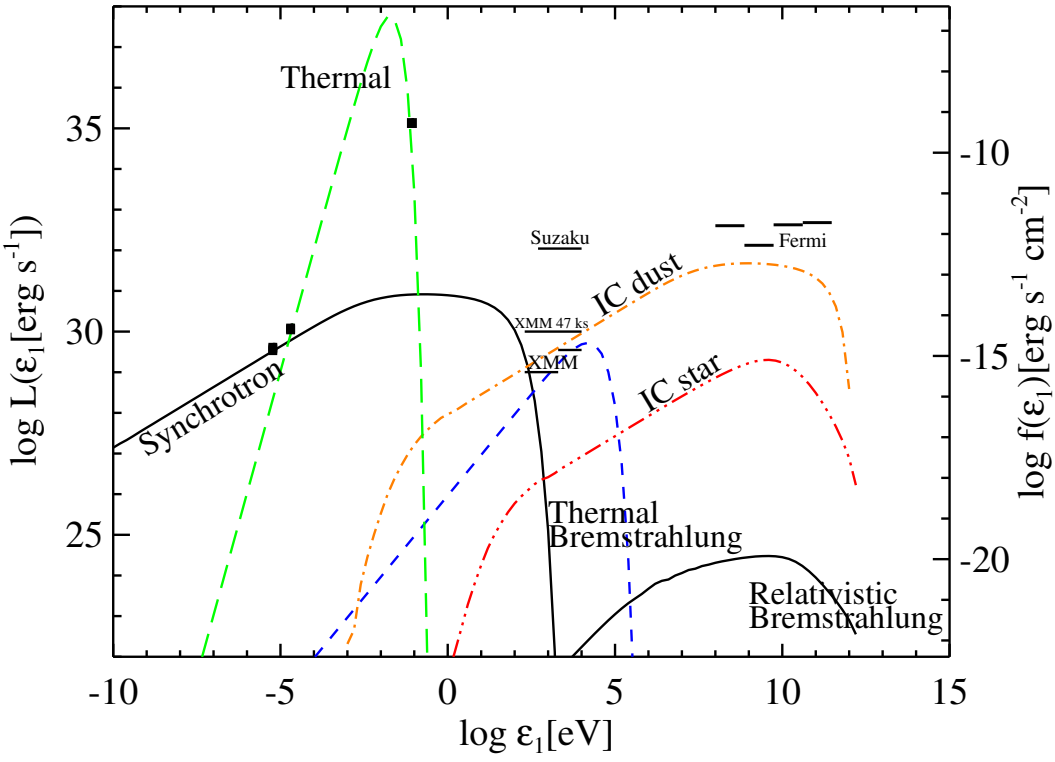

Figure 3.9: Luminosity distribution for the bow shock formed by BD+43 3654. We include the MSK (at about 0.1eV) and VLA observations from Benaglia et al. [2010]. and the *Fermi* upper limits for this star from Schulz et al. [2014].

transitions from red to blue supergiants and vice versa. The stellar wind velocities also change rapidly. During the transient phase from BSG to RSG the defunct wind of the BSG still reaches a few hundred kilometers per second, but at the RSG phase the wind velocity decreases down to $\sim$ 20 km/s, and hence the acceleration of particles is inefficient and the nonthermal processes are unable to produce high-energy photons in sufficiently large numbers to be detected with the current X-ray telescopes (see Fig. 3.10). Mohamed et al. [2012] found that the bow shock formed by Betelgeuse is still young ($<$ 30 kyr), but this bow shock has been formed by the defunct RSG wind, and hence is a weak shock, not able to emit high-energy photons.

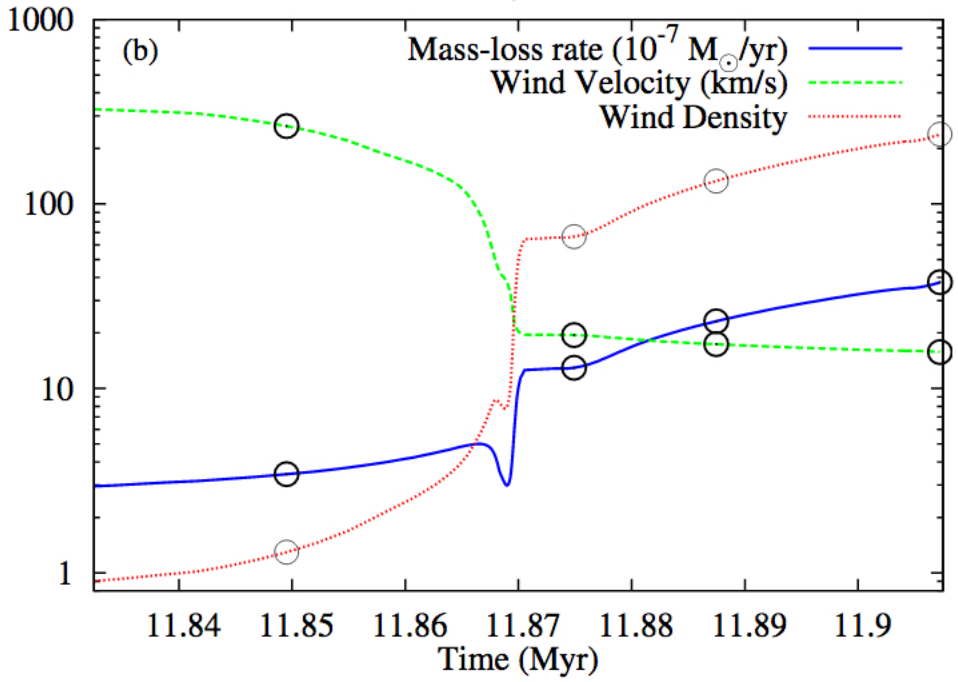

Figure 3.10: The starting point of the simulations performed by Mackey et al. [2012] corresponds to a lifetime of Betelgeuse of 11.4 Myr, about 400 kyr before the transition from BSG to RSG, produced at about 11.87 Myr. Although the mass-loss rate increases (blue line), the wind velocity falls in a greater proportion, reducing drastically the kinetic power available in the RSG wind.

Here we used the parameters derived by [Mackey et al., 2012] in their simulations (see Table 3.3) to test the possibility of a nonthermal high-energy emission prior to the transition phase from BSG to RSG. The total kinetic power is rather low compared to the O stars, but the star is relatively close and a possible low X-ray luminosity can still be detectable. The result is shown in Fig. 3.11. The IC of the dust photons can lead to the emission of detectable X-ray photons. We also include the *Chandra* detection mean limits reported by Posson-Brown et al. [2006] in the 0.1 - 6 keV range for this star, although they are less sensitive than the limit reported by Hasinger et al. [2001]. Our simulation shows that the most energetic photons

	Parameters	Values
$\dot{M}$	Wind mass-loss rate	$3.2^{-7} M_\odot$ yr^{-1}
V_w	Wind velocity	270 km s^{-1}
R_0	Standoff radius	0.63 pc
$L_\star$	Luminosity of the star	8×4.8^4 $L_\odot$
$T_\star$	Stellar temperature	9.12 kK
$R_\star$	Stellar radius	90 $R_\odot$
n_H	Ambient medium density	0.2 cm^{-3}
$V_\star$	Stellar velocity	50 km s^{-1}
d	Distance	200 pc
Age	Bow shock lifetime	30 kyear
α	Electron injection index	2

Table 3.3: Betelgeuse parameters during the transition phase from blue to red supergiant [Mackey et al., 2012].

could be detected. However, we recall that the current observations of Betelgeuse do not correspond to the transition phase from BSG to RSG, but to the present RSG phase. Hence no detection is expected in the current phase.

For our work, we simulated the case of a supergiant star and tested the possibility of nonthermal emission from runaway stars during the transition phase from BSG to RSG. The X-ray luminosity is slightly faint, but it can make up a new source of high-energy photons in the neighborhood of the Earth.

3.3.5 Emission from other stars forming bow shocks

AE Aur was the first star with a detected X-ray emitting bow shock, and BD+34 3654, although no detection has been found, has been a prior star for the study of nonthermal emission from bow shocks. Peri et al. [2012] reported a list of runaway stars with IR bow shocks detected in the infrared. Most of those stars have not been observed in X-rays. Schulz et al. [2014], with 57 months of *Fermi*-LAT data, test the possibility of GeV emission from the bow shocks formed by those stars (including AE Aur and BD+34 3654), although no emission in that band was detected for any star.

However, although our model can test the possibility of nonthermal emission of the bow shocks according to the parameters listed for them by Peri et al. [2012], by comparing the IC of the dust (responsible of the GeV emission) with the limits obtained by Schulz et al. [2014], the lack of X-ray and radio data from those shocks does not allow us to constrain the free parameters of our model. Nevertheless, we produced a grid of luminosity graphs for different parameter values. In particular, we tested two terminal velocity values, W_1=1100 and W_2=2000 km s^{-1}; three different mass loss rates values, $\dot{M}_1$=0.1, $\dot{M}_2$=1 and $\dot{M}_3$=5×10^{-6} $M_\odot$ yr^{-1}; two ambient medium densities, 0.1 and 2 cm^{-3}; two stellar velocities, 60 and 120 km s^{-1}; and two different values of the electron injection index, α_1=2 and α_2=2.3. In Table 3.4

we show the results for the different parameter combinations expressed in flux units for two different distances, at 300 pc (left Y-axis and in red) and at 600 pc (right Y-axis and in orange). In some cases, due to the large amount of points increase the computational time needed for the the simulations, we reduce the number of points, which produces jumps at the beginning of the IC luminosities, but do not affect to our purposes. The XMM-*Newton* detection limit proposed by Hasinger et al. [2001] for 100 ks and the *Fermi* upper limit from Acero et al. [2015] are also included.

The electron injection index, the mass loss rate and the wind velocities are the parameters that most influence the resulting emission produced by the nonthermal processes. In particular, a combination of low electron injection indexes, high mass loss rates and high terminal wind velocities almost assure detectable X-ray photons production at the two different distances computed, as expected. In some cases even the emission at the GeV band could be detected with the most recent *Fermi* limit observations. The density and the velocity of the star are also major parameters to produce or not a bow shock, but once the bow shock is formed, the other three parameters have more influence on the emission mechanisms.

The synchrotron emission is responsible of the radio emission. However, high ambient medium densities favor the enhancement of the synchrotron emission, shift-

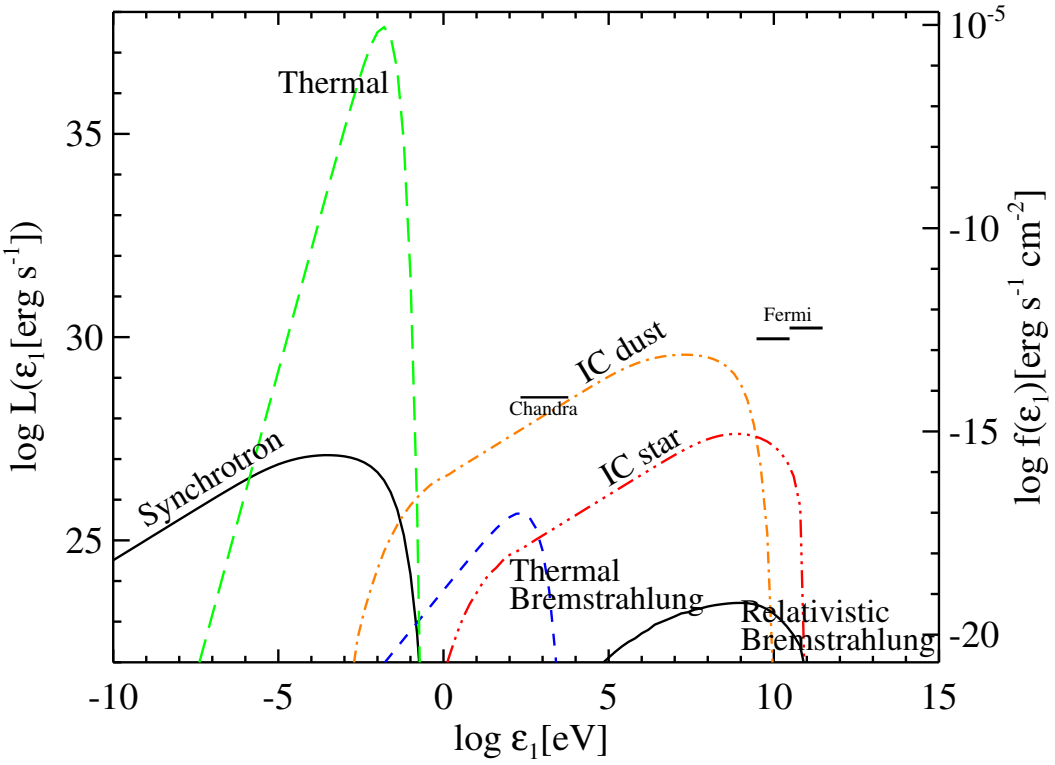

Figure 3.11: Luminosity distribution for the bow shock formed by Betelgeuse during the transition phase form blue to red supergiant before the current red supergiant phase.

ing in some cases the synchrotron tail at high energies to the X-rays wavelengths, adding its contribution to the IC of the dust photons, but in general the IC of the dust photons is the most important mechanism for the X-ray photon production. The IC of the stellar photons is way less intense than the IC of the star photons. The relativistic Bremsstrahlung is very weak for the parameters we have considered, and is not shown.

On the other hand, the thermal Bremsstrahlung, is then not affected by the electron injection index, but affected by the wind velocity, the mass loss rate, the stellar velocity and the ambient medium density. In some cases, it can be a so relevant emission process as the IC of the dust photons. In those cases, the possible X-ray detectable emission would be produced by the contribution of thermal and nonthemal processes. The thermal emission of the dust is the most important process in the IR band.

Due to the lack of X-ray observations of bow shocks around runaway stars, we discuss the possibility of X-ray detection according to the results of our simulations for the different stars listed in Peri et al. [2012] (see also parameter values therein, and Appendix A of this work), which are not only runaway stars, but also runaway stars in which an IR bow shock has been detected with WISE. Most promising candidates are highlighted in boldface.

- **HIP 2036**: Has not been observed in X-rays with either *Chandra* or XMM-*Newton*. The stellar velocity is rather low, the terminal velocity is about 1200 km s^{-1} and the mass loss rate is 4.8×10^{-7} $M_{\odot}$ yr^{-1}. The distance is about 750 pc. Pictures 25 and 26 represent the most similar situation corresponding to this star, except for the density. High ambient medium densities, according to Eq. 3.1 reduce the standoff radius length, and according to Eqs. 2.15 and 2.18, the IC luminosity of the dust and of the stellar photons is enhanced, specially the IC of the stellar photons. On the other hand, the distance reduces the flux. However, the synchrotron emission at X-rays wavelengths its important at high ambient medium densities, as in this case, hence possibly leading to X-ray synchrotron emission, which is add to the IC of the dust photons and to the thermal Bremsstrahlung, probably producing observable X-ray photons.

- HIP 2599: 1 or 7 are the pictures that best represent the possible emission from the bow shock formed by this star. Although a supergiant star, is a B1 star, and hence the mass loss rate is low (0.12×10^{-6}). Furthermore, the star is at 1.5 kpc, making more difficult the possibility of the bow shock to be detected. Even for 600 pc, one of the distances we simulate, none of the combinations we have computed results in a detectable flux for low mass loss rates. Thus, it seems very unlikely that this star can produce a detectable non-thermal bow shock at X-rays.

- **HIP 11891**: Pictures 29 and 35 correspond to simulations with parameters very close to those of the star. A low injection index (2) is more likely to produce a detectable shock in the X-ray band that a higher index. The star is at 900 pc, hence weakening the possible flux on Earth, but on the other hand,

the wind velocity is 2800 km s^{-1}, higher than the 2000 km s^{-1} we simulate. The wind velocity is a very important parameter that enhances the emission of both the thermal and the nonthermal processes. Hence, if the electron injection index is low, the high terminal velocity can lead to an enhancement of the IC of the dust photons, producing a detectable X-ray flux, despite the distance of the star, through a long exposure time.

- HIP 16518: is a B1 main sequence star, with a very low wind velocity and a very low mass loss rate. Hence the luminosity processes considered are very faint and also the distance (650 pc) reduces the possibility of detection. We do not expect X-ray emission from the bow shock formed by this star.

- HIP 17358: Although the star is very close, at only 150 pc, is a B5 star, with a very low mass loss rate ($\leq 10^{-9}$ $M_\odot$ yr^{-1}) and a low wind velocity (500 km s^{-1}) the luminosity processes are very weak, not leading to a detectable X-ray flux. We discard the possibility of a high-energy emitting bow shock.

- HIP 22783: Is a supergiant O9.5 star, with a strong wind velocity (1600 km s^{-1}) but a not very high mass loss rate (0.25×10^{-6} $M_\odot$ yr^{-1}). The ambient medium density is also low (0.02 cm^{-3}). This combination of parameters lead to a long standoff radius, about 4.7 pc from the star. Pictures 4 and 10 well represent the situation of the bow shock formed by this star, however, even for 600 pc no detectability is expected, and this star is at 1.6 kpc, out of any detection possibility with such parameters, according to our simulations.

- HIP 25923: Picture 25 best represents the situation of this star. Is a B0 star at 900 pc, with a very weak mass loss rate, 0.06×10^{-6} $M_\odot$ yr^{-1}. According to our simulations, no detection is expected.

- HIP 26397: Although a close star, at 350 pc, is a B0.5 main sequence star, with a very low mass loss rate, and a low terminal wind velocity, which reduces the effectiveness of the emission mechanisms, and hence no detectable emission is expected.

- HIP 28881: This is an O8 main sequence star, with an intense wind velocity. However, is at 1.5 kpc, and as an in other cases, that distance reduces the possibility of detection of a X-ray flux. The emission can be high, but the flux is too low when arrives the Earth at such distance.

- HIP 29276: is a B1 supergiant star, but its terminal wind velocity and the mass loss rate are very weak to produce a detectable emission at 400 pc. Our weakest bow shock simulated is the one represented in Picture 1, and the parameters of this star are well below those chosen for that simulation.

Table 3.4: $N_H = 0.1$ cm^{-3}, $V_\star = 60$ km s^{-1}

	α_1		α_2	
$\dot{M}$	W_1	W_2	W_1	W_2
$\dot{M}_1$	1 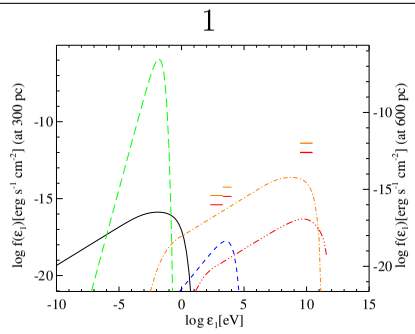	4 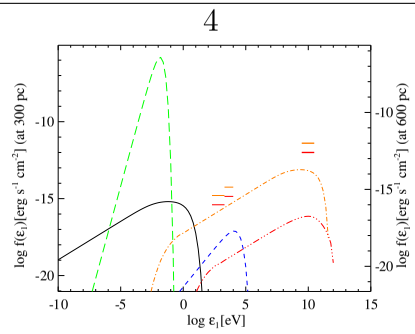	7 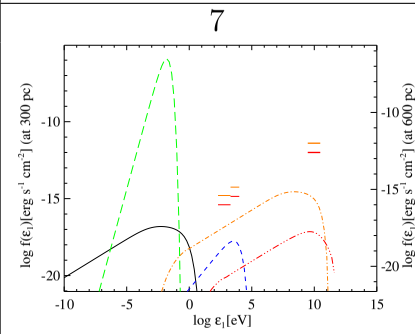	10 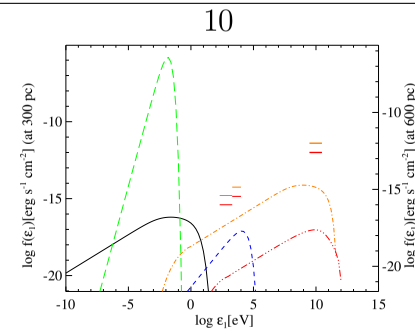
$\dot{M}_2$	2 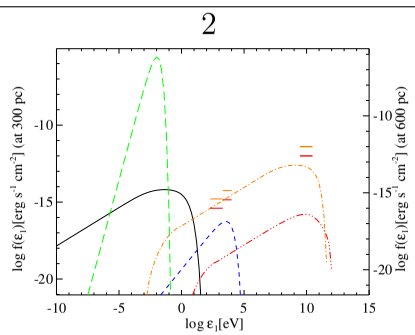	5 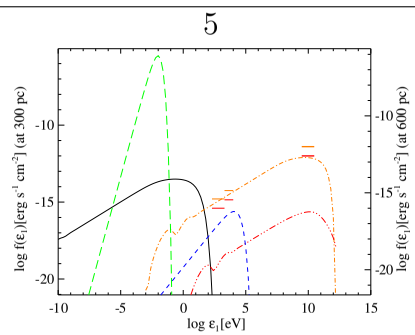	8 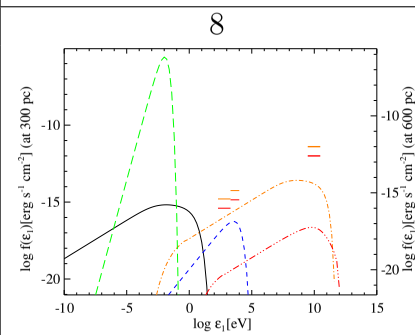	11 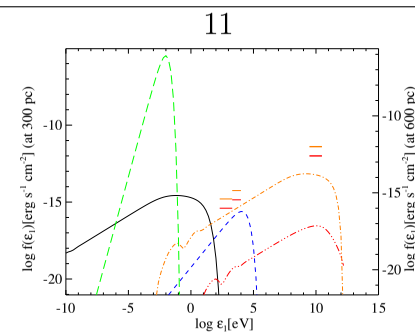
$\dot{M}_2$	3 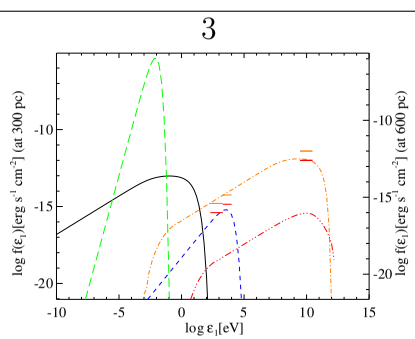	6 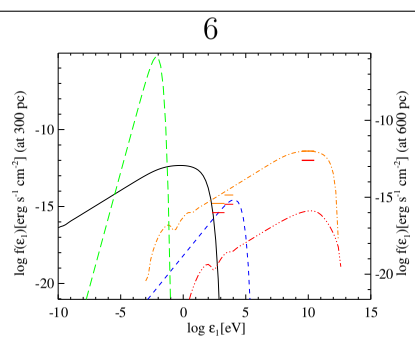	9 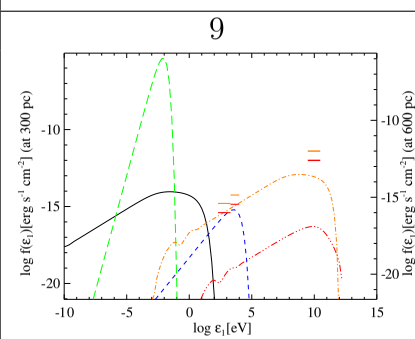	12 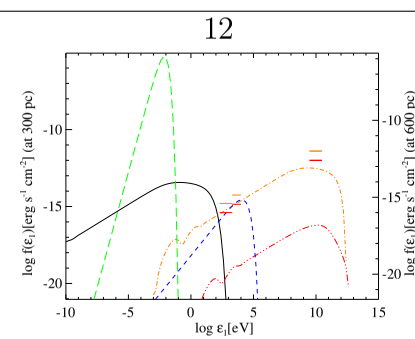

Table 3.4: Electron injection indexes: α_1=2 and α_2=2.3; Terminal wind velocities: W_1=1100 and W_2=2000 km s^{-1}; Mass loss rates: $\dot{M}_1$=0.1 $\times 10^{-6}$, $\dot{M}_2$=1$\times 10^{-6}$ and $\dot{M}_3$=5$\times 10^{-6}$ $M_\odot$ yr^{-1}. Red lines represent the *XMM-Newton* upper limits from Hasinger et al. [2001] at 300 pc, for an observation of 100 ks and the Fermi upper limit from Acero et al. [2015]; orange lines represent the same but for 600 pc.

Table 3.4 (cont.): $N_H = 0.1$ cm^{-3}, $V_\star = 120$ km s^{-1}

	α_1		α_2	
$\dot{M}$	W_1	W_2	W_1	W_2
$\dot{M}_1$	13	16	19	22
$\dot{M}_2$	14	17	20	23
$\dot{M}_3$	15	18	21	24

Table 3.4 (cont.): $N_H = 2$ cm^{-3}, $V_\star = 60$ km s^{-1}

$\dot{M}$	α_1		α_2	
	W_1	W_2	W_1	W_2
$\dot{M}_1$	25	28	31	34
$\dot{M}_2$	26	29	32	35
$\dot{M}_3$	27	30	33	36

Table 3.4 (cont.): $N_H = 2$ cm^{-3}, $V_\star = 120$ km s^{-1}

$\dot{M}$	α_1		α_2	
	W_1	W_2	W_1	W_2
$\dot{M}_1$	37	40	43	46
$\dot{M}_2$	38	41	44	47
$\dot{M}_3$	39	42	45	48

- HIP 31766: Although a O9.7 supergiant, with parameters closer to Pictures 5 and 11, the star is at 1.4 kpc, well over the distances we have considered. No X-ray detection is expected.

- HIP 32067 and HIP 34536: As in the previous star, the large distances at which these stars are found, 2.1 and 1.3 kpc respectively, impede that the bow shocks formed by these stars can be detected in X-rays, although they are O5.5 and O6.5 main sequence stars, with high wind velocities.

- **HIP 38430**: Pictures 29 and 35 best represent the combination of parameters of this star. Although it is at 900 pc, the high wind velocity (2600 km s^{-1}), a mass loss rate of 0.7 $M_{\odot}$ yr^{-1}, can produce both great IC of the dust and thermal Bremsstrahlung luminosities. On the other hand, the high ambient medium density (60 cm^{-3}) enhances the synchrotron emission, adding its contribution to the two previous processes. It has never been observed with *XMM-Newton*, but according to our simulations, a low injection index would favor the emission of a detectable flux in the X-ray band, despite the distance is high.

- HIP 62322: is the closest star of the survey, but is B2.5 V star, with a very low mass loss rate (6×10^{-9} $M_{\odot}$ yr^{-1}) and a very low terminal wind velocity (300 km s^{-1}). Our simulations show no possible of high-energy detection from the bow shock formed by this star.

- **HIP 72510**: Is a giant O6.5 star. It has a high wind stellar velocity, 2545 km s^{-1} and an important mass loss rate of 0.26×10^{-6} $M_{\odot}$ yr^{-1}; furthermore, it is very close from the Earth, at only 350 pc of distance. Pictures 4,5 and 10,11 are the best approaches to this bow shock. Taking into account that in our pictures we consider a terminal velocity of 2000 km s^{-1}, and that the real density is de double (0.2 cm^{-3}) of the one we consider (only 0.1 cm^{-3}), and also considering the distance of the star, we expect a detectable flux of high-energy photons from this star if a low electron injection index (2) rules in the region, although long exposures may be needed.

- HIP 75095: Pictures 25 and 31 describe a situation similar to the combination of parameters of this bow shock. Despite the high ambient medium density around the bow shock (40 cm^{-3}), the star is at 800 pc, too far to detect a high-energy emitting bow shock, according to our simulations.

- HIP 77391: Is a supergiant O9 star embedded in a high dense medium (30 cm^{-3}). Configurations, 28 and 34 resemble the configuration of the parameters of this for shock. No detection is expected at 800 pc according to our simulations, and even considering that the high density favors the synchrotron emission to produce high-energy photons, the detection of this bow shock in the X-ray band seems unlikely.

- **HIP 78401**: The representations in figures 25 and 31 are very similar to the parameters corresponding to the bow shock formed by this star. The X-ray

emission shown is rather low; however, the star is very close to the Earth, at 224 pc, and also the terminal wind velocity is somehow greater than the used in the simulations. Hence, it is possible that, if the electron injection index is low in the acceleration region, the bow shock is detectable at high energies.

- HIP 82171: Is a supergiant B0.5 star at about 850 pc. Figures 37 and 43 are good representations for the bow shock parameters of this star. The low mass loss rate and the large distance to the star impedes the detection of nonthermal photons from the bow shock formed by this star.

- HIP 88652: The parameters of this star favor the emission of nonthermal X-rays photons, but its distance (650 pc) is too large to detect them from Earth. Figure 29 would represent the most favorable situation for this star, but only for lower distances the photon flux could be detected.

- HIP 92865: Is a O8 main sequence star. Although close to the Earth (at only 350 pc), the ambient medium density and the mass loss rate are very low, and hence a very low flux of nonthermal photons is expected.

- HIP 97796, HIP 101186 and and HIP 114990: this stars are found at 2.2, 1.5 and 1.4 kpc respectively, and at such distances even for efficient shocks in producing X-ray nonthermal photons the expected fluxes on Earth are very low.

After the study of these stars around which a bow shock is detected in the IR, we can conclude the high-energy emission from a bow shock formed by a runaway star is somehow difficult. First, because not all runaway stars can form a bow shock, even weak: some of them can cross the ambient medium without forming a bow shock, either because the star releases great amounts of energy in a weak medium, or because the star do not encounter a sufficiently dense cloud. Second, because the maximum X-ray luminosity from the bow shocks is lower than 10^{30} erg s^{-1}, which produces low fluxes at certain distances; hence, from our results, it seems difficult to find X-ray emitting bow shocks at further distances than 600 pc, reducing the high-energy detectability to the neighbourhood of the Sun. Furthermore, from our analysis we conclude that, in general, long exposures are needed to detect bow shocks in X-rays, even in the most energetic cases. However, the next generation of X-ray telescopes (i.e. Athena) will have a higher effective area and will make easier to detect these sources with lower exposure times, and enhancing the distances at which shocks could be detected.

Chapter 4

Nonthermal emission from supernova remnants

4.1 Brief introduction to Supernovae nature

Supernovae are stellar explosions that can reach luminosities of the order of 10^9 - 10^{10} $L_\odot$. Later, the luminosity decreases fast on time scales of days or months, but in most cases the remnants of the supernovae are still visible as luminous sources containing the material ejected during the explosion.

Most supernovae are caused by the gravitational collapse of very massive stars. Along the relatively short live of massive stars, the nuclear fusion processes that take place in their nucleus synthesize heavy elements from light elements, and the resulting metals are distributed in shells, with the heaviest occupying the inner shells while the lightest moving in outer shells. On the other hand, other supernovae are caused by the termonuclear explosion of a white dwarf. In both cases, the outer layers of the star after the explosion form the well known supernova remnants (SNR).Hence, two scenarios are considered [Battaner, E., 1999]:

1. Supernovae explosions can occur at the end of the evolutionary stage of massive stars (zero age main sequence mass higher than 8 $M_\odot$). When the nucleus of a massive stars synthesize enough iron, the star is not able to produce nuclear reactions in its nuclei anymore (the binding energy of the Fe nucleus is the highest, and hence the production of elements heavier than Fe absorbs energy, thus is not a favorable process), and the pressure of degenerated electrons is not high enough to maintain the structure of the star. Hence, the core of the star collapses gravitationally rapidly until it reaches a critical density. At that moment, the outer shells rebound and are expelled out to the interstellar medium.

   In the collapsing process (a free fall process), the density and the temperature reach very high values inside the stellar nucleus. This collapsing process takes place in a time scale of about one second, and in this stage protons capture electrons, and hence neutrinos are released, carrying energy with them. When the density of the stellar nucleus reaches values close to those found in atomic

nuclei, the collapse is suddenly stopped forming a very compact inner nucleus. When the outer layers impact this rigid nucleus are then bounced back sweeping all the stellar material, shocking the circumstellar material and the interstellar medium, releasing large amounts of potential energy as a supernova. The nucleus of the star survives the explosion and continue collapsing. Depending on the mass, if neutrons can stop the collapse, a neutron star arises, but if the mass is high enough, a black hole appears.

2. The other possible scenario occurs when a C-O white dwarf star in a close binary system accumulates enough material from its companion to exceed the Chandreasekar limit. In this case, the raise of the nuclear temperature triggers nuclear fusion reactions that produce the instant fusion of the nucleus and the explosion of the star. The star explodes completely, ejecting its shells at very high velocities. In this case, no residuum is left in the center of the explosion.

SN 1006, SN 1054, SN 1181, Tycho's supernova of 1572 and Kepler's supernova of 1604 are examples of the most famous and youngest supernovae in our neighbourhood. In particular, they all were naked eye observed supernovae (they were observed before the development of the first telescopes). Actually, they were very important in the science history since they were the prove that the Universe beyond the Moon and the known planets is changeable, against the Aristotelian idea of an immutable universe. However, the development of modern telescopes opened new insights about the production and formation of supernovae, particullarly when they were detected in other galaxies, such as SN 1885A in the Andromeda Galaxy. Soon, it was discovered that they were standard candles [Kowal, 1968] and hence that they could be used to measure astronomical distances.

Supernovae are classified into two general groups, named Type I and Type II, distinguished by the presence (Type II) or not (Type I) of Hydrogen lines in the optical spectrum (Balmer series). The explanation of this difference is explained by the presence of hydrogen outer shelf in the progenitor star in the case of Type II supernovae, while in the progenitors of Type I supernovae those hydrogen envelopes have disappeared, either because strong mass-loss rates remove those layers or because the progenitor was a white dwarf that has lost the Hydrogen surface during their evolution. However, new distinctions are made in each group, as described in Table 4.1 (adapted from Turatto [2003]).

Among all types of supernovae, Type Ia supernovae have very particular and important features. First, they are reported to be present in all kind of galaxies, including elliptical galaxies which only contain old stellar populations, and are associated with old or intermediate-age stars. Hence, they are supposed to explode into a uniform circumstellar medium (at least into one which is not modified by mass loss in the form of stellar wind, [Berezhko et al., 2012]) As they do not present Balmer lines, are mostly associated with the explosion of accreting white dwarfs, which have no hydrogen envelopes. Second, their light curves are generally very similar, and the maximum luminosity and the width of the curve at the maximum is also similar [Phillips, 1993]; furthermore, they are the most luminous supernovae. About 25 - 30% of observed supernovae are of Type Ia.

Table :Supernovae Classification

Type	Characteristics
Type I, absence of Balmer lines	
Ia	Singly ionised silicon Si II at 615.0 nm.
Ib	Neutral He I line at 587.6 nm.
Ic	Weak or absent Helium lines.
Type II, hydrogen optical lines present in the spectrum	
IIP	Reaches a plateau in its light curve. No narrow lines.
IIL	Linear decrease in its light curve. No narrow lines.
IIn	Some narrow lines.
IIb	Spectra similar to Type II ar early stages, but changes to become like Ib/c at later times.

The rest of supernovae are only found close to star-forming regions, which indicate that they are more likely to be produced by the core collapse of massive stars. Type Ib and Ic do not present Hydrogen lines. Type Ib supernovae present strong He lines, which are lacking in Type Ic. They are found in star-forming regions, and are associated with the core collapse of massive stars that has lost their Hydrogen envelopes before the explosion. On the other hand, Type II supernovae show Hydrogen lines and occur in star-forming regions placed in the spiral arms of galaxies. Hence, these supernovae correspond to the explosions of short-lifetime massive stars. About 50% of the supernovae explosions are of this type.

4.2 SNR as particle acceleration sites

When a star explodes as a supernova, the ejected material expands into the ambient medium. The beginning of the expansion is known as the free expansion phase. Initially, the expansion velocity is almost constant as the piled material is small compared to the ejected mass, but soon the shock velocity expansion decreases as because part of the kinetic energy is transferred to the ambient medium. In the next phase, the Sedov phase, most energy is transferred from the ejected material to the shock heating. The radiative cooling is negligible in this phase, and hence the expansion is adiabatic. Finally, when the post-shock temperature increases, radiative losses become significant, and the radiative phase starts. Relativistic particles are accelerated during the first two phases, the free expansion and the Sedov phase. During the radiation phase the shock velocity decreases, and hence an important fraction of the shock energy is lost by radiation and the acceleration efficiency decreases [Helder et al., 2012].

Supernova remnants (SNRs) are thought to be major factories producing relativistic particles in our Galaxy. Fermi and other high-energy observatories have made enormous strides in detecting Cosmic Rays (CR) γ-ray emissions from SNRs [e.g Brandt et al., 2015]. When combined with complementary X-ray and radio data, these γ-ray observations have finally led to the determination of the leptonic

and hadronic nature of CRs in a few systems. However, there are still very few systematic study of CRs in SNRs, largely because of the difficulty in decomposing the γ-ray emission from leptonic and hadronic CRs. Such decomposition requires modeling the broad-band spectral energy distribution (SED) from radio-wavelenghts to γ-rays.

In order to decompose hadronic from leptonic emission, we need radio and hard X-ray data to characterize the shape of the synchrotron emission by CR electrons, and GeV/TeV data to characterize and disentangle the IC leptonic emissions, and the π^0 decay hadronic emission. Hot gas and dust can be associated with the optical and infrared emission from the SNRs, and the X-ray emission can be produced by the thermal bremsstrahlung of the very hot gas heated by the supernova wave but can also be produced by synchrotrons losses of high-energy electrons if the SNR becomes an efficient acceleration site. The synchrotron radiation of ultra relativistic electrons is responsible for the radio emission.

The Cherenkov telescope *H.E.S.S.* has detected γ emission from, for example, the SNR RX J0858.0-4622 [Aharonian et al., 2007] or from the SNR of SN 1006 [Acero et al., 2010]. Aharonian et al. [2007] and Acero et al. [2010] proposed the possible origin of the γ emission could be the IC of the X-ray or CMB photons or from the p-p inelastic collisions. These conclusions encourage us to introduce our non-thermal model in the study of the emission detected in these objects.

The interest in the high-energy emission from SNRs comes from their association as candidates to cosmic-ray acceleration. First, because SN release sufficient kinetic energy to explain the estimated Galactic luminosity in cosmic rays, and second, because diffusive shock acceleration provides a viable mechanism to accelerate particles at the shock fronts. Actually, most shell type SNRs are synchrotron radio emitters, which confirms that electrons are accelerated up to at least GeV energies. Baade & Zwicky [1934] assume that about 10% of the energy released in the explosion of a supernova is turned into Cosmic Rays (CR), in order to explain the energy density of the observed CR in our galaxy. However, the fraction of energy in the explosion converted into CR energy is still debated. In Secs. 2.4.2 and 2.4.4 we saw that either the IC of the dust and the proton-proton inelastic collision could be responsible for the γ-ray emission. However, so far, γ-rays from some SNRs have been historically explained by hadronic processes (see Li & Chen [2012]), although recent studies are also considering the possibility of a leptonic origin of the γ-rays emission (see, for example, Acero et al. [2010] and Miceli et al. [2014]). Here we try to clarify the origin of the emission detected around the supernova remnant of SN 1006.

4.3 SN 1006

SN 1006 is a Type Ia supernova remnant [Schaefer, 1996] and the brightest (in apparent magnitude) supernova reported and is an ideal target to study the acceleration process in astrophysical shocks. It exploded in 1006 AD as Chinese and Islamic observers divulged. It is a dynamically young remnant with a shock velocity of $v_s \sim 5000$ km s^{-1} [Winkler et al., 2014]. The surrounding ISM has a density of

$n_H \sim 0.035$ cm^{-3} [Miceli et al., 2012], and the radius of the remnant is about 15'. This remnant was first identified at radio wavelengths [Gardner & Milne, 1965]. Winkler et al. [2003] derived a distance of 2.2 kpc.

The source SN 1006 was the first SNR in which a nonthermal component of X-rays was detected in the rims by ASCA [Koyama et al., 1995] and ROSAT [Willingale et al., 1996]. The spectrum suggested that electron can be accelerated up to ∼100 TeV. Subsequent *Chandra* and *XMM* images are now major data to study the origin of the nonthermal emission.

Here we try to explain the emission at different wavelengths by using our model developed in Chapter 2. We aim to clarify the different possible contributions to the spectrum of the SNR of SN 1006. The results were published in Miceli, M., Orlando, S., Pereira, V. et al. [2016].

SN 1006 shows a morphology characterized by two opposed radio, X-ray, (and γ-ray) bright limbs dominated by nonthermal emission (bilateral SNR) and separated by an inner region of low surface brightness and soft, thermal X-ray emission [Miceli et al., 2012]. The nonthermal limbs suggest the presence of highly efficient particle acceleration. Fig. 4.1 (extracted from Miceli et al. [2012]) shows an image of the SN 1006 in two energy bands:

- Left panel shows the *XMM* MOS count-rate in the 0.5-0.8 keV band, mainly corresponding to the thermal emission.
- Right panel shows the *XMM* MOS count-rate in 2-4.5 keV energy band, which corresponds with the nonthermal emission.

The figures also shows the symmetry axis of the remnant. Overlapped regions marked from a to h were used by the authors to quantify the possible shock modification along the rim: where nonthermal emission is stronger, shock compression must increase. In conclusion, Miceli et al. [2012] found that the shock compression ratio increases from 4 up to 6 in regions of the southeastern rim that are closer to the nonthermal limbs. This can be naturally interpreted as a result of shock modification induced by hadron acceleration.

Although SN 1006 is expanding in a tenuous environment, the remnant interacts with ambient interstellar clouds. A higher ambient density is observed in the northwestern rim, where the shock is slowed down by the interaction with dense material (the northwestern cloud), producing a relatively bright and sharp H_α filament and soft X-ray emission [e.g. Li et al., 2015; Winkler et al., 2003]. However, particle acceleration is not very efficient in the northwestern limb, as revealed by the very faint nonthermal emission.

On the other hand, according to Fig. 4.1, the southwestern limb shows both efficient particle acceleration and relatively high ambient density in the cloud, thus being a privileged site for the detection of γ -ray emission. To study the nonthermal emission from the SW limb of the SNR 1006, we used the MHD model developed by Orlando et al. [2012]. Based in this model, in Miceli, M., Orlando, S., Pereira, V. et al. [2016] is reproduced the interaction of the southwestern limb with a dense cloud, as derived from HI observations (see Fig. 4.2).

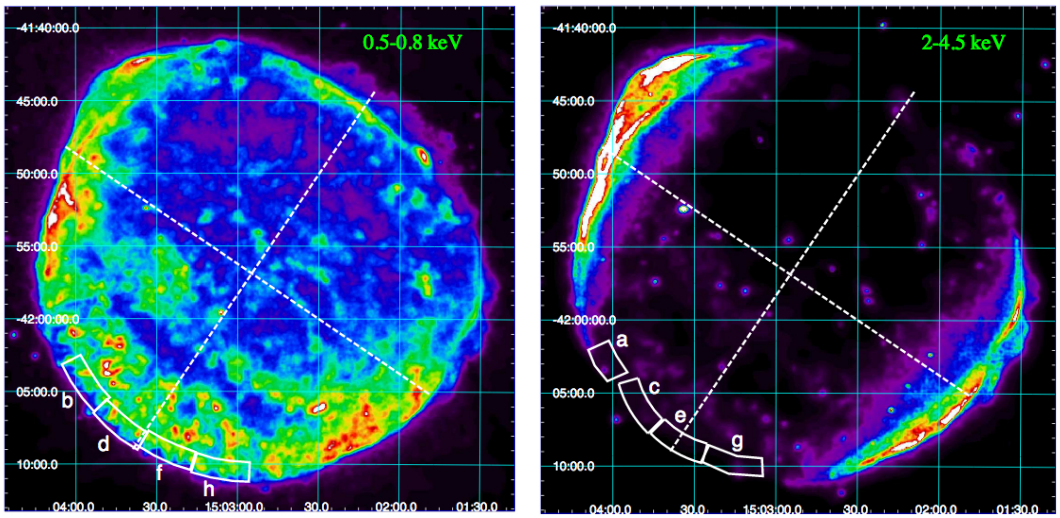

(a) SN 1006 image in the 0.5-0.8 keV energy band.

(b) SN 1006 image in the 2-4.5 keV energy band.

Figure 4.1: Left panel: mosaicked count-rate images (MOS) of SN 1006 in the 0.5-0.8 keV band. North is up and East is to the left. The two dashed lines indicate the symmetry axis of the remnant, marking the center of the synchrotron limbs (northeast and southwest) and of thermal limbs (northwest and southeast). Right panel: same as upper panel in the 2-4.5 keV band. Images obtained from Miceli et al. [2012]

The analysis of six years of *Fermi–LAT* data performed by Acero et al. [2015] has recently provided stringent conditions that help us to constrain the total high-energy nonthermal emission. In particular, the upper limits (at the 95% confidence level) for the flux of the southwestern limb are 1.9×10^{-13} erg cm^{-2} s^{-1} at the median energy of the $3 - 30$ GeV (i. e. at 9.48 GeV) band and 3.5×10^{-13} erg cm^{-2} s-1 at 94.8 GeV.

To synthesize the γ-ray emission we considered three components, namely i) the hadronic emission originating from the impact of high-energy protons with the cloud material; ii) the hadronic emission originating from the impact of high-energy protons with the ambient tenuous medium; and iii) the IC emission.

4.3.1 Hadronic contribution

SN 1006 interacts with ambient interstellar clouds. The northwestern rim expands through a dens ambient medium, and hence the shock is slowed down by the interaction with the dense material. Particle acceleration is not efficient therein, as revealed by the lack of nonthermal emission. On the contrary, the SW limb is a privilege site for the detection of γ-ray hadronic emission. The presence of electrons with energies of a few TeV suggest that hadrons can be effectively accelerated up to ultra relativistic energies at the shock front. For our simulations, in the SW limb we distinguish between three regions: the dense cloud, the shocked part of the dense

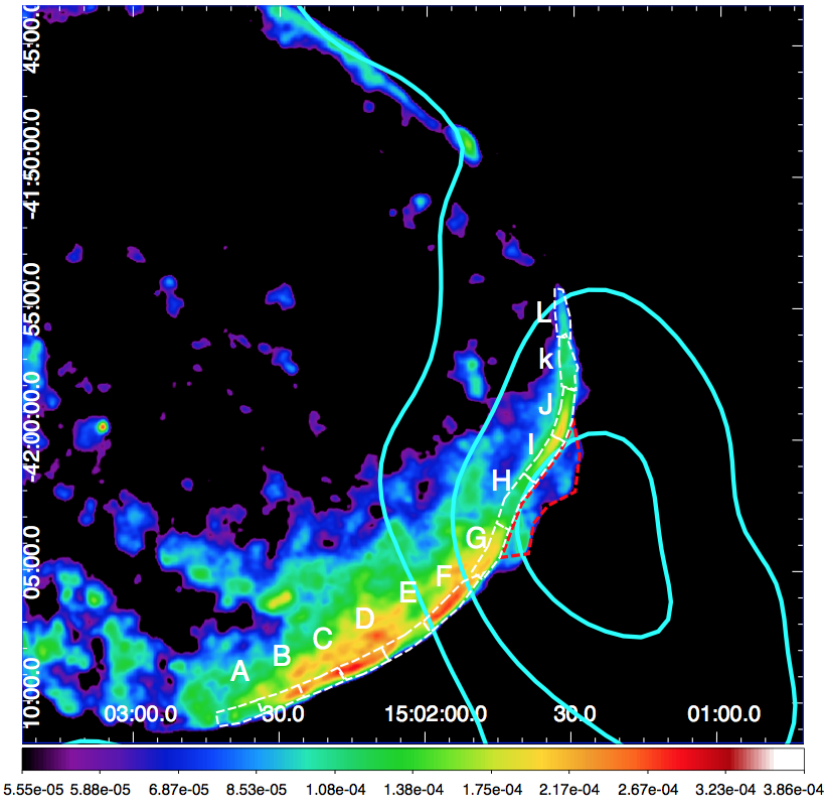

Figure 4.2: EPIC count-rate of the southwestern part of SN 1006 in the 0.3-2 keV band. The contours indicate the column density derived from HI observations, and show the presence of a dense cloud interacting with the remnant.

cloud, and the nonthermal SW limb (see Fig. 4.3).

The detailed description of the targets of proton-proton collisions we developed in Sec. 2.4.4 shows that the only free parameters to derive the hadron emission from SN 1006 are the spectral index of the accelerated particles, which allow us to ascertain some properties of the cosmic rays accelerated at the SW limb of SN 1006, and the ambient density. In particular, we explored what values of the total energy released in the SNR that is turned into protons in the SW limb and the cutoff values of the accelerated protons at the dense cloud and at the shocked cloud are consistent with the observational constraints on the γ-ray emission.

In Miceli et al. [2014] the total proton energy is fixed to 10^{50} erg, corresponding to a 10% of the total explosion energy. Assuming same energy to both limbs, the energy corresponding to the SW limb is $E_{SW} = 5 \times 10^{49}$ erg. In Miceli, M., Orlando, S., Pereira, V. et al. [2016] we present three different scenarios (for a 10% of the total energy turned into hadronic energy, a 5% and a 2%). We want to test if the total proton energy is enough to explain the *H.E.S.S.* data obtains by Acero et al. [2010] or if another contribution is necessary. Fig. 4.4 shows the *H.E.S.S.* map of SN 1006.

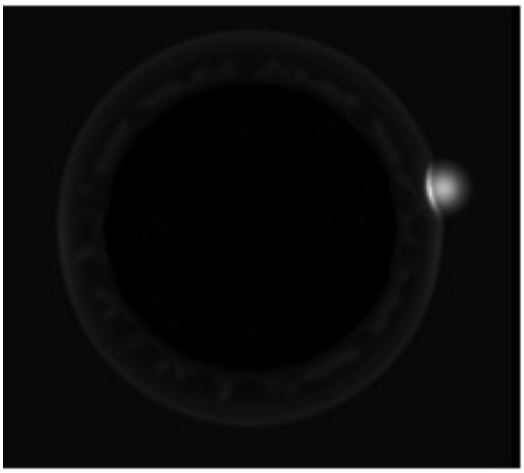

(a) Density profile of the cloud.

(b) Shocked cloud.

(c) SW limb.

Figure 4.3: MHD simulation of the SW limb. The matrixes are not rotated to fit the real SN orientation. The X-axis is perpendicular to the center of the limb. The images correspond to a perpendicular cut in the Z-axis. a) spherical dense cloud; b) shocked part of the cloud; c) nonthermal SW limb.

For the first time, in Miceli, M., Orlando, S., Pereira, V. et al. [2016] are considered two populations of protons: those that impact against the cloud material, and those that impact with the ambient tenuous medium. For each population we can use the expression 2.31, with $\alpha = 2$ and $\beta = 1$, assumed in Miceli, M., Orlando, S., Pereira, V. et al. [2016]. We permit the cutoff energy of the protons accelerated at the shock and transmitted inside the cloud to differ from that of protons accelerated at the remnant forward shock and interacting with the tenuous ambient material. In particular, they correspond to 3 TeV and 150 TeV. The first cutoff must be smaller than the second one given that the acceleration process in the shocked cloud have had less time to accelerate protons than in the shocked medium.Hence, we express

the proton energy distributions as

$$Q(E)_{p,high} = Q_{0,p1} E_p^{-2} \exp(-E_p/3TeV) = Q_{0,p1} J_{p,1}, \tag{4.1}$$

$$Q(E)_{p,low} = Q_{0,p2} E_p^{-2} \exp(-E_p/150TeV) = Q_{0,p2} J_{p,2}. \tag{4.2}$$

$Q_{0,p1,2}$ for each population is computed from the total proton energy, but since this energy is divided between the two populations, we have to calculate the fraction of energy that goes into each one. For this matter, it is necessary to compute how many times the shocked low density region is higher than that of the shocked cloud. In [Miceli, M., Orlando, S., Pereira, V. et al., 2016] is developed a magneto hydrodynamic (MHD) model to reproduce the evolving remnant, which describes the propagation of the SNR of SN 1006 through a magnetized ambient medium. From that simulation, we take the density and temperature images corresponding to the current phase of the SN, and create new images corresponding to the low and high density regions of the SW remnant. In particular, since a shock region is about four times as dense as the ambient density [Landau & Lifshitz, 1959] we select the cells correspondent to the low density shocked region as those cells with a density between 3.4 and 5.8 times the ambient medium density (0.035 cm^{-3}), as derived from the MHD model (Miceli et al. [2012] found that the shock compression ratio increases from 4 up to $\sim$ 6 in regions of the rim that are closer to the nonthermal limbs), and the shocked cloud as those cells with densities higher than 5.8 times the

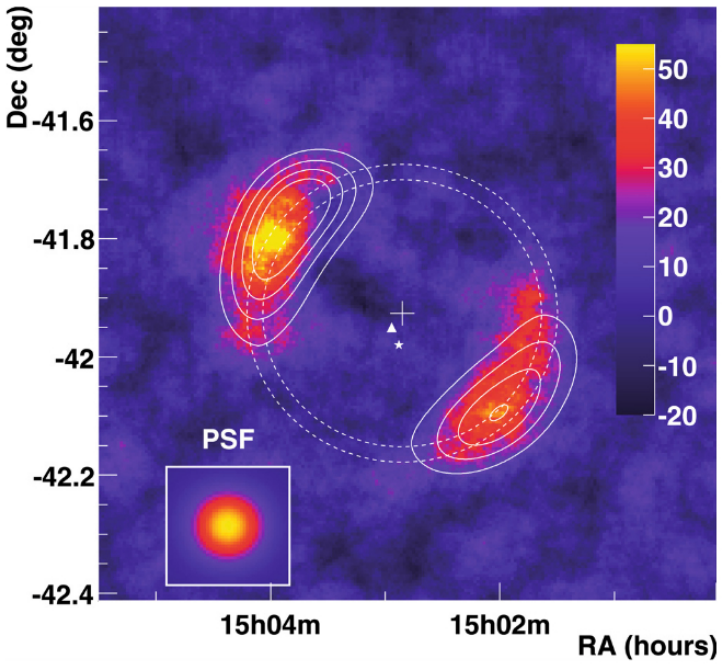

Figure 4.4: *H.E.S.S.* γ-ray image of SN 1006. The white cross indicates the geometrical centre of the SNR. The white contours correspond to a constant X-ray intensity enclosing respectively 80%, 60%, 40% and 20% of the X-ray emission. Image obtained from Acero et al. [2010]

ambient density. Furthermore, we also represent the dependency of the acceleration region as a parametrization of an angular dependent function of the density in the low density shock region, proportional to $\cos^2\theta$, where θ is the angle counted from the center or the SW rim (X axis in the MHD simulations). We obtain a ratio r=7.71, i.e, the acceleration region in the lower density region is $\sim$ 8 times bigger than the acceleration region in the shocked cloud area.

Then, the values of $Q_{0,p1,2}$ can be obtained from

$$E_{SW,p} = \int_{E_{p,min}}^{E_{p,max}} Q_{0,p2} J_{p,2} E_p dE_p + \int_{E_{p,min}}^{E_{p,max}} Q_{0,p1} J_{p,1} E_p dE_p, \tag{4.3}$$

which means that the total hadronic energy is distributed between the two hadronic populations. On the other hand, assuming that the energy is distributed isotropically trough the volume of both acceleration regions, then the second integral must be equal to r^{-1} times the first integral. Hence

$$E_{SW,p} = Q_{0,p2}(r+1)/r \int_{E_{p,min}}^{E_{p,max}} J_{p,2} E_p dE_p. \tag{4.4}$$

Hence, $Q_{0,p1}$ can be obtained from

$$Q_{0,p1} = \frac{Q_{0,p2} \int_{E_{p,min}}^{E_{p,max}} J_{p,2} E_p dE_p}{r \times \int_{E_{p,min}}^{E_{p,max}} J_{p,1} E_p dE_p}. \tag{4.5}$$

Finally, to compute the hadronic luminosity, we follow the procedure described in Sec. 2.4.4, and the results are shown in Fig. 4.5. *Fermi*-LAT upper limits (at the 95% confidence level) for the flux of the southwestern limb from Acero et al. [2015] and the γ-ray spectrum observed with *HESS* for the same limb from Acero et al. [2010] are also included.

We first explore the case with $E_{p,SW} = 5 \times 10^{49}$ erg (i. e. a total hadronic energy $E_{p,tot} = 10^{50}$ erg in the whole remnant, corresponding to 10% of the explosion energy), $E_{cut,1,p} = 3$ TeV, and $E_{cut,2,p}$ =150 TeV [Miceli et al., 2014]. We verified that, with this set of parameters, the resulting γ-ray emission in the GeV band is over the $Fermi - LAT$ upper limits and is not still able to explain the $H.E.S.S.$ data. There is no reason to believe that the cosmic-ray acceleration efficiency is constant with time. Particles could be accelerated to the highest energies at the very beginning of the SNR evolution and the acceleration efficiency could decrease significantly in the following years [Fernandez et al., 2013]. Hence, we then explored different proton spectra, by reducing the total hadronic energy. Panel (b) of Fig. 4.5 shows the γ-ray emission obtained for $E_{p,SW} = 2.5 \times 10^{49}$ erg (i. e., hadrons have drained $\sim$ 5% of the explosion energy) and same proton cutoff energies; finally, panel (c) of Fig. 4.5 shows the γ-ray emission for $E_{p,SW} = 10^{49}$ erg, which in this case, presents a γ-ray flux well below the $Fermi - LAT$ upper limits.

Our results show that the hadronic emission is not enough to explain the *HESS* data obtained by Acero et al. [2010], and hence a leptonic contribution is needed: the IC. This result is very interesting since we reject the pure hadronic scenario

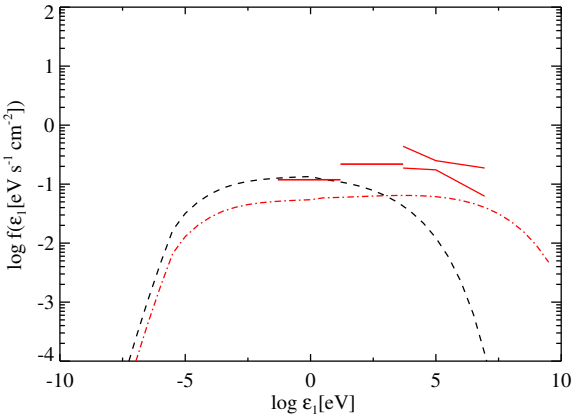

(a) Total hadronic energy of 5×10^{49} erg.

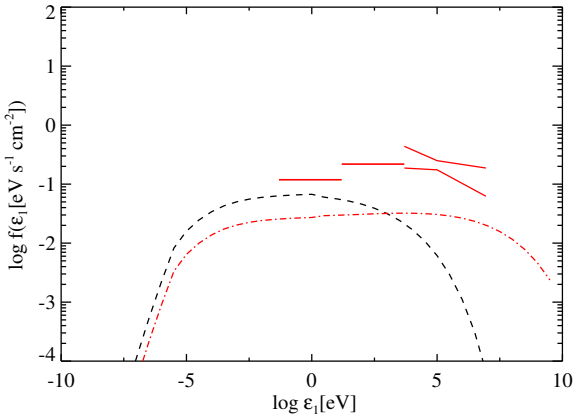

(b) Total hadronic energy of 2.5×10^{49} erg.

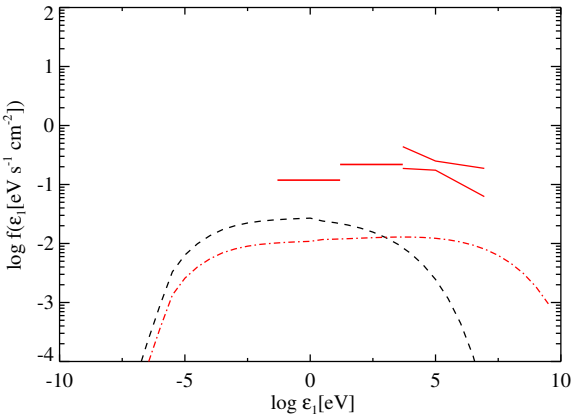

(c) Total hadronic energy of 10^{49} erg.

Figure 4.5: p-p inelastic collision emission from the two populations of protons for the three different total hadronic energies from Miceli, M., Orlando, S., Pereira, V. et al. [2016]. The dashed line describes the hadronic emission from the shocked cloud, and the dashed-dotted line the hadronic emission from the shocked ambient medium. *Fermi* limits of detection from [Acero et al., 2015] and the *H.E.S.S* data are included.

in the TeV band. A mixed leptonic-hadronic scenario in needed, including the fact that the leptonic emission should be higher than the hadronic emission in that band. Furthermore, we discard some of the different scenarios proposed in the literature to explain the TeV emission, not only because the total proton energy prevents the hadronic emission to reach the observed fluxed, but also because the *Fermi*-Lat upper limits show that if the hadron emission would be the responsible of the TeV band data (H.E.S.S. data), it should have also been detected in the GeV band, and it does not happen.

Hence, we discard the possibility of being the emission of the π^0 decay the only responsible of the observed γ-rays. Acero et al. [2010] and Berezhko et al. [2012] test the possibility of a pure hadronic model, but greater energies were needed and also obtained fluxes in the GeV band greater than the upper limits related. We

also have to point out that if a leptonic contribution is needed, the sum of the hadronic and leptonic contributions would exceed the *Fermi*-LAT upper limits if we still consider that about a total of a 10% of the supernova explosion energy is dedicated to the acceleration of particles, and hence we will also have to accept that the proton energy has been reduced with time.

Since radiative losses are negligible for protons, the derived luminosity spectrum is generated by the accelerated protons, represented by the injection functions. The total proton energy remaining in the acceleration region is revealed as a very important value to reject the possibility of π^0 decay emission to be the unique responsible of the *H.E.S.S.* observations, and to explain the non detection of emission in the GeV band. On the other, hand, this is the first time where two populations of protons are considered, since a second population arises from the interaction of the SNR with a dense cloud [Miceli, M., Orlando, S., Pereira, V. et al., 2016].

4.3.2 Leptonic contribution

Zirakashvili & Aharonian [2007] found analytical solutions for energy spectra of electrons that are accelerated in the shock-waves of SNRs. They presented asymptotic solutions for the high-energy asymptotic branch of the distribution of electrons. However, they always consider that synchrotron losses dominate over other electron loses; to obtain the analytic solution to a broader range, they use the asymptotic solutions for very low and very high electron energies, using numerical calculations at intermediate energies. Their solutions have been widely used to parametrize the electron emission through synchrotron and IC processes. On the other hand, Reynolds & Keohane [1999] modeled the nonthermal limbs as synchrotron radiation from a power-law distribution with an exponential cutoff (SCRUT model). This cutoff is selected to fit the X-ray data, which corresponds to the tail of synchrotron emission. In particular, the electron energy distribution for each case is given by

$$N(E) \propto E^{-\alpha}[1 + 0.523(E/E_0)^{2.25}]^2 \exp[-(E/E_0)^2] \tag{4.6}$$

$$N(E) \propto E^{-\alpha} \exp[-(E/E_{cut})] \tag{4.7}$$

Here, we want to show that the model we have presented in Chapter 2 is also valid for SNRs. Furthermore, we showed that many factors affect the shape of the electron distribution, and such influences can be inferred from the consideration of all the cooling time rates, that also produce a change in the slope of the electron energy distribution (see Sec. 2.3). In addition, although it is possible that synchrotron losses domain over other processes, the presence of dust or heated dust in the shock region can lead to intense IC losses, which in some cases can dominate over those produced by synchrotron cooling, as we saw in the case of bow shocks produced by runaway stars. Hence, we will follow the same scheme presented in Chapter 3, studying the spectra synthesize under different situations and the changes in the electron spectrum (and thus in the leptonic emission).

According to our model, the synchrotron and IC losses influence each other. We use the radio and X-ray emission to fit the synchrotron emissions, and this emission

influences the IC emission, fixing its value. Hence, we do not process the leptonic processes separately, but we study their effects on the other process.

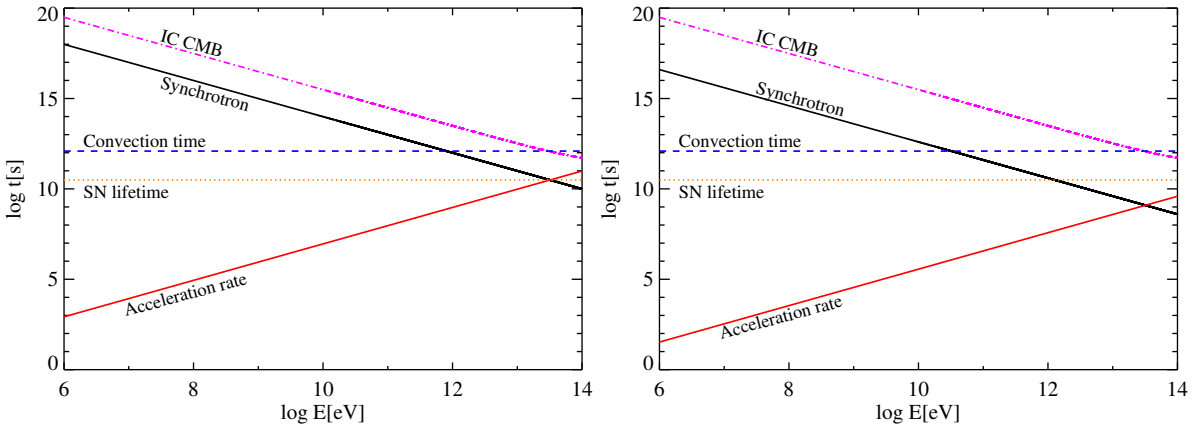

(a) Cooling time rates for B=20 μG.

(b) Cooling time rates for B=100 μG.

Figure 4.6: Cooling time rates for two different values of the magnetic field: a) 20 μG; b) 100 μG.

First, we only consider the IC originated from the scattering of CMB photons. In our model, the magnetic field has a great importance in the electron energy distribution, as we show in Fig. 4.6, where we can compare the differences in the time rates for different values of the magnetic field (for 20 and 100 μG).

Considering only the IC of the CMB photons, the synchrotron losses are much more important than the IC losses, and this difference is even larger for higher values of the magnetic field strength. Furthermore, low values of B do not allow electrons of none energy to cool down completely since the supernova lifetime is shorter than the time needed by electrons of all energies to cool down completely. Then, the electron energy distribution is the injection function of electrons derived from the Fermi first order mechanism. However, for higher values of the magnetic field, the highest energy electrons have time to cool completely, producing a change in the slope in the electron energy distribution, as seen in Fig. 2.8. Clearly, in this case synchrotron cooling is the dominant cooling process.

In Table 4.1 we present the luminosity distributions for different strengths of the magnetic field and for different electron injection indexes. Radio [Reynolds, 1996], X-rays [Bamba et al., 2008] and *H.E.S.S.* [Acero et al., 2010] data are shown, as well as the *Fermi* detection limits. For very low energies, numerical constrains (the energy step chosen for the simulations) produce a small jump in the synchrotron spectrum; longer numerical simulations would correct them, but the global result would be the same, thus we prioritize the computational time. From the synthesized spectra, we conclude that low magnetic fields allow IC emission to explain the nonthermal GeV and gamma emission, but high magnetic field values reduce de efficiency of the IC scattering. Only values of 10-15 μG can explain the *Fermi* and *H.E.S.S* data. This conclusion is of the utmost importance since our model predicts that the IC of the CMB photons is not compatible with high values of the magnetic

field to explain the observations at very high energies. Hence, if we consider that only the CMB photons are present in the shock region, only low magnetic fields can be considered to explain the observations at TeV energies.

It is also important to note that the influence of the magnetic field on the synchrotron losses is not only related to the efficiency of the process, but also to the shape of the electron energy distributions.

The change in the slope of the electron energy distribution originated by those electrons that can cool completely, as seen in Fig. 4.6 *b* also affects the spectrum, which shows that the peaks of the synchrotron and IC luminosities are shifted to the left.

4.3.3 Mixed model: leptonic and hadronic contributions

The synchrotron emission is responsible of the X-ray emission detected in the SW limb of the SN 1006. The IC emission produces high-energy photons, particularly in the GeV and TeV bands. However, as we explained in section 4.3.1, there exist two populations of hadrons that also contribute to the high-energy emission. Hence, we mixed both contributions to synthesize the complete spectrum, as shown In Fig. 4.7.

The spectrum can explain the observed *H.E.S.S.* spectrum at TeV energies and is also consistent with the newest $Fermi - LAT$ upper limits, being at the edge of detectability in the 3−30 GeV band.

However, only for 10 μG the observational data can be explain. The IC dominates all the high-energy range for a magnetic field of 10 μG, being the hadronic emission only significant in the 3-30 GeV band. The total current hadronic energy to fit the data results in 10 ^{49} erg.

For 15 μG, even considering a total hadronic energy of 2.5 $\times$ 10^{49} erg, the *H.E.S.S* data can not be explained; higher hadronic energy can not compensate the IC emission decrease since it would exceed the *Fermi* detection limit. At this point is important to note that due to time limits for numerical simulations and to the number of free parameters, we only run simulations for discrete set of parameters (not continuous). Hence, we approach to the values that best explain the data, being conscious that intermediate values of the parameters chosen for the simulations would obtain better approaches. Nevertheless, we can reach the same conclusions optimizing the computational time.

In agreement with our results, Acero et al. [2010] showed that the TeV observations of SN 1006 obtained with the HESS telescope cannot be uniquely attributed to hadron emission, and showed that a mixed scenario that includes leptonic and hadronic components also provides a good fit to the γ-ray data; furthermore, they pointed out that according to the model by Berezhko et al. [2012] the hadronic and leptonic components in the γ-ray emissions are of comparable strength. However, we show that the recent *Fermi* detection limits in the GeV band from Acero et al. [2015] reduce the possible hadronic contribution, revealing the leptonic emission as the dominant process.

For Petruk et al. [2009] the data are consistent with a pure leptonic model, in

Table 4.1

	B [μG]	
α	10	15
2.2	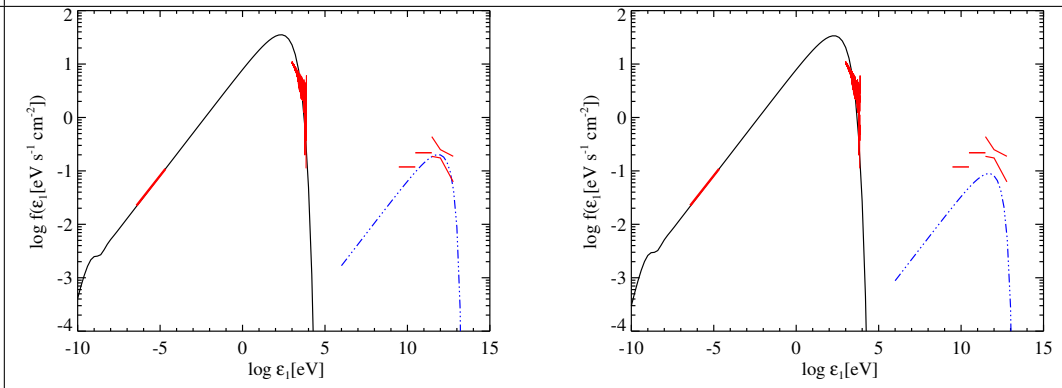	
2.3	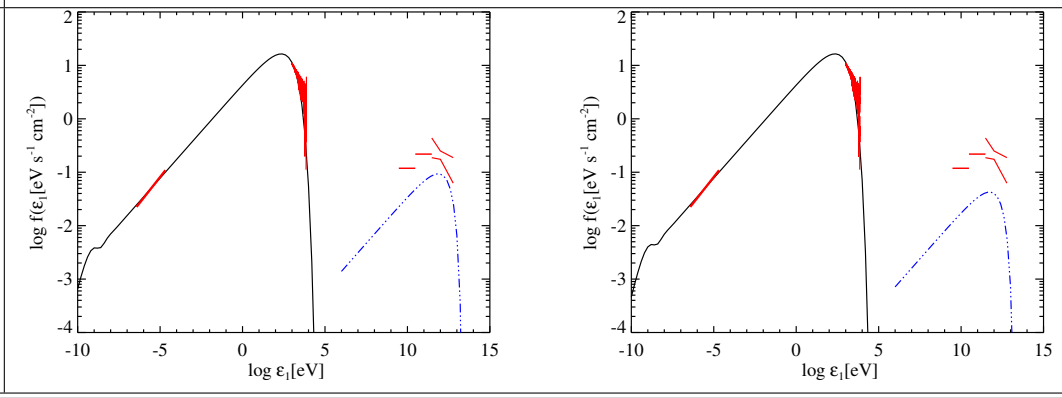	
	B [μG]	
α	30	100
2.2	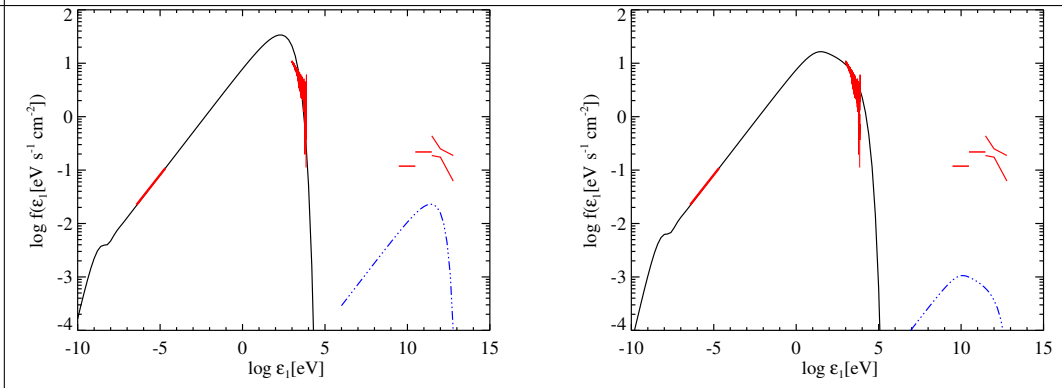	
2.3	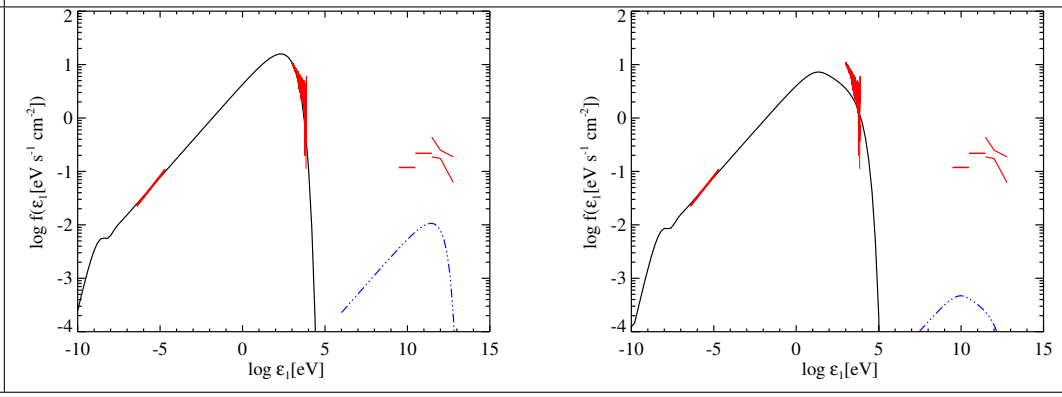	

Table 4.1: Simulations of SN1006 SW limb considering only the CMB IC scattering.

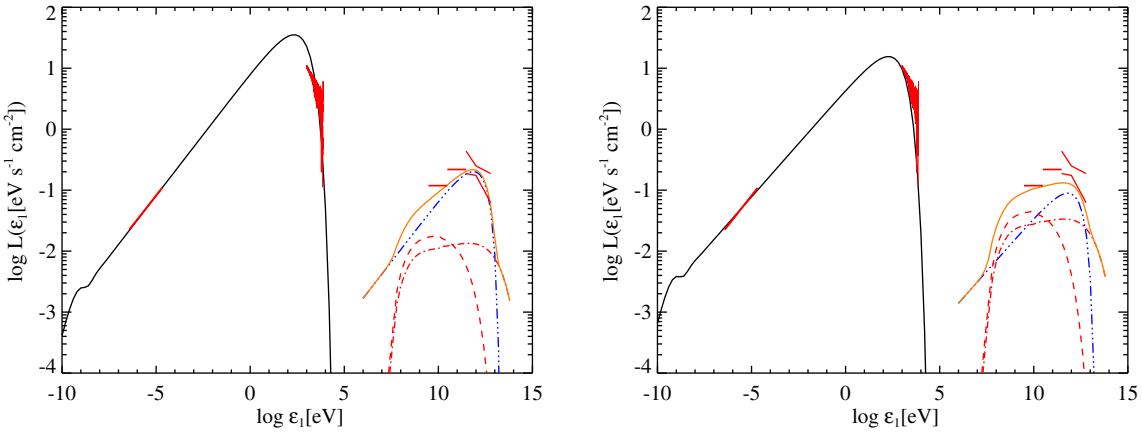

(a) B=10 μG, α=2.3, hadronic energy of 10^{49} erg. (b) B=15 μG, α=2.3, hadronic energy of 2.5×10^{49} erg.

Figure 4.7: Best fit spectra considering only the IC of the CMB photons and a mixed model of leptonic and hadronic contributions for a) 10 μG and b) 15 μG.

agreement with the morphology of the γ-ray emission of SN 1006. The basic model of hadronic γ-ray production requires particles accelerated up to a few TeV energies and a target of sufficient density.

Therefore, the tenuous environment around SN 1006 ($<$0.05 cm^{-3}) does not favor the proton-proton interactions that trigger hadronic emission. However, we have considered two populations of protons, one corresponding to the low density shock regions, and one corresponding to the shocked cloud which interacts with the southwestern limb. The IC is still the dominant process, but the hadron emission is not negligible. According to our results, the emission in the GeV band, if present, will be detectable within a few more years, when the *Fermi* detection limits will be decreased. This would help to add new constraints that would lead to more accurate values of the total hadronic energy available in the current remnant.

The magnetic field we obtain with our model, of $\sim$ 10 μG, is low compared to the magnetic field obtained by other authors and models. For example, [Parizot et al., 2006] derive a magnetic field of $\sim$ 100 μG, and Berezhko et al. [2012] fitted the multiwavelength spectrum with 150 μG, although overestimated the GeV emission. Acero et al. [2010] used a magnetic field strength of $B = 30$ μG to fit the observational data with a pure leptonic model and $B = 45$ μG with a mixed model.

Complementary photon field sources.

We now study the possibility of coexistence of another more energetic photon field (such us the emission of a cold dust) with the CMB photons. From Fig. 4.6 the decrease of the IC observed in Table 4.1 and Fig. 4.7 can be explained. The higher the magnetic field, the more efficient the synchrotron mechanism in cooling particles (the acceleration of charged particles following an helical trajectory is higher and so is the fraction of the particle energy emitted) in accordance with Eq. 2.11, and also the synchrotron emission is enhanced (Eq. 2.35). However, the synchrotron

emission depends on the magnetic field strength. Hence, the strongest the magnetic field, the more important are the synchrotron losses and the less important the IC cooling. This result would explain that for stronger magnetic fields the IC decreases. Then, if only the IC of the CMB photons is considered, according to our

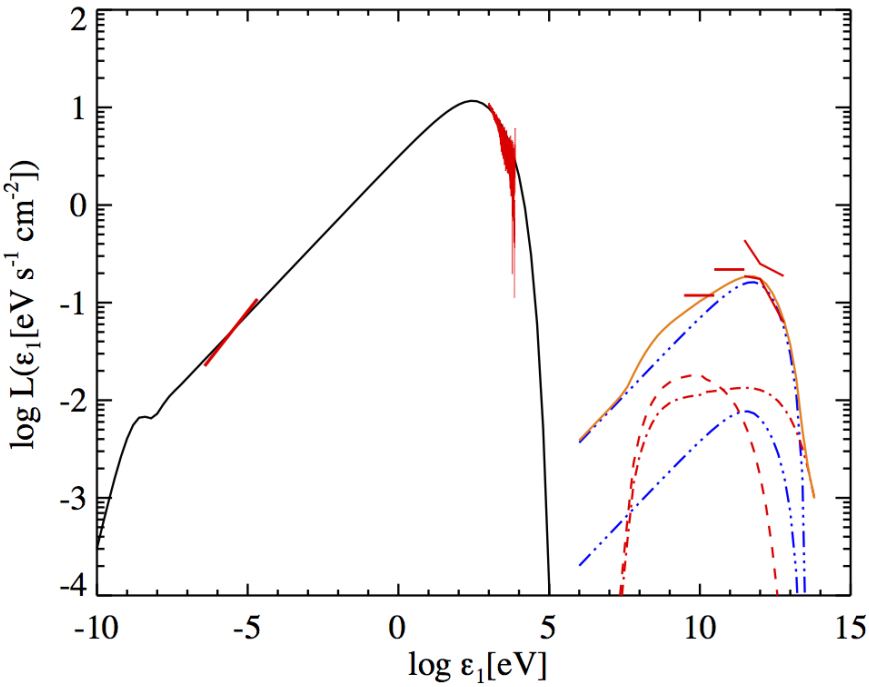

Figure 4.8: Synthetic inverse Compton monochromatic emission of the southwestern limb of SN 1006 at 3 GeV (in red) and 3 TeV (in blue). The contours of the X-ray emission are superimposed in white.

simulations only a very low magnetic field could explain the X-ray and the γ-ray observations as a contribution of both leptonic an hadronic processes. This suggests that, if there is a source of photons other than the CMB, the IC losses would be more important compare to the synchrotron losses and hence stronger magnetic fields. This is because if synchrotron losses are much more relevant than IC losses, they carry away most of the energy, leaving photons scattered by electrons without enough energy. However, if another more energetic source of photons exists, they would need less energy to be scattered up to very high energies, and hence being able to coexist with powerful magnetic fields.

We observe that as the magnetic field increases (see Table 4.1), the IC maximum is shifted to the left. For values higher than 30 μG the IC peaks at the GeV band and not at the TeV band. Since the IC emission must be dominant in the TeV band to explain the *H.E.S.S* data (if the hadronic emission were dominant in the TeV band it would exceed the *Fermi* limits), we can not consider very strong magnetic field values. In Fig. 4.8 we plot the synthesize spectrum for 30 μG, considering a photon field at 6 K degree. Although the IC of the CMB photons is very low, in this case it would be compensated by a hotter photon field. Again, the IC is

responsible for most of the high-energy emission, and the hadronic contributions is only relevant in the GeV band.

This new source of photons has never been observed in that region by any telescope. However, the expanding ejecta of young SNRs are expected to be important factories of cold dust, whose thermal infrared emission may also contribute to the total IC emission.

Chapter 5

Summary and conclusions

5.1 Summary

In this PhD thesis we have studied the nonthermal emission from bow shocks formed by runaway stars and from the supernova remnant SN 1006. In particular, we have developed a nonthermal model starting from previous models from other authors, with the aim of generalizing our model to any kind of shock with a stellar origin. Using observational data at different wavelengths, we have tried to constrain the different physical parameters taking part in the high-energy photon emission processes.

We have presented the physics of different nonthermal emission processes (Chapter 2), namely synchrotron, Inverse Compton (IC) and proton-proton inelastic collisions; we have also studied the characteristics of the bow shocks formed by runaway stars (Chapter 3) and the conditions that favor the acceleration of charged particles. In particular, we studied the bow shock formed by the stars AE Aur, BD+43 3654 and Betelgeuse. Then, we applied our model to the scenario observed towards the south-west limb of the supernova remnant SN 1006. The main aspects of this work can be summarized as follows:

1. Firstly, we study the cooling processes that are able to produce observable nonthermal photons. As a basis, we use the models of Ginzburg & Syrovatskii [1964], Berezinskii et al. [1990], Kelner et al. [2006], Zirakashvili & Aharonian [2007], del Valle & Romero [2012].

   a) The Fermi first-order acceleration mechanism is responsible for the acceleration of charged particles. Charged particles undergoing this acceleration follow a power-law distribution $Q(E) \propto E^{-\alpha}$, which is the particle injection function. In shock acceleration regions, the time a particle needs to be accelerated up to an energy E depends on the magnetic field B as $t_{acc} \propto E/B$.

   b) Synchrotron and Inverse Compton (IC) cooling processes are revealed as the most relevant leptonic processes. All cooling processes are considered together and influence each other, which is an important improvement with

respect to previous models; in particular, it has never been considered before in supernovae emission models, but has very important effects on the synthesized spectra. The time an electron needs to cool down completely by synchrotron processes is proportional to $B^{-2}E^{-1}$: high-energy electrons cool down faster. The highest magnetic field, the more efficient the synchrotron process in cooling particles. IC can easily produce X-ray photons from cold photon fields: namely, low-energy photons from cold material emissions, at a few dozens of Kelvin degrees, can be scattered up to X-ray wavelengths by electrons of at least $\sim$ 50 MeV, as shown in Fig 2.3. We consider different sources of photons, such as the Cosmic Microwave Background (CMB), dust photons from the heated shock regions, and the photons from stars close to the acceleration regions.

c) Proton-proton inelastic collisions is the most relevant hadronic cooling process.

d) The maximum energy electrons can reach is given by the energy where the acceleration rate and the most efficient cooling processes are equal.

e) The particle energy distribution accounts for the following scenarios: the different cooling processes the particles may undergo, the possibility of the particles to be convected away from the acceleration region before they cool down, and the lifetime of the shock region. When a range of particles have time to cool down completely and other particles do not, a change in the slope of the particle energy distribution arises, as seen in Fig 2.8. If none particles cool completely, the electron energy distribution is the electron injection function, which is the power-law distribution of the particles undergoing the Fermi first-order mechanism.

2. Second, we study the possibility of bow shocks formed by runaway stars to emit nonthermal emission. Then we apply our model to the bow shocks formed by the stars AE Aurigae and BD+43 3654, and to a supergiant star during the transition phase from blue to red supergiant. The results were published in Pereira et al. [2016].

a) Runaway stars are stellar objects that were expelled from their place of origin by dynamical processes. From the interaction between the interstellar medium and the stellar wind of this stars results a bow shock, which is the heading front shock propagating in the same direction than the stellar wind at a velocity similar to the stellar speed, and the reverse shock, moving opposite to the stellar wind and at its same velocity. The bow shock is formed at a distance where the stellar wind and the interstellar medium (ISM) pressures equalize, known as the standoff radius, $R_0 = (\dot{M}V_w/(4\pi\rho_{ISM}V_\star^2))$.

b) The free parameters of the model to synthesize the bow shock nonthermal spectrum are the following:

i) The factor χ, which defines the relation between the magnetic and the kinetic energy densities, as defined in Sec. 3.2 .

ii) The fraction of the total energy available in the acceleration region is given by q_{rel}.

iii) The electron injection index, α, as defined in Secs. 2.1 and 2.3.

iv) The width of the acceleration region, given as a fraction, δ, of the standoff radius, as explained in section 3.2

c) To obtain the nonthermal spectra of the different bow shocks, we first numerically compute the maximum electron energy by calculating the cooling time rates of the different nonthermal cooling processes and the acceleration rate as explained in Sec. 2.2. Then, we compute the particle energy distribution (see Sec. 2.3). Finally, we computationally obtain the synthesized spectrum as derived in section 2.4.

d) To constrain the bow shock physical parameters of the star AE Aurigae, we use the X-ray data from López-Santiago et al. [2012] and the *Fermi* limits from Schulz et al. [2014].

e) Then, we try to explain the X-ray non-detection from the star BD+43 3654. For the simulations, we use the radio and thermal infrared data obtained from the bow shock region formed by this star, the *XMM-Newton* detection limits for 100 ks and the *Fermi* detection limits for this bowshock.

f) We extend the study of the nonthermal emission from bow shocks to the bow shocks formed by supergiant stars during the transition phase from blue to red supergiant. We use the hydrodynamic simulations for the star Betelgeuse from Mackey et al. [2012] to compute the synthetic nonthermal from the bow shock formed by this star.

g) Finally, we produce a grid of nonthermal spectra for different values of the ISM density, the velocity of the star, the stellar mass loss rate, the terminal wind velocity and the electron injection index, to qualitatively study the possibility of nonthermal emission (and detection) from other bow shocks detected in infrared energies and listed in Peri et al. [2012].

3. We extend our model to the study of the nonthermal emission from supernova remnants, since the nonthermal processes that take place in this objets are in common with those in the bow shocks from runaway stars, and as supernova remnants are efficient particles acceleration. In particular, we apply our model to the southwestern (SW) limb of the supernova remnant SN 1006.

a) First, we try to explain the very high-energy emission from the SW limb of the SN 1006 by the emission from hadronic processes. We constrain the emission from the total proton energy, the MHD simulations from Orlando et al. [2012], the *Fermi* detection limits from Acero et al. [2015] and the *H.E.S.S.* from Acero et al. [2010]. For the interaction of this limb with a dense cloud, we include two populations of protons, one for those interacting with the tenuous ISM medium, and one for those that impact against the dense cloud material. From Miceli et al. [2014] the total energy corresponding to the SW is 5×10^{49} erg; we present three different scenarios: 10%, 5% and 2% of

the total energy turned into hadronic energy. The results were presented in Miceli, M., Orlando, S., Pereira, V. et al. [2016].

b) Second, we try to explain the emission from the SW limb by leptonic processes. The main nonthermal cooling processes are the synchrotron and the IC of the CMB photons. Both processes are studied together and influence each other, as shown in Fig. 4.6: the radio [Reynolds, 1996] and X-ray [Bamba et al., 2008] data constrain the shape and intensity of the synchrotron emission; the *Fermi* and *H.E.S.S.* data constrain the IC emission and the magnetic field strength.

c) Third, we study the hadronic and leptonic processes together to try to obtain a better approach to the observational data of the SW limb. In this case, the IC of the CMB photons and the hadronic emission contribute to explain the *H.E.S.S.* observations, while the *Fermi* data is used to constrain the total hadronic energy, as shown in Fig. 4.7. Furthermore, we also compare our results with previous studies.

d) Finally, we also try to explain the observational data including the possibility of other cold photon fields in the shock region coexisting with the CMB photons. This would permit the IC to be more efficient and hence other values of the magnetic field could be considered.

5.2 Conclusions

Main conclusions of this Ph.D. Thesis are:

- The cooling time rates define which of the different nonthermal cooling processes is most relevant according to the shock parameters. Together with the acceleration rate, they determine the electron and proton energy distributions. The study of the shock parameters can reveal a change in the slope in the energy distribution that is strongly reflected in the emitted spectra. Furthermore, nonthermal processes are not independent, but they influence each other. To synthesize the spectra, all processes should be taken into account (they should definitely not be processed independently). Our model is applied to different types of stellar objects to investigate their capacity to inject nonthermal high-energy photons to the interstellar medium.

- A combination of low electron injection indexes, high mass loss rates and high terminal wind velocities favor the X-ray photon production in bow shocks. The density and the velocity of the star are also major parameters to determine the formation of a bow shock.

- The synchrotron emission is responsible for the radio emission but the Inverse Compton (IC) of dust photons is the most important mechanism for the X-ray photon production. The IC of stellar photons is less intense than the IC of dust photons. The relativistic Bremsstrahlung is very weak.

- The IC of the infrared photons present in the bow shock formed by AE Aur is the most important cooling process. The IC of the dust photons explains the observational data at X-ray wavelengths, and is also consistent with the *Fermi* detection limits for this star. The electron distribution can be modeled with an electron injection index of $\alpha = 2$, and the spectrum can be reproduced with a shock width of 0.3 times the standoff radius, considering that 15% of the total energy available in the acceleration region is turned into relativistic particles, and that the magnetic energy is 20% of the kinetic energy of the wind.

- For the star BD+43 3654, our model explains successfully the radio (originated by synchrotron and the thermal emission of the heated dust) and infrared observational data available. Furthermore, it is consistent with the X-ray and *Fermi* non-detections for this star. We successfully explain the detection and non-detection at different wavelengths. The observational data is consistent with an electron injection index of $\alpha = 2.1$, a magnetic energy density similar to the kinetic energy density, and with 10% of the energy available in the acceleration region turned into relativistic particles.

- According to our model, nonthermal emission from bow shocks formed by runaway stars conform a new source of high-energy photons injected to the ISM. However, their X-ray emission is not very strong (a maximum luminosity

of about 10^{30} erg s^{-1} in the 0.3-10 keV) and hence can only be detected in our neighbourhood, mainly at distances under 1 kpc. With the current generation of X-ray telescope. We expect a major step forward in detections of these sources with the forthcoming Athena X-ray telescope.

- Supergiant stars during the transition from blue to red supergiant form bow shocks that emit nonthermal high-energy emission. However, the emission is fainter than that emitted by bow shocks formed by runaway stars.

- We consider two populations of protons in the Southwestern limb of the supernova remnant SN 1006, one for the interacting protons with a dense cloud, and another for those interacting with the tenuous ambient medium. However, we discard the possibility of the hadronic emission to be the unique responsible for the total *H.E.S.S.* emission according to the new *Fermi* limits in the GeV band, which constrain the total hadronic energy to be under 5×10^{49} erg.

- A contribution of hadronic and leptonic processes explain the observational data at all wavelengths. The synchrotron emission is the most efficient cooling process and responsible for the radio X-ray emission. IC of the cosmic microwave background photons emission is revealed as the most relevant nonthermal process that explains the high-energy emission at GeV and TeV, with a small contribution of hadronic emission. The main parameters that explain the observations are a magnetic field strength $B = 10$ μG, electron injection index $\alpha_e = 2.3$, proton injection index $\alpha_p = 2$ and a total current hadronic energy of 10^{49} erg.

- The observational data is also compatible with the coexistence of another cold photon field and higher values of the magnetic field. For a photon field at 6 K, a magnetic field strength of $B = 30\mu$G can also explain the observational data.

Appendix A

Star	l	w	R	l	w	R	n_{ISM}	Comments
	[arcmin]			[pc]			[cm^{-3}]	
HIP 2036	4.5	1.3	1	0.99	0.29	0.22	130	Emission-line star
HIP 2599	9	1.3	3	3.81	0.55	1.27	0.4	Emission-line star
HIP 11891	4	1	1	1.05	0.26	0.26	3	Star in cluster
HIP 16518	4	1	0.7	0.76	0.19	0.13	0.2	Variable star
HIP 17358	3	1	1	0.13	0.04	0.04	600	Variable star
HIP 22783	33	10	10	15.43	4.67	4.67	0.02	Emission-line star
HIP 24575	2	0.5	0.4	0.32	0.08	0.06	3	Double or multiple star
HIP 25923	4	1	1.5	1.05	0.26	0.39	1	Variable star
HIP 26397	3	1	1	0.31	0.10	0.10	2	Star
HIP 28881	9	1.5	3	5.54	0.92	1.85	0.3	Double or multiple star
HIP 29276	5	2	2	0.58	0.23	0.23	0.003	Eclipsing binary of beta Lyr type
HIP 31766	5	2	2	2.06	0.82	0.82	0.03	Double or multiple star
HIP 32067	13	2.5	3	8.01	1.54	1.85	0.1	Emission-line star
HIP 34536	12	3	4	4.51	1.13	1.50	0.01	HII (ionized) region
HIP 38430	2	0.5	0.5	0.52	0.13	0.13	60	Emission-line star
HIP 62322	4	1.2	1	0.17	0.05	0.04	0.02	Double or multiple star
HIP 72510	4.5	0.8	1.5	0.46	0.08	0.15	0.2	Emission-line star
HIP 75095	1.5	0.5	0.5	0.35	0.12	0.12	40	Star
HIP 77391	4	1	1	0.93	0.23	0.23	30	Star
HIP 78401	25	2	6	1.63	0.13	0.39	2	Double or multiple star
HIP 81377	22	2	5	1.42	0.13	0.32	1	Be star
HIP 82171	2	0.5	0.7	0.49	0.12	0.17	1	Star
HIP 88652	6	1	1.5	1.13	0.19	0.28	2	Star
HIP 92865	11	1	3	1.12	0.10	0.31	0.003	Eclipsing binary of beta Lyr type
HIP 97796	13	2.5	6	8.32	1.60	3.84	0.02	Spectroscopic binary
HIP 101186	19	2.5	4	8.21	1.08	1.73	0.1	Emission-line star
BD+43 3654	12	3	3.5	5.06	1.27	1.48	0.2	Star
HIP 114990	3.5	0.75	1.5	1.43	0.31	0.61	0.05	Star

Figure 1: Stellar bow shock parameters for the selected stars studied in Peri et al. [2012]: coordinates and ambient medium densities.

Star	Group	l [°]	b [°]	Spectral type	d [pc]	v_∞ [km s^{-1}]	$\dot{M} \times 10^6$ [$M_\odot$ yr^{-1}]	v_{tg} [km s^{-1}]	v_r [km s^{-1}]
HIP 2036	2	120.9137	+09.0357	O9.5III+B1V	757 ± 161[a]	[1200]	0.48	15.2	−5
HIP 2599	1, 2	120.8361	+00.1351	B1 Iae	1457 ± 300[a]	1105	0.12	26.2	−2.3
HIP 11891	2	134.7692	+01.0144	O5 V((f))	(900)	2810	1.10	11.9	−48
HIP 16518	2	156.3159	−16.7535	B1 V	(650)	[500]	0.006	47.3	25
HIP 17358	1	150.2834	−05.7684	B5 III	(150)	[500]	<0.001	[35]	4
HIP 22783	1	144.0656	+14.0424	O9.5 Ia	1607 ± 275[a]	1590	0.25	[52]	6.1
HIP 24575	2	172.0813	−02.2592	O9.5 V	548 ± 68[a]	[1200]	0.1	140.0	59.1
HIP 25923	2	210.4356	−20.9830	B0 V	(900)	[1000]	0.06	16.8	17.4
HIP 26397	2	174.0618	+01.5808	B0.5 V	(350)	[750]	0.014	11.9	−19
HIP 28881	1	164.9727	+12.8935	O8 Vn	1500[b]	2070	0.03	[17]	5
HIP 29276	1, 2	263.3029	−27.6837	B1/2 III	(400)	[600]	<0.001	9.2	30.6
HIP 31766	2	210.0349	−02.1105	O9.7 Ib	1414 ± 28[a]	1590	1.07	6.7	58.4
HIP 32067	1,2	206.2096	+00.7982	O5.5V(((f))+...	2117 ± 367[a]	2960	0.13	23.4	31
HIP 34536	1, 2	224.1685	−00.7784	O6.5V(((f))+...	1293 ± 206[a]	2456	0.19	14.3	58
HIP 38430	1	243.1553	+00.3630	O6Vn+...	(900)	[2570]	0.7	[13]	28
HIP 62322	2	302.4492	−05.2412	B2.5 V	(150)	[300]	0.006	4.5	42
HIP 72510	1, 2	318.7681	+02.7685	O6.5III(n)(f)	(350)	[2545]	0.27	7.4	−74
HIP 75095	2	322.6802	+00.9060	B1Iab/Ib	(800)	[1065]	0.14	28.6	4
HIP 77391	1	330.4212	+04.5928	O9 I	(800)	[1990]	0.25	[19]	15
HIP 78401	1	350.0969	+22.4904	B0.2 IVe	224 ± 24[a]	[1100]	0.14	[38]	−7
HIP 81377	1, 2	006.2812	+23.5877	O9.5 Vnn	222 ± 22[a]	[1500]	0.02	24.4	−15
HIP 82171	2	329.9790	−08.4736	B0.5 Ia	845 ± 120[a]	1345	0.09	65.7	−53.3
HIP 88652	2	015.1187	+03.3349	B0 Ia	(650)	[1535]	0.5	8.2	30
HIP 92865	1	041.7070	+03.3784	O8 Vnn	(350)	[1755]	0.04	[2]	−41
HIP 97796	1	056.4824	−04.3314	O7.5 Iabf	2200[c]	[1980]	0.50	[110]	9
HIP 101186	1	082.3557	+02.9571	O9.7 Ia	1486 ± 402[a]	[1735]	0.23	22.3	−28
BD+43 3654	1	082.4100	+02.3254	O4 If	1450[d]	[2325]	6.5	[14]	−66.2
HIP 114990	1	112.8862	+03.0998	B0 II	1400[e]	[1400]	0.6	[52]	−125.3

Figure 2: Stellar bow shock parameters for the selected stars studied in Peri et al. [2012]: coordinates, spectral types, distances, terminal wind velocities, mass loss rates, and proper motion.

Appendix B

Table 1. Constants.

Constant	Simbol	Value (cgs units)
Electron mass	m_e	9.11×10^{-28} g
Proton mass	m_p	1.67×10^{-24} g
Light velocity	c	2.99×10^{10} cm s^{-1}
Electron charge	e	4.80×10^{-10} statC
Thompson cross section	σ_T	6.65×10^{-25} cm^2
Elec. classical radius	r_e	2.82×10^{-13} cm
Fine-structure constant	α	1/137
Solar radius	$R_\odot$	6.955×10^{10} cm
Solar luminosity	$L_\odot$	3.839×10^{33} erg s^{-1}
Boltzmann's constant	k	1.381×10^{-16} erg K^{-1}
Permittivity of free space	ε_0	7.968×10^{-2} (no units in cgs)
Planck constant	h	6.63×10^{-27} erg s

Table 2. Units in CGS.

Magnitude	cgs units	cgs conversion
e	statC	$g^{1/2}$ $cm^{3/2}$ s^{-1}
Energy	erg	g cm^2 s^{-2}
Magnetic field	Gauss	$cm^{-1/2}$ $g^{1/2}$ s^{-1}

Bibliography

Acero, F., Aharonian, F., Akhperjanian, A. G., et al. 2010, A&A, 516, A62 xi, 3, 4, 62, 65, 67, 68, 69, 71, 72, 74, 79

Acero, F., Lemoine-Goumard, M., Renaud, M., et al. 2015, A&A, 580, A74 xi, xiii, 50, 53, 64, 68, 69, 72, 79

Adams, D. J. 1980, Bristol, Adam Hilger, Ltd. (Monographs on Astronomical Subjects, No. 6), 1980. 159 p., 14, 29

Aharonian, F. A. 2004, Very High Energy Cosmic Gamma Radiation: A Crucial Window on the Extreme Universe. Edited by AHARONIAN FELIX A. Published by World Scientific Publishing Co. Pte. Ltd., . ISBN #9789812561732, 9789812561732 2

Aharonian, F., Akhperjanian, A. G., Bazer-Bachi, A. R., et al. 2007, ApJ, 661, 236 62

Baade, W., & Zwicky, F. 1934, Proceedings of the National Academy of Science, 20, 259 62

Bamba, A., Yamazaki, R., Yoshida, T., Terasawa, T., & Koyama, K. 2005, ApJ, 621, 793 4

Bamba, A., Fukazawa, Y., Hiraga, J. S., et al. 2008, PASJ, 60, S153 71, 80

Battaner, E. 1999, Introducción a la Astrofísica. Alianza Editorial, ISBN: 9788420657455 59

Bell, A. R. 1978, MNRAS, 182, 147 11, 20, 33

Benaglia, P., Romero, G. E., Martí, J., Peri, C. S., & Araudo, A. T. 2010, A&A, 517, L10 xi, 3, 4, 35, 44, 45, 47

Berezhko, E. G., Ksenofontov, L. T., & Völk, H. J. 2002, A&A, 395, 943 3, 4

Berezhko, E. G., Ksenofontov, L. T., Voumllk, H. J. 2012, ApJ, 759, 12 60, 69, 72, 74

Berezinskii, V. S., Bulanov, S. V., Dogiel, V. A., & Ptuskin, V. S. 1990, Amsterdam: North-Holland, 1990, edited by Ginzburg, V.L. 18, 77

Blaauw, A. 1961, Bull. Astron. Inst. Netherlands, 15, 265 31

Blumenthal, G. R., & Gould, R. J. 1970, Reviews of Modern Physics, 42, 237 15

Bosch-Ramon, V., & Khangulyan, D. 2009, International Journal of Modern Physics D, 18, 347 16

Brandt, T. J., Acero, F., de Palma, F., et al. 2015, arXiv:1507.03633 61

Burke, B. F., & Graham-Smith, F. 2014, Infrared Astronomy, 25

Comerón, F., & Pasquali, A. 2007, A&A, 467, L23 44

del Valle, M. V., & Romero, G. E. 2012, A & A, 543, A56 3, 4, 18, 20, 25, 35, 36, 43, 77

Draine, B. T., & Lee, H. M. 1984, ApJ, 285, 89 16

Drury, L. O. 1983, Reports on Progress in Physics, 46, 973 11, 12, 33

Fermi, E. 1949, Physical Review, 75, 1169 9

Fernandez, D., Hahn, J., Marandon, V., Renaud, M., & Aion Viana for the H. E. S. S. collaboration 2013, arXiv:1307.6347 4, 68

Fullerton, A. W., Massa, D. L., & Prinja, R. K. 2006, ApJ, 637, 1025

Gardner, F. F., & Milne, D. K. 1965, AJ, 70, 754 63

Gies, D. R. 1987, ApJS, 64, 545 31

Gies, D. R., & Bolton, C. T. 1986, ApJS, 61, 41 31

Ginzburg, V. L., & Syrovatskii, S. I. 1964, The Origin of Cosmic Rays, New York: Macmillan, 1964, 21, 77

Ginzburg, V. L., & Syrovatskii, S. I. 1965, Anual Review of Astronomy and Astrophisics, 3, 297 13

Ginzburg, V. L., & Syrovatskii, S. I. 1969, Anual Review of Astronomy and Astrophisics, 7, 375 13

Gvaramadze, V. V., Kniazev, A. Y., Kroupa, P., & Oh, S. 2011, A&A, 535, A29 35

Gualandris, A., Portegies Zwart, S., & Eggleton, P. P. 2004, MNRAS, 350, 615 32

Gvaramadze, V. V., & Bomans, D. J. 2008, A&A, 485, L29 44

Hasinger, G., Altieri, B., Arnaud, M., et al. 2001, A&A, 365, L4 xiii, 45, 48, 50, 53

Helder, E. A., Vink, J., Bykov, A. M., et al. 2012, Space Science Reviews, 173, 369 61

Hillas, A. M. 1984, Anual Review of Astronomy and Astrophisics, 22, 425 11

Hoogerwerf, R., de Bruijne, J. H. J., & de Zeeuw, P. T. 2000, ApJ, 544, L133 31, 32

Howarth, I. D., Siebert, K. W., Hussain, G. A. J., & Prinja, R. K. 1997, MNRAS, 284, 265 44

Hubrig, S., Oskinova, L. M., & Schöller, M. 2011, Astronomische Nachrichten, 332, 147 40

Kellermann, K. I., & Verschuur, G. L. 1988, Galactic and Extragalactic Radio Astronomy, 2

Kelner, S. R., Aharonian, F. A., & Bugayov, V. V. 2006, Phys. Rev. D, 74, 034018 18, 23, 28, 77

Kippenhahn, R., & Weigert, A. 1990, Stellar Structure and Evolution, XVI, 468 pp. 192 figs.. Springer-Verlag Berlin Heidelberg New York. Also Astronomy and Astrophysics Library, 29

Kobulnicky, H. A., Gilbert, I. J., & Kiminki, D. C. 2010, ApJ, 710, 549 35, 44

Kowal, C. T. 1968, ApJ, 73, 1021 60

Koyama, K., Petre, R., Gotthelf, E. V., et al. 1995, Nature, 378, 255 63

Landau, L. D., & Lifshitz, E. M. 1959, Course of theoretical physics, Oxford: Pergamon Press, 1959, 18, 67

Li, H., & Chen, Y. 2012, MNRAS, 421, 935 62

Li, J.-T., Decourchelle, A., Miceli, M., Vink, J., & Bocchino, F. 2015, MNRAS, 453, 3953

Lin, T., Finkbeiner, D. P., & Dobler, G. 2010, Phys. Rev. D, 82, 023518 63

Longair, M. S. 2011, High Energy Astrophysics, by Malcolm S. Longair, Cambridge, UK: Cambridge University Press, 2011 22

López-Santiago, J., Miceli, M., del Valle, M. V., et al. 2012, ApJ, 757, L6 9, 18, 23, 29, 33

Mackey, J., Mohamed, S., Neilson, H. R., Langer, N., & Meyer, D. M.-A. 2012, ApJ, 751, L10 7, 35, 40, 43, 79

Maíz-Apellániz, J., Walborn, N. R., Galué, H. Á., & Wei, L. H. 2004, ApJS, 151, 103 xi, xiii, 7, 47, 48, 49, 79

Markova, N., Puls, J., Repolust, T., & Markov, H. 2004, A&A, 413, 693 31

Miceli, M., Decourchelle, A., Ballet, J., et al. 2008, Advances in Space Research, 41, 390 44

Miceli, M., Bocchino, F., Decourchelle, A., et al. 2012, A&A, 546, A66 40

Miceli, M., Bocchino, F., Decourchelle, A., et al. 2013, A&A, 556, A80 xi, 63, 64, 67

Miceli, M., Acero, F., Dubner, G., et al. 2014, ApJL, 782, L33 3, 11, 23

Miceli, M., Orlando, S., Pereira, V., et al. 2016, A&A, 593, A26 62, 65, 68, 79

Moffat, A. F. J., Marchenko, S. V., Seggewiss, W., et al. 1998, A&A, 331, 949 xi, 8, 63, 65, 66, 67, 69, 70, 80

Moffat, A. F. J., Marchenko, S. V., Seggewiss, W., et al. 1999, A&A, 345, 321 31

Mohamed, S., Mackey, J., & Langer, N. 2012, A&A, 541, A1 31

Noriega-Crespo, A., van Buren, D., & Dgani, R. 1997, AJ, 113, 780 48

Orlando, S., Bocchino, F., Reale, F., Peres, G., & Petruk, O. 2007, A%A, 470, 927 35

Orlando, S., Bocchino, F., Miceli, M., Petruk, O., & Pumo, M. L. 2012, ApJ, 749, 156

Pereira, V., López-Santiago, J., Miceli, M., Bonito, R., & de Castro, E. 2016, A&A, 588, A36 7, 63, 79

Parizot, E., Marcowith, A., Ballet, J., & Gallant, Y. A. 2006, A&A, 453, 387 7, 37, 78

Peri, C.S., 2010, MSc thesis, Universidad Nacional de la Plata, Argentina 74

Peri C.S., Benaglia, P., Brookes, D. P., Stevens, I. R., & Isequilla, N. L. 2012, A&A, 538, A108 16, 24

Petruk, O., Bocchino, F., Miceli, M., et al. 2009, MNRAS, 399, 157 x, xii, 4, 7, 30, 35, 36, 39, 44, 45, 49, 51, 79, 83, 84

Phillips, M. M. 1993, ApJ, 413, L105 72

Planck Collaboration, Ade, P. A. R., Aghanim, N., et al. 2011, A&A, 536, A23 60

Planck Collaboration, Abergel, A., Ade, P. A. R., et al. 2014, A&A, 571, A11

Posson-Brown, J., Kashyap, V. L., Pease, D. O., & Drake, J. J. 2006, arXiv:astro-ph/0606387

Poveda, A., Ruiz, J., & Allen, C. 1967, Boletin de los Observatorios Tonantzintla y Tacubaya, 4, 86 48

Povich, M. S., Benjamin, R. A., Whitney, B. A., et al. 2008, ApJ, 689, 242 31

Protheroe, R. J., & Stanev, T. 1999, Astroparticle Physics, 10, 185 35

Reynolds, S. P. 1996, ApJL, 459, L13 22

Reynolds, S. P., & Keohane, J. W. 1999, ApJ, 525, 368 71, 80

Repolust, T., Puls, J., & Herrero, A. 2004, A&A, 415, 349 70

Rybicki, G. B., & Lightman, A. P. 1979, New York, Wiley-Interscience, 1979. 393 p. 44

Rieger, F. M., Bosch-Ramon, V., & Duffy, P. 2007, Ap&SS, 309, 119 14, 23, 25

Schaefer, B. E. 1996, ApJ, 459, 438 22

Schulz, A., Ackermann, M., Buehler, R., Mayer, M., & Klepser, S. 2014, A&A, 565, A95 62

Terada, Y., Tashiro, M. S., Bamba, A., et al. 2012, PASJ, 64, 138 x, xi, 43, 44, 47, 49, 79

Tetzlaff, N., Neuhaeuser, R., & Hohle, M. M. 2010, VizieR Online Data Catalog, 741, 190 3, 30, 47

Toalá, J. A., Oskinova, L. M., González-Galán, A., et al. 2016, Apj, 821, 79 31

Turatto, M. 2003, Supernovae and Gamma-Ray Bursters, 598, 21 47

van Buren, D., & McCray, R. 1988, ApJ, 329, L93 60

van Buren, D. 1993, Massive Stars: Their Lives in the Interstellar Medium, 35, 315 35, 40

van Buren, D., Noriega-Crespo, A., & Dgani, R. 1995, AJ, 110, 2914 33

Vink, J. S., de Koter, A., & Lamers, H. J. G. L. M. 2001, A&A, 369, 574 35

Willingale, R., West, R. G., Pye, J. P., & Stewart, G. C. 1996, MNRAS, 278, 749 44

Wilkin, F. P. 1996, ApJL, 459, L31 63

Winkler, P. F., Gupta, G., & Long, K. S. 2003, ApJ, 585, 324 33

Winkler, P. F., Williams, B. J., Reynolds, S. P., et al. 2014, ApJ, 781, 65 63

Zirakashvili, V. N., & Aharonian, F. 2007, A&A, 465, 695 62

Zwicky, F. 1957, Berlin: Springer, 1957 70, 77
31